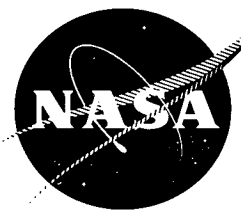


NASA SP-8039

**NASA
SPACE VEHICLE
DESIGN CRITERIA
(CHEMICAL PROPULSION)**

**SOLID ROCKET MOTOR
PERFORMANCE ANALYSIS
AND PREDICTION**



**CASE FILE
COPY**

MAY 1971

NATIONAL AERONAUTICS AND SPACE ADMINISTRATION

FOREWORD

NASA experience has indicated a need for uniform criteria for the design of space vehicles. Accordingly, criteria are being developed in the following areas of technology:

Environment
Structures
Guidance and Control
Chemical Propulsion

Individual components of this work will be issued as separate monographs as soon as they are completed. This document, part of the series on Chemical Propulsion, is one such monograph. A list of all monographs issued prior to this one can be found on the last page of this document.

These monographs are to be regarded as guides to design and not as NASA requirements, except as may be specified in formal project specifications. It is expected, however, that these documents, revised as experience may indicate to be desirable, eventually will provide uniform design practices for NASA space vehicles.

This monograph, "Solid Rocket Motor Performance Analysis and Prediction," was prepared under the direction of Howard W. Douglass, Chief, Design Criteria Office, Lewis Research Center; project management was by John H. Collins, Jr. The monograph was written by William H. Miller of the Rocketdyne Solid Rocket Division, North American Rockwell Corporation, and was edited by Russell B. Keller, Jr. of Lewis. To assure technical accuracy of this document, scientists and engineers throughout the technical community participated in interviews, consultations, and critical review of the text. In particular, Dr. J. D. Hoffman of Purdue University, E. C. Graesser, Jr. of Hercules, Incorporated, and C. A. Speak of Thiokol Chemical Corporation individually and collectively reviewed the monograph.

Comments concerning the technical content of this monograph will be welcomed by the National Aeronautics and Space Administration, Lewis Research Center (Design Criteria Office), Cleveland, Ohio 44135.

May 1971

GUIDE TO THE USE OF THIS MONOGRAPH

The purpose of this monograph is to organize and present, for effective use in design, the significant experience and knowledge accumulated in development and operational programs to date. It reviews and assesses current design practices, and from them establishes firm guidance for achieving greater consistency in design, increased reliability in the end product, and greater efficiency in the design effort. The monograph is organized into two major sections that are preceded by a brief introduction and complemented by a set of references.

The State of the Art, section 2, reviews and discusses the total design problem, and identifies which design elements are involved in successful design. It describes succinctly the current technology pertaining to these elements. When detailed information is required, the best available references are cited. This section serves as a survey of the subject that provides background material and prepares a proper technological base for the *Design Criteria* and Recommended Practices.

The *Design Criteria*, shown in italic in section 3, state clearly and briefly what rule, guide, limitation, or standard must be imposed on each essential design element to assure successful design. The *Design Criteria* can serve effectively as a checklist of rules for the project manager to use in guiding a design or in assessing its adequacy.

The Recommended Practices, also in section 3, state how to satisfy each of the criteria. Whenever possible, the best procedure is described; when this cannot be done concisely, appropriate references are provided. The Recommended Practices, in conjunction with the *Design Criteria*, provide positive guidance to the practicing designer on how to achieve successful design.

Both sections have been organized into decimally numbered subsections so that the subjects within similarly numbered subsections correspond from section to section. The format for the Contents displays this continuity of subject in such a way that a particular aspect of design can be followed through both sections as a discrete subject.

The design criteria monograph is not intended to be a design handbook, a set of specifications, or a design manual. It is a summary and a systematic ordering of the large and loosely organized body of existing successful design techniques and practices. Its value and its merit should be judged on how effectively it makes that material available to and useful to the designer.

CONTENTS

	Page
1. INTRODUCTION	1
2. STATE OF THE ART	3
3. DESIGN CRITERIA and Recommended Practices	55
REFERENCES	83
GLOSSARY	95
NASA Space Vehicle Design Criteria Monographs Issued to Date	103

<u>SUBJECT</u>	<u>STATE OF THE ART</u>		<u>DESIGN CRITERIA</u>	
PREDICTION OF PRESSURE AND THRUST VERSUS TIME	<i>2.1</i>	4	<i>3.1</i>	55
Internal Flow-Field Modeling	<i>2.1.1</i>	5	<i>3.1.1</i>	55
Quasi-Steady-State Performance	<i>2.1.1.1</i>	5	<i>3.1.1.1</i>	56
Uniform Pressure Within Combustion Chamber		—	<i>3.1.1.1.1</i>	56
Nonuniform Pressure Within Combustion Chamber		—	<i>3.1.1.1.2</i>	56
Transient Performance	<i>2.1.1.2</i>	7	<i>3.1.1.2</i>	57
Ignition Transient	<i>2.1.1.2.1</i>	8	<i>3.1.1.2.1</i>	57
Tailoff Transient	<i>2.1.1.2.2</i>	8	<i>3.1.1.2.2</i>	58
Oscillatory Combustion	<i>2.1.1.2.3</i>	9		—
Burning-Front Progression	<i>2.1.2</i>	10	<i>3.1.2</i>	59
Local Flow-Field Effects		—	<i>3.1.2.1</i>	59
Linear and Semilinear Burning		—	<i>3.1.2.1.1</i>	59
Erosive Burning		—	<i>3.1.2.1.2</i>	59
Temperature Effects		—	<i>3.1.2.2</i>	61
Motor Dynamic Effects		—	<i>3.1.2.3</i>	61
Nozzle Performance	<i>2.1.3</i>	14	<i>3.1.3</i>	62
Area Variations	<i>2.1.3.1</i>	14	<i>3.1.3.1</i>	62
Thrust Coefficient	<i>2.1.3.2</i>	15	<i>3.1.3.2</i>	63

<u>SUBJECT</u>	<u>STATE OF THE ART</u>		<u>DESIGN CRITERIA</u>	
Detailed Analytical Prediction	<i>2.1.3.2.1</i>	15	<i>3.1.3.2.1</i>	64
Flow-Field Analyses	<i>2.1.3.2.1.1</i>	19	<i>3.1.3.2.1.1</i>	64
Particle Characterization	<i>2.1.3.2.1.2</i>	22	<i>3.1.3.2.1.2</i>	65
Recombination Losses	<i>2.1.3.2.1.3</i>	27	<i>3.1.3.2.1.3</i>	66
Boundary-Layer Losses	<i>2.1.3.2.1.4</i>	27	<i>3.1.3.2.1.4</i>	67
Heat Losses	<i>2.1.3.2.1.5</i>	28	<i>3.1.3.2.1.5</i>	68
Simplified Analytical Prediction	<i>2.1.3.2.2</i>	29	<i>3.1.3.2.2</i>	69
Flow Separation Effects	<i>2.1.3.2.3</i>	32	<i>3.1.3.2.3</i>	70
PREDICTION OF MOTOR MASS AND MOTOR BALANCE VERSUS TIME	<i>2.2</i>	34	<i>3.2</i>	71
Motor Mass Versus Time	—	—	<i>3.2.1</i>	71
Motor Mass and Motor Balance Versus Time	—	—	<i>3.2.2</i>	71
EVALUATION OF PROPELLANT PERFORMANCE PARAMETERS	<i>2.3</i>	35	<i>3.3</i>	71
Specific Impulse	<i>2.3.1</i>	35	<i>3.3.1</i>	71
Analytical Prediction	<i>2.3.1.1</i>	36	<i>3.3.1.1</i>	72
Demonstration	<i>2.3.1.2</i>	42	<i>3.3.1.2</i>	73
Specific Impulse BEM Characteris- tics	<i>2.3.1.2.1</i>	42	<i>3.3.1.2.1</i>	73
Specific Impulse Scaling	<i>2.3.1.2.2</i>	42	<i>3.3.1.2.2</i>	74
Density	<i>2.3.2</i>	43	<i>3.3.2</i>	76
Burning Rate	<i>2.3.3</i>	44	<i>3.3.3</i>	76
Linear Burning-Rate Characteristics	<i>2.3.3.1</i>	44	<i>3.3.3.1</i>	77
Burning-Rate BEM Characteristics	<i>2.3.3.1.1</i>	44	<i>3.3.3.1.1</i>	77
Chamber Pressure Sensitivity	—	—	<i>3.3.3.1.1.1</i>	78
Temperature Sensitivity	—	—	<i>3.3.3.1.1.2</i>	78
Strand Burning Rates	<i>2.3.3.1.2</i>	47	—	—
Augmentation of Linear Burning Rates	<i>2.3.3.2</i>	48	<i>3.3.3.2</i>	79
Effect of Gas Flow	<i>2.3.3.2.1</i>	48	—	—
Effect of Pressure Transients	<i>2.3.3.2.2</i>	49	—	—
Effect of Spin	<i>2.3.3.2.3</i>	50	—	—
Effect of Strain	<i>2.3.3.2.4</i>	52	—	—
Effect of Bondlines	<i>2.3.3.2.5</i>	52	—	—
PREDICTION OF PERFORMANCE VARIABILITY	<i>2.4</i>	53	<i>3.4</i>	80
Variables	<i>2.4.1</i>	53	<i>3.4.1</i>	80
Prediction of Variations	<i>2.4.2</i>	54	<i>3.4.2</i>	82

LIST OF FIGURES

Figure	Title	Page
1	Typical effect of combustion gas velocity on burning-rate augmentation	12
2	Typical effect of mass flux on burning-rate augmentation	12
3	Characteristic net and control surface	16
4	Typical effect of nozzle contraction ratio on specific impulse	17
5	Typical effect of nozzle convergence on test motor I_{spd} efficiency	17
6	Typical effect of nozzle submergence on specific impulse	18
7	Typical effect of nozzle length on vacuum specific impulse efficiency (optimized conical nozzle configuration)	20
8	Typical effect of condensed metal oxide in exhaust on test motor I_{spd} efficiency	21
9	Measured mass-median Al_2O_3 particle diameter vs. chamber pressure ..	23
10	Effect of residence time on exhaust particle size	24
11	Correlation of particle size/motor size data with maximum stable droplet diameter theory	24
12	Data on the drag coefficient of spheres	25
13	Divergence efficiency for conical nozzles	29
14	Typical influence of expansion and pressure ratios on thrust coefficient	32
15	Physical model of flow separation and static-pressure characteristics ..	33
16	Typical effect of mass flowrate on test motor I_{spd} efficiency	36
17	Typical effects of nozzle parameters on test motor I_{spd} efficiency	38
18	Typical effect of chamber pressure on vacuum specific impulse efficiency	40
19	Typical effect of motor size on vacuum specific impulse efficiency	41
20	Burning rate/pressure relationship for propellants for which $r = aP^n$..	46
21	Burning rate/pressure relationship for three types of propellants	46
22	Effect of acceleration direction on burning rate	50
23	Effect of acceleration on burning rate for different propellants	50
24	Effect of aluminum particle size on burning rate	51
25	Specific impulse scaling schematic	74

LIST OF TABLES

Table	Title	Page
I	Drag Coefficients for Spherical Particles	26
II	Nusselt Numbers for Spherical Particles	26
III	Ballistic Performance Variation Summary	53

SOLID ROCKET MOTOR PERFORMANCE ANALYSIS AND PREDICTION

1. INTRODUCTION

The initial phase of a solid rocket motor development program is typified by numerous parametric studies conducted to optimize the design. Fabrication problems, specified motor performance requirements, and environmental loadings are considered in the evaluation of candidate grain geometries, motor configurations, and propellant formulations. Although these initial design studies are comprehensive, it is not practical to treat parametrically all the factors that influence motor performance. Rather, from these evaluations the optimum design is selected for detailed evaluation. This detailed analysis examines critically the combination of propellant, grain design, and motor configuration to determine whether the proposed motor will perform as specified. The basic problem is to predict full-scale motor performance by using a combination of (1) theoretical performance based on chemical-thermodynamic relationships, and (2) demonstrated performance data obtained from subscale motor tests or from previous firings on full-scale motors of similar design. Performance predictions must identify and quantitatively evaluate the nonideal conditions within a solid rocket motor that result in lower-than-theoretical performance. Insufficient consideration for the differences between theoretical or subscale motor performance and the performance deliverable in a full-scale propulsion system has resulted in initial designs that did not meet the specified performance. Costly redesign and schedule slippage were necessitated or the available performance was accepted with a compromise in mission objectives or in motor reliability.

This monograph is intended to provide the insight and capability to predict accurately the propulsion performance of contemporary solid rocket motor designs. The concept basic to the monograph is that successful analysis and prediction require (1) a thorough understanding of the characteristics of solid rocket motors, of the interrelationships of the critical performance parameters, and of the mechanisms that affect those parameters and thereby degrade ideal performance; and (2) complete familiarity with the analytical techniques and experimental methods appropriate for predicting the propulsive performance of propellant, nozzle, and motor.

Fundamental phenomena and theories are reviewed briefly, and the interrelationships of the critical performance parameters are established. Methods for predicting the

time histories of motor pressure, thrust, and mass flow are presented, together with techniques for evaluating the parameters that are necessary inputs to these predictions; these methods include of course those necessary for identifying and evaluating performance loss mechanisms associated with various propellant systems and with various motor operating conditions. Losses upstream and downstream of the nozzle throat are analyzed for their effect on nozzle performance and deliverable specific impulse. Characteristics of propellant performance parameters, as determined from tests of small ballistic evaluation motors, are assessed to establish desirable test motor characteristics, the number of tests, test condition, and allowable deviations. Techniques for scaling these parameters to predict full-scale motor performance are presented. Where possible, the predicted and demonstrated propellant and motor performances are correlated. In all cases, references are given for detailed coverage of the necessary techniques and procedures.

2. STATE OF THE ART

In a solid rocket motor, hot gases generated by the chemical reaction between a fuel and an oxidizer stored within the motor are accelerated to supersonic velocities through a nozzle designed to develop the resultant force. Propulsion thus is achieved by the conversion of the thermal energy of a chemical reaction into the kinetic energy of combustion products. The effectiveness of this process is predicted and assessed by evaluating the reaction thrust developed through the pressure-imparted momentum of the expanded exhaust gases.

The vector sum of all forces acting on the material within a control volume may be expressed with the momentum equation as

$$\sum \vec{F} = \frac{d}{dt} \int_{cv} \rho \vec{u} dV + \int_{cs} \vec{u} (\rho \vec{u} \cdot \vec{n}) dA \quad (1)^1$$

For the simplified case of a stationary motor with one-dimensional steady flow, this becomes

$$F = \dot{m}_e u_e / g_c + (P_e - P_a) A_e \quad (2)$$

where

- F = thrust, lb_f
- t = time, sec
- ρ = density, lb/in.³
- \vec{u} = local velocity vector, ft/sec
- dV = elemental control volume, in.³
- \vec{n} = unit vector normal to elemental control surface area dA
- dA = elemental control surface area, in.²
- cs = surface of control volume
- cv = control volume
- \dot{m}_e = mass flowrate at nozzle exit, lb_m/sec
- u_e = exhaust-product velocity at nozzle exit, ft/sec
- P_e = exhaust-product static pressure at nozzle exit, lb_f/in.²
- P_a = ambient pressure, lb_f/in.²
- A_e = flow area at nozzle exit, in.²
- g_c = gravitational conversion constant, 32.17 lb_m-ft/lb_f-sec²

Thus, the thrust developed is dependent on exhaust-product mass flowrate, nozzle-exit exhaust velocity and pressure, ambient pressure, and nozzle-exit area. In turn, the initial three parameters are dependent on propellant and motor characteristics that may include propellant burning rate, density, burning-surface area and progression, combustion-chamber pressure and gas temperature, and various geometric

¹Symbols and subscripts are defined in the Glossary.

characteristics of the nozzle. Other variables (e.g., specific impulse and thrust coefficient) often used to evaluate or compare the performance of rocket motors are highly dependent on these initial three parameters.

The analysis and prediction of the deliverable performance of a solid rocket motor require that the interrelations and dependencies of the performance parameters be clearly established and expressed in mathematical form. Mathematical modeling used to simulate solid rocket combustion-chamber internal flow fields is reasonably good for steady-state and transient flow predictions. Proven detailed analytical techniques are available for predicting and scaling deliverable specific impulse and nozzle performance. These analyses account for the major factors contributing to the momentum losses encountered in solid rocket motors. However, there remain numerous uncertainties associated with the prediction of the response of burning-front progression rate to such phenomena as mass flux, spin, unsymmetrical thermal gradients, and high pressure transients. Ballistic evaluation motor tests duplicating these environments greatly enhance the prediction of full-scale motor internal flow and deliverable performance. Considerable data on the demonstrated efficiency of motor and nozzle designs have been accumulated. By use of known efficiency factors, it is possible to adjust theoretical specific impulse and thrust coefficient so that the performance of new but similar motor designs may be predicted accurately.

2.1 Prediction of Pressure and Thrust Versus Time

Prediction of rocket motor performance requires equations that relate deliverable thrust and pressure not only to the physical dimensions of the motor and to the ballistic properties of the propellant but also to specific time periods during motor burn. Instantaneous values of pressure and thrust are related to the discharging mass flowrate, deliverable specific impulse, nozzle thrust coefficient, and nozzle throat area as follows:

$$F = P_c A_t C_F = (\dot{m}_t I_{spd})_{\text{motor}} = (\dot{m}_t I_{spd})_{\text{propellant}} + (\dot{m}_t I_{spd})_{\text{inerts}} + (\dot{m}_t I_{spd})_{\text{igniter}} \quad (3)$$

where

P_c = stagnation pressure of exhaust gases just upstream of nozzle entrance section, lb_f/in.²

A_t = nozzle throat area, in.²

C_F = nozzle thrust coefficient

\dot{m}_t = mass flowrate at nozzle throat, lb_m/sec

I_{spd} = deliverable specific impulse, lb_f-sec/lb_m

The contributions of the igniter (sec. 2.1.1.2.1) and inerts (secs. 2.2 and 2.3.1.2.2) normally are secondary factors in predicting overall motor performance. Propellant mass flowrate is predicted from the expression

$$\dot{m}_p = A_b r_b \rho_p \quad (4)$$

where

- \dot{m}_p = propellant mass flowrate, lb_m/sec
- A_b = propellant burning-surface area, in.²
- r_b = burning-front progression rate, in./sec
- ρ_p = propellant mass density, lb_m/in.³

Propellant burning-surface area A_b may be predicted by laying out the grain configuration and mapping burning fronts by drafting techniques, or by using automated geometry computer programs such as those described in references 1 through 4. Burning-front progression rate r_b is dependent on propellant type, on the conditioning received by the grain before motor operation, and on the conditions that exist within the combustion chamber during motor operation. Thus, to predict rocket motor thrust- and pressure-time histories accurately, analytical techniques must model mathematically (1) the flow of the combustion gases within the combustion chamber, (2) the characteristics of the burning-surface progression, and (3) the nozzle performance parameters.

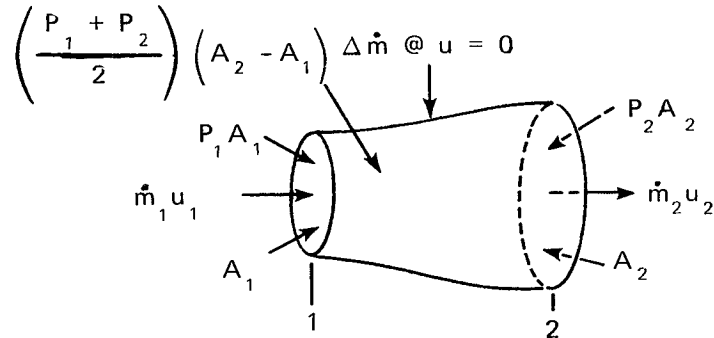
2.1.1 Internal Flow-Field Modeling

Thrust- and pressure-time histories of most rocket motors are evaluated in steps that treat separately each of three phases of motor operation: (1) quasi-steady state, (2) ignition transient, and (3) tailoff transient. Contemporary mathematical models are used to analyze gas flow and mass addition to the flow within the combustion chamber and to predict chamber pressure and discharge flowrates. These models are based on fundamental gas dynamic and thermodynamic relationships with proper consideration for conservation of mass, energy, and momentum.

2.1.1.1 Quasi-Steady-State Performance

Steady-state gas dynamic relationships are used to describe motor performance during the operational phase in which the time rate of change of chamber pressure does not significantly affect propellant or motor ballistic characteristics. Interior ballistics for this "quasi-steady-state" condition are predicted by one of two methods, both of which assume a one-dimensional flow. The first method, hereafter referred to as "equilibrium," is applicable for the condition in which the pressure is essentially constant throughout the motor chamber, i.e., mass flux (mass flow per unit of cross-sectional flow area) in the grain port is low enough that the pressure drop over the burning surface is slight. The second method (incremental analysis) is required in the analysis of high-performance, high-volumetric-loaded motors in which mass flux is significant and results in a significant pressure drop.

The requirement for higher performance motors has forced the designer to develop this second method of calculation. As pointed out in reference 5, the effects of mass flux and mass addition on the combustion process are being successfully predicted with analytical methods and burning-rate rules developed from test data. The gas flow is evaluated assuming a one-dimensional, incremental flow as depicted in the following sketch of a motor element:



where subscript 1 identifies the forward end of the element and subscript 2 identifies the aft end. Equation (5) is developed by applying the momentum equation to this element and assuming steady flow:

$$P_1 A_1 - P_2 A_2 + \left(\frac{P_1 + P_2}{2} \right) (A_2 - A_1) = \frac{(\dot{m}_2 u_2 - \dot{m}_1 u_1)}{g_c}$$

$$P_2 = P_1 - \frac{2(\dot{m}_2 u_2 - \dot{m}_1 u_1)}{(A_1 + A_2)g_c} \quad (5)$$

This expression relates the pressure at the forward end of the element P_1 with that at the aft end of the element P_2 in terms of mass flowrate, gas velocity, and flow area. A series of these increments is assumed down the length of the grain, and summing the pressure drops occurring across each increment provides the pressure difference within the combustion chamber resulting from mass addition. Complete motor analysis involves an incremental analysis of both gas generation and the resulting flow conditions. Three factors are involved in this incremental analysis: changing flow area, changing burning surface, and changing rate of burning. Variations in all three may occur between increments from the forward end to the aft end of the propellant cavity. Thus, it is not practical to write a single equation for the relation between head-end static pressure and nozzle-end stagnation pressure. However the method of evaluating the flow by small increments, equation (5), and summing these incremental variations has been very successful (refs. 1 through 5).

2.1.1.2 Transient Performance

Transient equations are used when the mass, momentum, volume, and pressure of the combustion products within the motor chamber vary significantly with time. Mass conservation requires that motor performance be expressed (ref. 6, pp. 237-238) as

$$\rho_p A_b r_b = \dot{m}_t + \frac{d}{dt} (\rho_c V_c) \quad (6)$$

where

ρ_c = density of combustion gas, lb_m/in.³
 V_c = chamber free volume, in.³

Several simplifying assumptions are made in the solution of this equation. For the time interval under analysis, chamber free-volume changes generally are neglected and combustion temperature T_c is assumed constant, as is the characteristic velocity of the combustion gas c^* . With these assumptions incorporated, equation (6) can be expressed as (ref. 6, pp. 238-239)

$$\frac{dP_c}{dt} = \frac{R_0 T_c}{\bar{M} V_c} \dot{M} \quad (7)$$

where

$$\dot{M} = \rho_p A_b r_b - A_t P_c C_D \quad (7a)$$

and

$C_D = g_c/c^* = \text{mass flow factor, sec}^{-1}$

R_0 = universal gas constant, 1545.5 ft-lb_f/lb_m-mole-°R

\bar{M} = average molecular weight of gas, lb_m/lb_m-mole

$$c^* = \sqrt{\frac{R_0 T_c g_c}{\bar{M} \gamma} \left(\frac{\gamma + 1}{2} \right)^{(\gamma+1)/(\gamma-1)}} \quad (\text{ideal rocket}), \text{ ft/sec}$$

γ = specific heat ratio

Equations (7) and (7a) show the use of the mass flow factor C_D and its relationship to the characteristic velocity c^* . Both C_D and c^* are widely used. For consistency in this monograph, however, only c^* will be used hereafter.

As in the steady-flow analyses of quasi-steady-state motor operation, the gas dynamics of the combustion-chamber internal flow field usually are predicted by summing incremental elements of flow evaluated over very short time intervals. Solutions are obtained by iterating the continuity and momentum equation for discharge pressure, temperature, and flowrate. Equations using these fundamental engineering principles are presented in references 2 and 7.

The transient phases most often of concern are motor ignition and tailoff or boost-sustain type transitions. However, both oscillatory combustion and vehicle acceleration can introduce transient phenomena. The possible occurrence of either condition must be considered by the designer.

2.1.1.2.1 Ignition Transient

During the ignition transient, mass flow from the igniter and the rate of flame propagation over the propellant grain burning surface must be considered in addition to the aforementioned nonsteady flow. The igniter contribution is discussed in detail in the design criteria monograph "Solid Rocket Motor Igniters" (ref. 8). References 1 through 4 also treat the igniter contribution; reference 9 provides a comprehensive analysis of current ignition theories. In the ballistic computer program described in reference 3, the ignition transient model is based on the mass balance equation,

$$\dot{M} = \dot{m}_{ig} + \rho_p r_b A_b - \frac{A_t P_c g_c}{c^*} \quad (8)$$

One of the most significant problems involved is predicting and treating the rate of flame spreading. In this program, \dot{m}_{ig} is an input as a function of time. The surface A_b is calculated from an input flame spread rate and the initial surface that is calculated by the grain-geometry subroutine. Reference 4 employs an incremental element analysis, in conjunction with a tabulation of the burning-rate coefficient as a function of distance burned, to simulate the effects of the flame front propagation rate. A similar approach is taken in reference 1, wherein flame spread is simulated by providing an input of a zero burning rate at all longitudinal stations of the grain at which the flame front has not yet arrived.

2.1.1.2.2 Tailoff Transient

Tailoff pressure bleddown accompanies the significant reduction in propellant burning surface that occurs with propellant burnout or boost-sustain type transitions. With propellant remaining in the chamber (as in boost-sustain transitions), the flow field and chamber pressure are described by equations (6) and (7). After propellant burnout, equation (7) becomes

$$\frac{dP_c}{dt} = - \frac{R_0 T_c A_t P_c g_c}{\bar{M} V_c c^*} \quad (9)$$

which can be solved to express chamber pressure as a function of bleddown time for choked flow:

$$P_c = P_{bo} \exp \left(- \frac{R_0 T_c A_t g_c t}{\bar{M} V_c c^*} \right) \quad (10)$$

where

P_{bo} = chamber stagnation pressure at propellant burnout, $\text{lb}_f/\text{in.}^2$
 t = time from propellant burnout, sec

The foremost problem in predicting these transient histories is to obtain an accurate prediction of the presence, shape, and magnitude of silver (propellant remaining in the motor at web burnout and the onset of tailoff). This prediction, in turn, is dependent on the success achieved in modeling the gas dynamics and in simulating propellant ballistic characteristics in the quasi-steady-state performance predictions. Other factors that have influenced the accuracy of these transient predictions include nozzle slagging and the failure to use propellant ballistic and performance parameters evaluated at the environmental conditions existing within the combustion chamber during the particular time interval under analysis. These problems generally are approached by using the incremental steady-flow analysis technique and treating propellant propulsive properties as a function of chamber pressure.

2.1.1.2.3 Oscillatory Combustion

A phenomenon encountered from time to time in solid rocket motor development is oscillatory combustion, i.e., pressure (flow) oscillations in the transverse modes (circumferential or radial) or in the axial (longitudinal) mode. In recent years, the addition of metallic fuels to solid propellant compositions has essentially eliminated the occurrence in the transverse modes. Even with metallized propellants, however, axial-mode oscillations continue to occur. Sometimes these appear spontaneously, and in other cases a pressure pulse may be necessary to initiate them. These axial-mode oscillations frequently are evident merely as small-amplitude, sinusoidal pressure oscillations at the first longitudinal mode of the chamber. Although these mild oscillations may have no adverse effect on motor operation, their acceptability depends on the characteristics of the system of which the motor is a part. Occasionally, the oscillations manifest themselves in a more severe wave form of greater amplitude, frequently consisting of higher harmonics of the first mode. In these instances, unacceptable increases in mean pressure and thrust levels may result, and pressure excursions may be severe enough to endanger structural integrity.

Much progress has been made in understanding the very complex interactions of the combustion and flow fields involved in oscillatory combustion. Many comprehensive reviews have been presented in the last few years (refs. 10 through 12) covering various aspects of the subject. This work to date, however, has not resulted in a unified confirmed method or procedure to follow in the motor design phase to eliminate the possibility of oscillatory combustion, although efforts are being exerted in this direction (refs. 13 and 14). Following the design guidelines in references 13 and 14 does not eliminate the possibility that oscillatory combustion will occur, but reduces the likelihood of this occurrence. Knowledge to date is better suited to guiding effective corrective action once oscillatory combustion is encountered. Such actions include modifying the propellant or revising the motor design to

incorporate acoustic cavities, baffles, and the like. The right approach depends on the individual circumstances, but even the best solution may result in some performance penalty.

2.1.2 Burning-Front Progression

Propellant burning-front progression rate is expressed as an empirical function dependent on propellant composition, propellant conditioning, combustion-chamber environment, and motor dynamics. Grain temperature, local static pressure, and mass flow significantly influence the local burning rate. For propellant grain configurations that have a low gas velocity or mass flux in the propellant cavity, burning-front progression rate is predicted with a simple pressure-dependent equation such as

$$r = a P_c^n \quad (11)$$

where

r = linear burning rate of propellant, in./sec

a = coefficient of pressure

n = linear burning-rate pressure exponent

For certain propellant formulations, the pressure exponent may be a function of pressure. If the exponent is constant with pressure, the expression is known as de Saint Robert's law. In either event, the propellant burning-rate coefficient and exponent for the temperatures to which the motor will be subjected are determined experimentally by the methods described in section 2.3.3.1.1. These experimental data are used to determine coefficients that describe the propellant burning rate as a function of both temperature and pressure. The four most commonly used coefficients are

$$\pi_K = \left[\frac{\partial \ln P}{\partial T_o} \right]_{K_n} \quad (12)$$

$$\sigma_P = \left[\frac{\partial \ln r}{\partial T_o} \right]_P \quad (13)$$

$$\sigma_K = \left[\frac{\partial \ln r}{\partial T_o} \right]_{K_n} \quad (14)$$

$$\pi_{P/r} = \left[\frac{\partial \ln P}{\partial T_o} \right]_{P/r} \quad (15)$$

where

T_o = conditioning temperature of the propellant, °F

K_n = ratio of propellant burning-surface area to nozzle throat area

Relationships of this type have been used successfully to predict burning-front progression rates for motor configurations in which mass flux in the grain port is less than the threshold value. For most propellants, however, certain levels of local gas

velocity or mass flux flowing parallel to the burning surface lead to an increased propellant burning rate. This augmentation often is referred to as "erosive burning" and has been found to vary significantly with propellant type and with chamber pressure. For certain propellants, burning rates have been noted to decrease at low flowrates, but at high flowrates this tendency reverses and burning rates increase. Figures 1 and 2 (refs. 15 and 16) illustrate typical characteristics of this augmentation as influenced by gas velocity and mass flux, respectively. The velocity or mass flux at which augmentation begins is referred to as the threshold value and is frequently related to operating pressure by a simple semi-empirical expression such as

$$u_{tv} = k_1 + k_2 P^{k_3} + k_4 P^{k_5} \quad (16)$$

or

$$G_{tv} = k_6 + k_7 P^{k_8} + k_9 P^{k_{10}} \quad (17)$$

where

$k_1, k_2 \dots k_{10}$ = experimentally determined coefficients and exponents

u_{tv} = threshold gas velocity, ft/sec

G_{tv} = threshold mass flux, lb_m/sec-in.²

Experience has shown that, when motor designs result in high mass flux values, burning-front progression cannot be expressed successfully by a linear burning-rate law. Many semi-empirical expressions describing burning-front progression rate under high-velocity conditions have been developed; they are reviewed in references 17 and 18. Specific expressions, as recommended in section 3.1.2.1.2, generally are of the form

$$r_b = a P_c^n (1 + \delta_{\text{augmentation}}) \quad (18)$$

where δ is an expression involving the internal flow-field and grain-geometry parameters considered to be influential in determining local burning rate.

For erosive burning, δ is evaluated with experimental data of the type shown in figures 1 and 2. To treat such augmenting environments as spin and pressurization, additional augmentation δ terms are included within the parentheses of equation (18).

Demonstrated motor performance (refs. 19 through 22) has shown extreme augmentation in burning rate caused by spin-induced acceleration. Detailed studies have been conducted to establish the parameters that contribute to this augmentation; these are reviewed in section 2.3.3.2.3. To date, no universal analytical or empirical

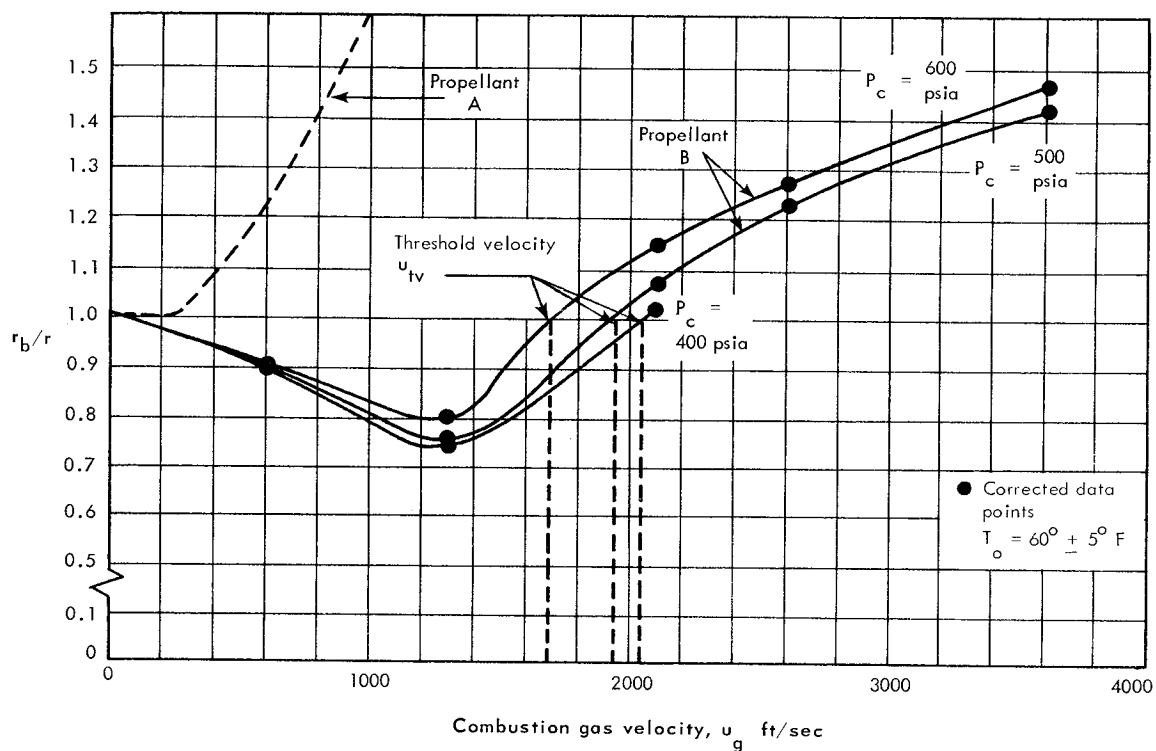


Figure 1.—Typical effect of combustion gas velocity on burning-rate augmentation (ref. 15).

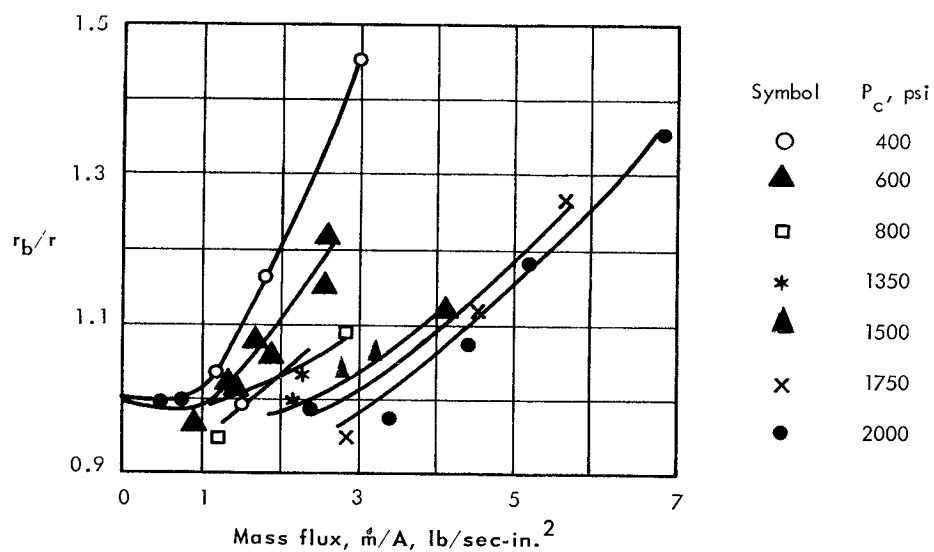


Figure 2.—Typical effect of mass flux on burning-rate augmentation (ref. 16).

solution has been established. The spin effect generally is treated as a direct increase in the linear burning rate, with the magnitude of augmentation $\delta_{\text{acceleration}}$ based on data from small-motor tests.

As further emphasized in the compilation of rocket motor spin data in reference 23, the angular acceleration effects are not restricted to burning-rate augmentation. A qualitative evaluation of the data in reference 23 indicated that centrifugal accelerations as low as 10 g directed perpendicularly into the burning surface of metallized solid propellants usually will (1) increase ignition delay time, (2) increase motor operating pressure, (3) decrease burn time, (4) extend the tailoff burning period, and (5) increase motor burnout mass and thermal protection requirements by depositing metallic oxide on the chamber/nozzle walls.

Increased motor operating pressure and decreased burn time in the spin environment may be attributed to higher mass addition rates that result directly from an acceleration induced increase in either the apparent propellant burning rate or the burning-surface area. In addition, motors incorporating end-burning grains and the usual converging-diverging nozzle are subjected to severe centerline coning of the propellant surface in a spin environment. Although the cause of this phenomenon has not yet been determined, the effect generally has been reduced or effectively eliminated by modifying the nozzle configuration.

Reference 24 presents a recent survey of the analytical studies of the interior ballistics of rocket motors subject to spin. The use of these techniques in predicting internal ballistics is not established practice. However, this survey led to the following tentative conclusions:

First: Rotation reduces the mass flux at the throat. This effect is accentuated by increasing the motor spin rate and by increasing the nozzle contraction ratio. However, a significant portion of this decrease may be negated by a transfer of angular momentum to the nozzle walls through viscous shear. This reduction in mass flux produces the same effect as a decrease in throat area and thus can cause increases in chamber pressure over the nonrotating condition. This pressure increase can be detrimental to successful motor performance because of the sensitivity of the propellant to pressure.

Second: Recirculating viscous flow patterns can build up from the action of the fore and aft end sections of the motor, and the boundary layer can transport significant portions of the mass from one area of the flow field to another. There also is a possibility of backflow patterns from dynamic effects in the nozzle. These patterns, as predicted analytically, can be quite complex if the ratio of tangential-to-axial velocity becomes much greater than unity. The hot combustion gases in these backflow and recirculatory patterns tend to impinge on the propellant and produce local variations in the burning rate. However, the patterns tend to be unstable and break up readily when disturbed.

Finally: Rotating flow in the combustion chamber establishes pressure gradients that may alter the local burning rates. In addition, the acceleration forces accompanying the pressure gradients can cause retention of solid phases at the propellant surfaces or otherwise affect the propellant combustion zone.

2.1.3 Nozzle Performance

The nozzle characteristics that most influence motor propulsion performance are throat area A_t and thrust coefficient C_F . Ideally, thrust coefficient, defined as $C_F = F/P_c A_t$, is a function only of nozzle geometry; gas specific heat ratio; and chamber, ambient, and nozzle-exit pressures (ref. 25, p. 55). In actual systems, however, this nozzle performance coefficient is influenced also by the two-phase lag, chemical nonequilibrium, boundary-layer losses, and transfer of heat to the nozzle. Typical maximum values of performance losses for the first three are 5 percent two-phase lag, 2 percent recombination, and 2 percent viscous losses. Heat loss to the nozzle is very dependent on the heat-sink properties of the nozzle material and the motor firing duration; no typical maximum percentage loss can be indicated. Predicting these loss factors necessitates combining theoretical analyses with empirical relationships and demonstrated performance.

2.1.3.1 Area Variations

Computer programs used in performance predictions are capable of analytically simulating nozzle throat- and exit-area variations that may occur during a motor firing. The simulation techniques differ in mathematical manipulation.

Reference 1 uses a nozzle-throat-diameter vs. time tabular input, references 2 and 3 treat diameters with specified erosion rates, and reference 4 expresses nozzle throat diameters as a series function of time. The data used are generally based on detailed heat-transfer analyses and subscale motor or material evaluation tests. The significance of accounting for nozzle erosion has been illustrated in test results. In one instance (ref. 26), a loss of 6 to 9 seconds in delivered specific impulse was experienced by burnout of a 55-second-duration motor. These losses include those caused by reductions in expansion ratio and by increased surface roughness.

Subscale nozzle and nozzle material evaluation tests generally are conducted during the initial phases of a motor development program to verify the design and material selection or to provide inputs to the nozzle detailed heat-transfer analysis (refs. 28 through 31). Wong (ref. 32) reviews state-of-the-art practices for predicting heat transfer to the nozzle from the two-phase, high-temperature, corrosive exhaust gases. The analyses treat convection from the gases, radiation of metal oxide particles, and energy resulting from particle impingement.

Certain nozzle inserts are fabricated from noneroding materials such as tungsten, tungsten-molybdenum, and silver-infiltrated tungsten. Experience has shown that inserts of this type expand under continuous heating and reduce throat area. This throat contraction is predicted by analyzing heat effects on the structural integrity of the insert backup insulation materials and the theoretical growth of the insert under the influence of the temperature and pressure at the throat.

Recent studies reported in reference 30 and analyses of motor firings have indicated that metal oxide is deposited on the nozzle throat surfaces during portions of a motor firing. When these deposits build up, they can reduce the throat area enough to produce an increase in the chamber pressure. These deposits are discharged either when the nozzle surface temperature attains the melting temperature of the metal oxide or when the gas dynamic drag forces exceed the strength of the deposit. If the breakdown of the deposit depends primarily on surface temperature, the buildup occurs once in the early phases of firing. If the breakdown depends primarily on drag forces, the deposits may form repeatedly. In either case, performance is affected. However, while the deposit studies have been informative and have identified a possibly significant phenomenon, they have not produced analytical techniques currently accepted for use in predicting the occurrence and buildup of these deposits.

2.1.3.2 Thrust Coefficient

Many sophisticated computer programs have been prepared to evaluate nozzle flow fields, to determine deliverable thrust coefficients, and to provide inputs to nozzle heat-transfer and structural analyses. However, use of these analyses often is circumvented by combining idealized rocket performance with efficiency factors based on performance delivered by previous motor designs. In both approaches, the influence of back-pressure-induced flow separation on thrust is semi-empirically assessed.

During early phases of a motor development program, coldflow tests are occasionally used for mass flowrate determinations and for the investigation of design characteristics that influence this rate and localized flow patterns. In addition, these tests may be used to identify flow separation characteristics. However, coldflow tests do not establish total nozzle performance and are expensive; therefore, these tests are not conducted as a standard practice.

2.1.3.2.1 Detailed Analytical Prediction

Thrust coefficient prediction requires analysis of high-temperature subsonic, transonic, and supersonic flow fields in which a two-phase medium, chemically in nonequilibrium, is gaining momentum through expansion. Simultaneously, the flow is losing energy because of friction, transfer of heat, and radial expansion. The differential

equations that express the limiting condition of irrotational flow of a compressible fluid in these different Mach number regimes differ in form. In the subsonic regime, the partial differential equations are elliptical; in the transonic regime ($0.8 < M < 1.2$), mixed; at the sonic condition, parabolic; and, in the supersonic regime, hyperbolic. Different mathematical techniques are required to evaluate these flow regimes.

The term “discharge coefficient” frequently is used to express how well the nozzle entrance design permits the flow effectively to fill the nozzle throat. This coefficient C_W is calculated as the ratio

$$C_W = \frac{\dot{m} \text{ (across transonic control surface)}}{\dot{m} \text{ (for 1-D flow through throat at sonic conditions)}} \quad (19)$$

Deliverable mass flowrate is calculated by numerically integrating the flow across the transonic control surface (fig. 3) that is established in the gas dynamic analysis of the transonic region of the nozzle throat.

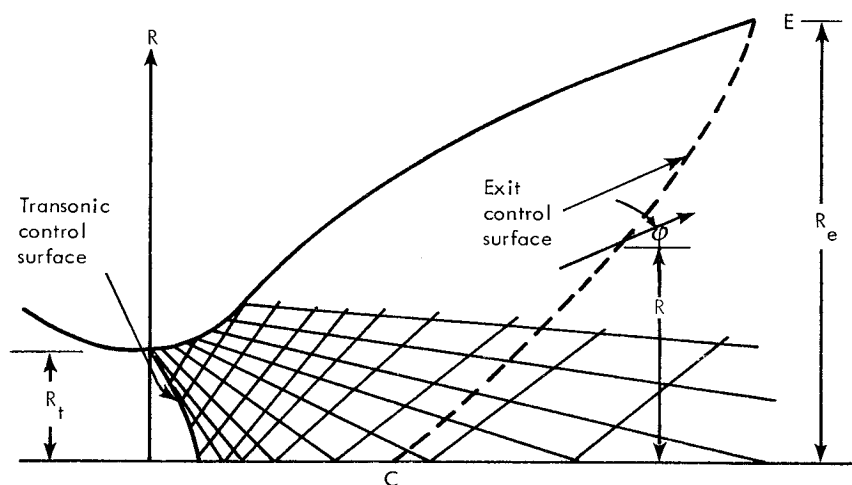


Figure 3.—Characteristic net and control surface.

Momentum losses incurred upstream of the nozzle throat significantly affect C_W . Qualitatively, entry contour and contraction ratio limitations account for 30 to 90 percent of these losses, viscous effects can account for 5 to 10 percent, and submergence 25 percent.

Figures 4 and 5 are examples of the effect on specific impulse and on specific impulse efficiency (I_{spd}/I_{osp}) associated with nozzle-entry contraction and curvature. Data presented in section 2.3.1.1 show the additional influence of throat entrance

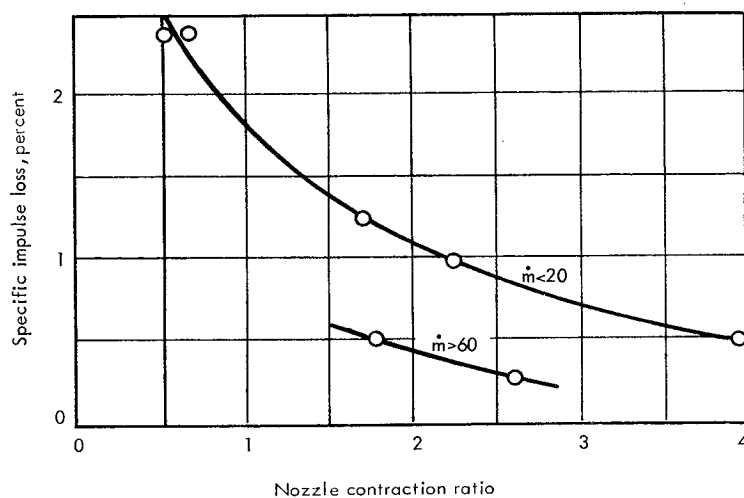


Figure 4.—Typical effect of nozzle contraction ratio on specific impulse (ref. 27).

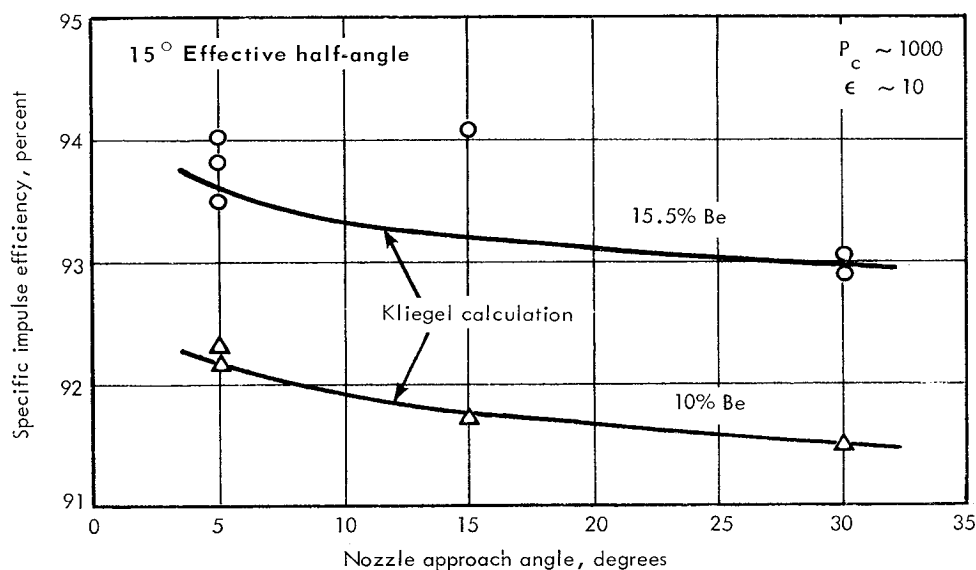


Figure 5.—Typical effect of nozzle convergence on test motor I_{spd} efficiency (ref. 27).

radius of curvature on impulse efficiency. The typical motor performance losses shown below and in section 2.3.1.1 have been attributed to nozzle entrance geometry and its combined influence on the condensed-phase acceleration profile, local heat loss, and nozzle erosion (ref. 27).

Submergence losses reported in reference 33 were relatively more significant than the 25 percent previously stated. However, their study included other entrance loss

factors as well. More recent data (fig. 6, from ref. 34) have isolated the influence of submergence per se, and in so doing indicated that its effect on overall motor performance loss is less severe than originally projected.

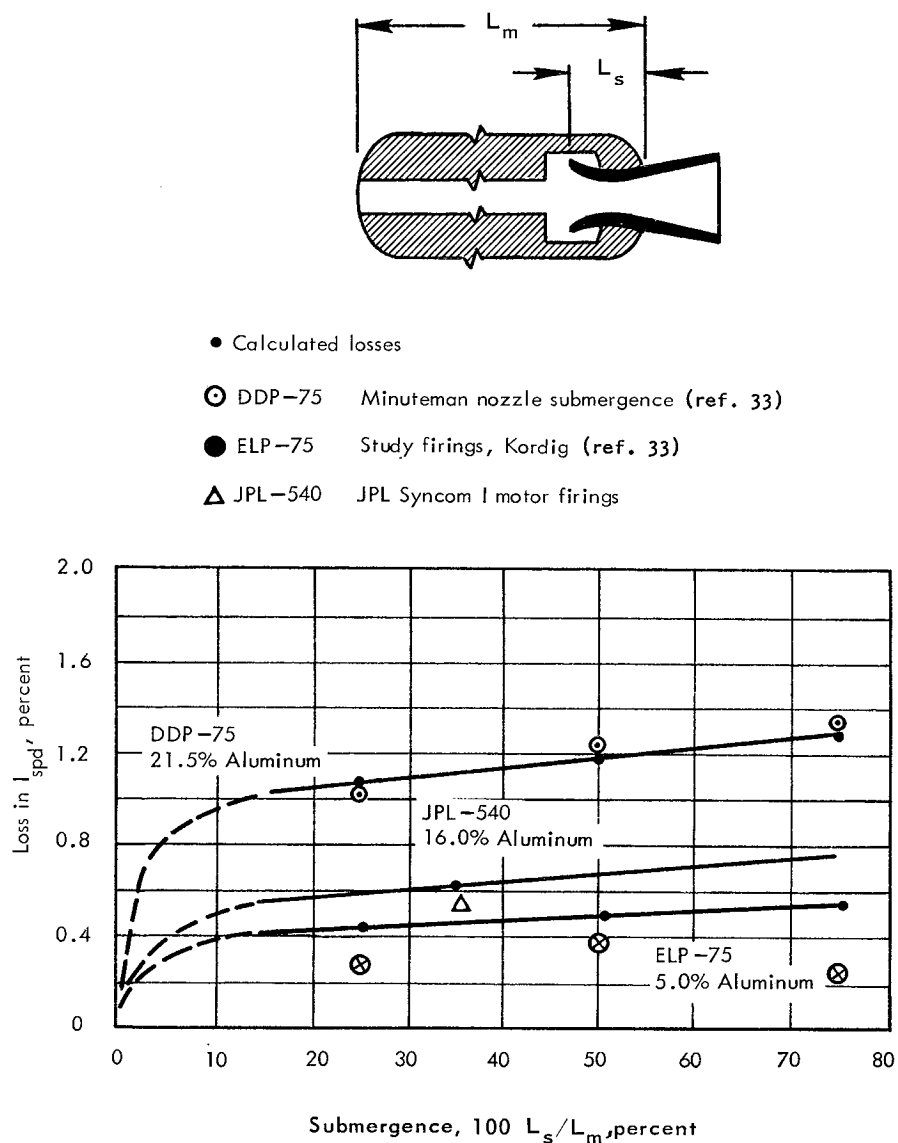


Figure 6.—Typical effect of nozzle submergence on specific impulse (ref. 34).

Flow characteristics evaluated at the transonic control surface are used as inputs to a method-of-characteristics analysis of the supersonic flow field in the nozzle exhaust cone. Thrust augmentation by this divergent section can be calculated by

integrating the pressure forces along the nozzle wall. Total nozzle thrust coefficient is computed by summing the thrust, equation (1), at the transonic control surface and at the nozzle-exit wall:

$$C_F = \frac{F}{P_c A_t} = \frac{F \text{ (input line)} + F \text{ (nozzle wall)}}{P_c A_t} \quad (20)$$

A second common technique for evaluating thrust coefficient (refs. 35 through 37) uses the total mass flowrate and the calculated velocity field across the exit control surface. For vacuum conditions, reference 37 expresses thrust coefficient as

$$C_{F_{vac}} = 2\pi \int_C^E \left\{ P/P_c + \left(\frac{\rho u^2}{P_c g_c} \right) \left(\frac{\sin \alpha \cos \phi}{\sin (\phi + \alpha)} \right) \right\} (R/R_t) d(R/R_t) \quad (21)$$

where

α = Mach angle

ϕ = angle between local velocity vector and motor centerline, deg

C, E = limits on control surface passing through exit of nozzle and intersecting meridional plane (fig. 3)

Powdered metals commonly are used as fuel additives to improve propulsive performance. However, deleterious effects are produced by the resulting liquid or solid particles that occur in the exhaust stream when these additives are present. Gas drag on the particles (thermal nonequilibrium between gas and particle) and possible particle impingement on the nozzle wall are involved. To account for these effects, the analyses made to evaluate the thrust function for this expanding divergent flow must be capable of treating two-phase media. Additional loss mechanisms that must be considered include recombination, boundary-layer, and heat losses. In a recent comparative evaluation Kliegel (ref. 38), using a conventional 5000-pound-thrust motor as a base, quoted the following as probable percentage losses in specific impulse: two-phase lag, 2.5 percent; recombination, 1.0 percent; boundary layer, 1.0 percent; condensation, 0.3 percent; and shock, 0.2 percent. These do not include divergence or heat losses; however, Crowe et al. (ref. 39) combined these losses with lag, recombination, and boundary-layer losses in their correlation study of high-performance nozzles. Typical examples of the predicted and experimental results are presented in figure 7. This study used a small motor with 12.5 pounds of 16 percent Al propellant. Conical nozzle configurations for which data are shown in figure 7 were those that were predicted to deliver optimum performance for the specified nozzle length.

2.1.3.2.1.1 Flow-Field Analyses

The effect of condensed metal oxide in the exhaust products of solid rocket propulsion systems (fig. 8) has been the subject of many reviews (refs. 40 through 42) and studies as borne out in Caswell's annotated bibliography (ref. 43) on two-phase nozzle flow. Two-phase losses are incurred because these condensed particles fail to gain momentum or transfer thermal energy. The particles gain motion only from

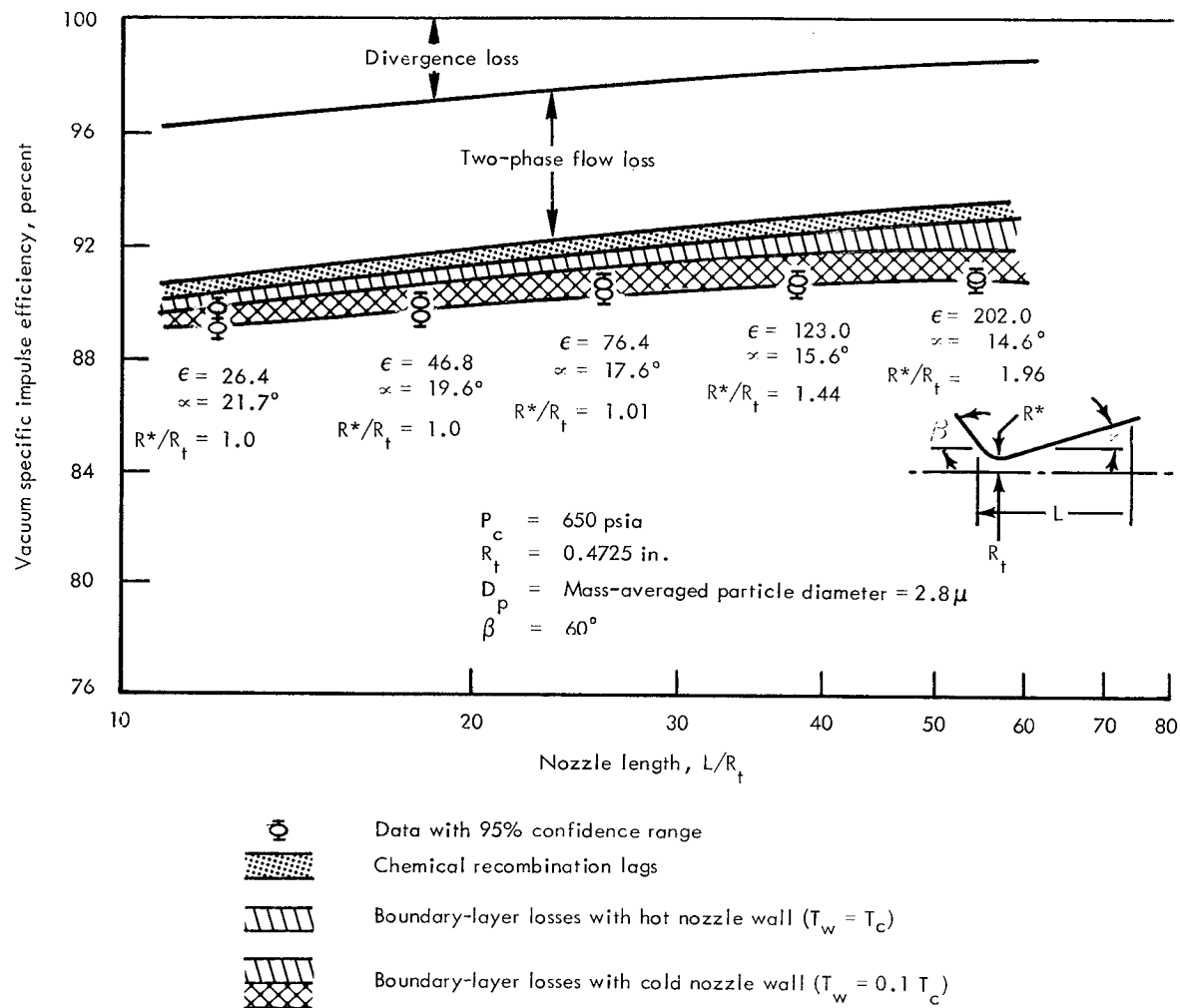


Figure 7.—Typical effect of nozzle length on vacuum specific impulse efficiency (optimized conical nozzle configuration) (ref. 39).

drag forces exerted by the combustion gases, and they transfer heat to these same gases primarily by convection. The inability of the particles and gases to achieve kinetic and thermal equilibrium can reduce I_{osp} (theoretical specific impulse) by as much as 5 percent, although a more common loss is 1.5 to 2.5 percent.

Programs have been prepared to analyze the flow of gas and particles in one-dimensional (refs. 44 through 48), two-dimensional, and axisymmetric nozzles (refs. 49 through 51). As emphasized in reference 52, other programs exist, but many have not been documented in the open literature and, as with those documented, their degrees of sophistication differ considerably. Finite-rate performance losses and nozzle boundary-layer and heat losses generally are not treated in these programs but are assessed separately.

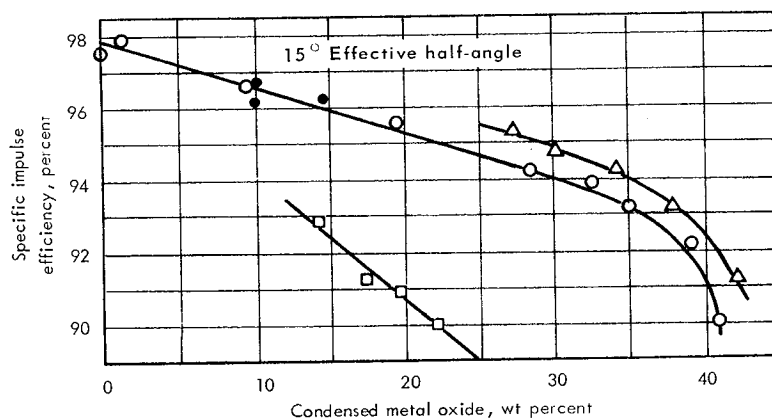


Figure 8.—Typical effect of condensed metal oxide in exhaust on test motor I_{spd} efficiency (ref. 27).

These programs use various analytical techniques in solving the gas-particle flow fields in the three Mach number regimes. The two-dimensional potential flow theory (ref. 53) is applied in the solution of subsonic flow fields. However, the governing equations for gas-particle mixtures are elliptic in nature; thus, approximations assuming one-dimensional-type flow or two-dimensional incompressible flow often are used.

In the transonic region, the analytical techniques used to predict two-phase flow effects are based on gas-dynamic theory with the gas characteristics modified to account for the condensed phase. In a recent review of analytical techniques for evaluating transonic idealized flow, the ICRPG Working Group on Performance Standardization (ref. 52) noted that exact solutions of this flow have not been achieved but that approximations have been derived by use of the small-perturbation theory. Series solutions in terms of the ratio of nozzle upstream radius R^* to the throat radius R_t and the specific heat ratio of the combustion gases γ have resulted from analyses described in references 54 through 56. These solutions appear to approximate closely actual flow for $R^*/R_t > 2.0$, but they are entirely inadequate for $R^*/R_t < 1.0$. Because of length restrictions, practical rocket nozzles generally have R^*/R_t ranging from 0.5 to 2.0; therefore, a method based on the perturbation theory is often inappropriate for solving transonic flow. One method (ref. 57) for evaluating transonic flow involving a small value for R^* is to use an inverse solution of the transonic flow field—streamlines are calculated from a given velocity distribution along the nozzle axis. This velocity distribution is adjusted until the boundary streamline corresponds to the desired real boundary. Both the radius of curvature and the entrance angle are considered. Steady, irrotational, adiabatic, and shockfree flow of a perfect gas with constant specific heats is assumed.

For perfect gas flows, approximate transonic solutions can be obtained (refs. 54 through 57) by taking perturbations about the sonic velocity point near the throat.

This method is applicable for perfect gas flows because the throat conditions are determined essentially by the nozzle geometry in the immediate neighborhood of the throat and are quite insensitive to the nozzle inlet geometry. This is not true for gas-particle flows because the throat conditions are determined by the nozzle inlet geometry. Thus, to obtain the conditions necessary to begin the calculation of supersonic characteristics for a gas-particle system, the equations for the complete subsonic and transonic flow field in the nozzle inlet and throat regions must be solved.

In applying these analytical techniques to the prediction of two-phase exhaust flow fields, the following assumptions are made:

- (1) The particles are spherical in shape and of a specified size with a uniform internal temperature.
- (2) These particles do not interact with each other and are of negligible volume.
- (3) Total gas-particle-mixture mass and energy are constant, and thermal energy is transferred by convection only.
- (4) External forces, except pressure of the gas and drag of the particles, are negligible and initial kinetic lags exist. Gas and particle specific heats generally are treated as being constant and have a value appropriately averaged for a two-phase medium.

By using a sink-flow analysis of a one-dimensional, gas-particle mixture under constant-lag conditions, it was determined (ref. 44) that a two-dimensional, axisymmetric gas-particle mixture flow in the transonic throat region can be treated as a perfect gas with an appropriately modified specific heat ratio and Mach number. This and Sauer's (ref. 55) power-series solutions are used by Hoffman (ref. 49) to determine the flow-field characteristics for this modified perfect gas. Kliegel (ref. 59) also assumes a one-dimensional sink flow and an effective specific heat ratio but uses a fourth-order approximation for the gas velocity component as described therein. These transonic characteristics serve as inputs for the method-of-characteristics solution of the supersonic exhaust flow field.

Studies of gas-particle flow (ref. 58) revealed that all the characteristics of the governing flow equations are real if the flow is supersonic. Thus, the supersonic flow of a gas-particle mixture can be computed by using the method of characteristics. The fundamentals of this mathematical technique are reviewed in reference 59, and early application to nozzle design is described in reference 60. It should be emphasized, however, that the accuracy of predicting nozzle performance with a two-phase medium is dependent not only on accurate solutions to the flow equations but also on the characteristics of the particles.

2.1.3.2.1.2 Particle Characterization

Particle shape, size, size distribution, and drag and heat-transfer coefficients must be either known or assumed so that the two-phase flow equations may be integrated. The logarithmic normal size distributions (ref. 58) remain consistent with the

findings of many recent investigations (ref. 41). Particle size measurements (ref. 61) made by direct sampling of the exhaust products and by an optical in situ technique have indicated that size is a function of several variables including chamber pressure (fig. 9), metal concentration, motor residence time (fig. 10), motor size (fig. 11), and thrust level. Recent reviews (refs. 62 and 63) have concluded that residence time in the motor is the principal independent variable. However, chamber pressure is also a significant parameter.

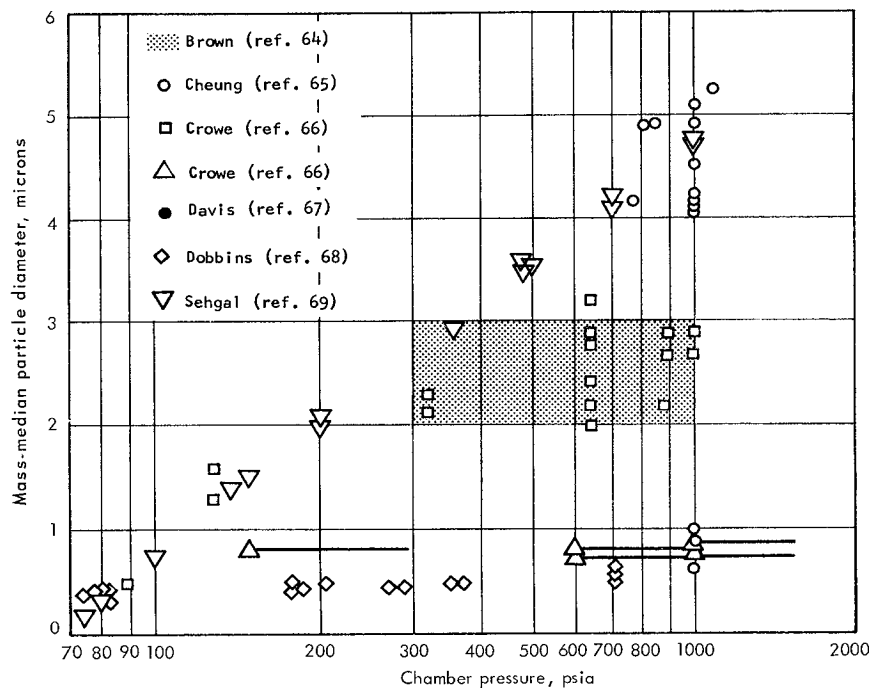


Figure 9.—Measured mass-median Al_2O_3 particle diameter vs. chamber pressure (ref. 62).

Numerous mathematical models have been developed to describe particle growth. Cheung and Cohen's (ref. 70) vapor condensation model explains both the pressure dependence and the metal concentration effect on oxide particle diameter. The amount of condensate per unit time is proportional to the cube of the particle diameter and also to the flux condensing (or agglomerating) across the boundary layer. Cheung and Cohen (ref. 65) also derived (from the rate equation for a first-order chemical reaction) a particle-growth law that related oxide droplet diameter to chamber pressure and residence time. An equilibrium or limiting mean droplet diameter of about 5 microns is reached when the oxide vapor supply is depleted. Brown (ref. 62) reviewed several models that account for the larger particles as the result of oxide coagulation or agglomeration. For the stable-drop diameter model (for which in fig. 11 the theoretical sizes are compared with particle sizes from actual motor firings), it is assumed that coagulation would result from the faster

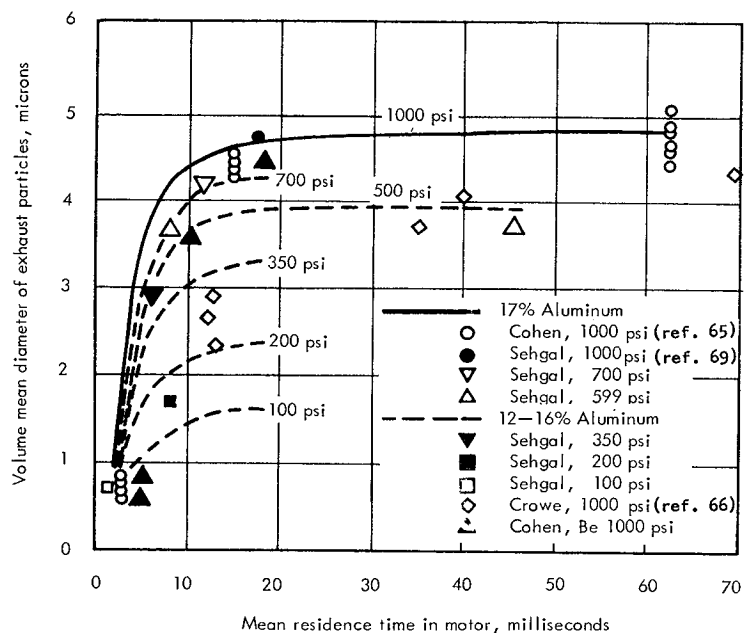


Figure 10.—Effect of residence time on exhaust particle size (ref. 62).

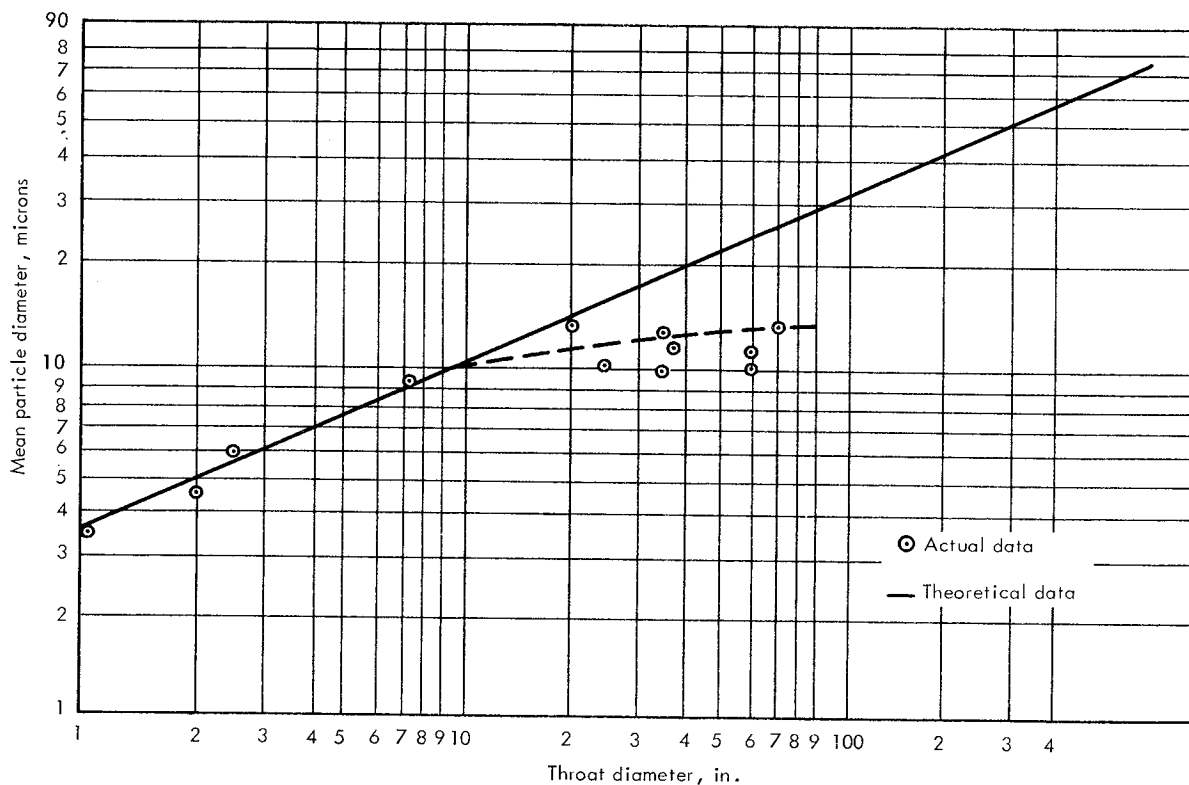


Figure 11.—Correlation of particle size/motor size data with maximum stable droplet diameter theory (ref. 71).

moving, smaller particles overtaking and colliding with larger droplets. Coagulation would follow when the oxide remained liquid. The limiting size of the droplet finally is reached when drag forces overcome surface energy, at which time larger droplets are shattered. Maximum stable-droplet size depends heavily on nozzle size and oxide surface tension and slightly on chamber pressure, nozzle contour, and droplet concentration. This approach correlated well with Smith's and Cohen's data, but not with Sehgal's. Brown further showed that the application of Setze's model to Cohen's data had predicted the existence of 10-micron particles in large motors two years before the experimental data obtained by Smith et al. (fig. 11, from ref. 71).

Various semi-empirical relationships have been suggested for the expression of particle drag and heat-transfer coefficients. All investigations have been conducted under the assumption that the particles are spherical and that Reynolds number is based on the particle-gas lag velocity increment. Summaries of values for drag coefficients are presented in figure 12 and table I, and for Nusselt number in table II. In figure 12, drag coefficients are compared with Stoke's drag law. Recent work by Crowe (ref. 39) and Carlson and Hoglund (ref. 72) indicate particles encounter the gamut of flow regimes from continuum to free-molecule flow. Semi-empirical expressions for particle drag over these regimes are developed in the referenced reports and are listed in table I along with Kliegel's expression (ref. 58) that corrects for slip flow.

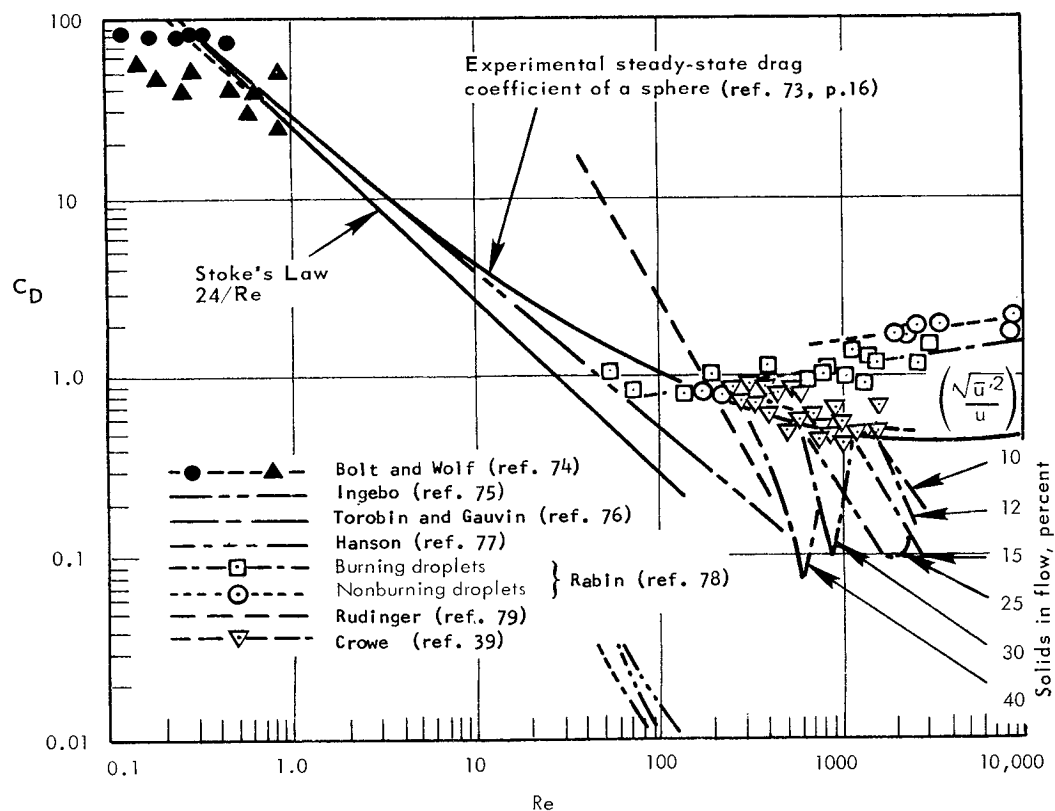


Figure 12.—Data on the drag coefficient of spheres (adapted from ref. 80).

Table I.—Drag Coefficients for Spherical Particles

Theoretical and semi-empirical expressions	Ref.
$C_D = \frac{24}{Re}$, where $(Re < 1)$	73 (p. 97)
$C_D = \frac{24}{Re} \left(1 + \frac{3 Re}{16} \right)$, where $(Re < 5)$	73 (p. 98)
$C_D = C_D^{(0)} \left[\frac{(1 + 7.5 Kn)(1 + 2 Kn) + 1.91 Kn^2}{(1 + 7.5 Kn)(1 + 3 Kn) + (2.29 + 5.16 Kn)Kn^2} \right]$	58
$C_D = \frac{24}{Re} \left[\frac{\left\{ 1 + 0.15 Re^{0.687} \right\} \left\{ 1 + \exp \left[\left(\frac{0.427}{M^{4.63}} \right) - \left(\frac{3.0}{Re^{0.88}} \right) \right] \right\}}{1 + \frac{M}{Re} \left[3.82 + 1.28 \exp \left(- \frac{1.25 Re}{M} \right) \right]} \right]$	72
$C_D = \left(C_{D_{inc}} - 2 \right) \exp \left[- 3.07 \sqrt{\gamma} \frac{M}{Re} g(Re) \right] + \frac{h(M)}{\gamma^{1/2} M} \exp \left[- \frac{Re}{2M} \right] + 2$	81
where $\log_{10} g(Re) = 1.25[1 + \tanh(0.77 \log_{10} Re - 1.92)]$ and $h(M) = [2.3 + 1.7 (T_p/T_g)^{1/2}] - 2.3 \tanh(1.17 \log_{10} M)$	

Table II.—Nusselt Numbers for Spherical Particles

Semi-empirical expressions	Ref.
$Nu = 2.5 Re^{0.15} + 0.04 Re$	
$Nu = 2 + 0.370 Re^{0.6} Pr^{1/3}$	82
$Nu = 2 + 0.459 Re^{0.55} Pr^{1/3}$	42
$Nu = \frac{Nu^{(0)}}{1 + 3.42 \frac{M}{Re Pr} Nu^{(0)}}$	83
$Nu = \frac{2 + 0.459 Re^{0.55} Pr^{0.33}}{1 + 3.42 \left(\frac{M}{Re Pr} \right) (2 + 0.459 Re^{0.55} Pr^{0.33})}$	72
$Nu = \frac{Nu^{(0)}}{1 + 2.72 \frac{Kn}{\gamma^{1/2} Pr} Nu^{(0)}}$	58
$Nu = \left[\left(2 + 0.654 Re^{1/2} Pr^{1/2} \right)^{-1} + 3.42 \frac{M}{Re Pr} \right]^{-1}$	

2.1.3.2.1.3 *Recombination Losses*

In thermochemistry programs used to predict performance of an idealized motor (sec. 2.3.1.1), chemical reactions are assumed to be either "frozen" or in "shifting" equilibrium with the gas flow process. In frozen flow predictions, it is assumed that chemical composition does not change during the expansion but that phase equilibrium is obtained (ref. 84). Shifting equilibrium flow predictions assume that the time for the system to reach chemical equilibrium is much shorter than the time for expansion through the nozzle and chemical equilibrium is obtained (ref. 84). Equilibrium predictions provide maximum theoretical performance. The programs prepared by Zeleznik and Gordon (refs. 85 and 86) are typical of those used in predicting frozen and equilibrium performance.

With real flows, however, losses are incurred because the expanding gases require a finite time for chemical recombination. There are two basic techniques (ref. 52) for calculating these finite-rate performance losses. The first (an exact method) performs step-by-step integration of equations that describe an arbitrary set of relaxation or recombination of processes. The enthalpy and composition of the expanding nonequilibrium gas flow can be found at any point in the nozzle through the solution of these equations. An example of this type of program is the one prepared by Kliegel et al. (ref. 48). The second method (an approximate solution) assumes that the nozzle flow can be divided into three regions: (1) a region of near-equilibrium flow, (2) a transition region, and (3) a region of nearly frozen flow. Most approximate methods reduce the transition region to a point called the "sudden freezing point." Equilibrium flow then is assumed up to the sudden freezing point, and frozen composition flow is assumed after this point. A program using this second method of finite-rate performance prediction, typified by Bray's work (ref. 87), was used in the prediction shown in figure 7. Another loss that can be considered broadly under the heading of recombination losses is that resulting from supercooling of liquids. Under certain conditions, a loss in specific impulse of as much as 1.3 percent has been attributed to supercooling. In this instance the kinetic mechanism is controlled by nucleation, not by chemical reaction.

2.1.3.2.1.4 *Boundary-Layer Losses*

Analyses of two-phase flow fields and the determination of particle trajectories indicate that the boundary layer in nozzles for solid propellant motors is composed primarily of gas with few particles (ref. 88). Exceptions occur only if the particles

are so very small that they have no channeling tendency or if the nozzle is very long and its contour permits particle impact (ref. 58). Therefore, boundary-layer and heat-transfer analyses generally are made by assuming a gaseous medium without particles; the boundary layer is assumed to be turbulent. The solution to this problem normally is computed by employing a simultaneous solution of the integral momentum and energy equations as described in reference 89.

The influence of boundary-layer losses often has been neglected when the viscous drag appears to be insignificant because of the small surface areas on which viscous forces would act (ref. 90). To establish the true significance of the boundary-layer and heat losses, however, each loss must be evaluated with respect to the accuracy of the performance prediction required for the particular motor being analyzed. To illustrate the magnitude of these losses relative to other performance losses, some typical values calculated for a well-insulated contoured nozzle with a 39:1 expansion ratio are, in percent,

Particle-lag loss	1.5
Boundary-layer loss	1.5
Heat losses	0.1
Nozzle-divergence loss	2.6
Combustion-efficiency loss	1.8

These values indicate that boundary-layer losses can be as significant as particle-lag losses. Similar calculations for nozzles of various geometries having 10:1 expansion ratios predicted boundary-layer losses ranging from 0.45 to 1.0 percent of the corresponding value. These calculations predicted motor performance values to within 1.5 to 2.5 percent of those delivered.

2.1.3.2.1.5 Heat Losses

In a study of high-performance nozzles (ref. 39), heat losses were found to be more significant than those given in section 2.1.3.2.1.4. For the nozzles shown in figure 7, heat losses were 1 to 1.5 percent whereas boundary-layer losses were less than 1 percent. Heat losses usually are predicted by integrating the distribution of heat flux over the affected hardware surface areas for the motor operational time. Heat flux distributions are predicted using heat-transfer coefficients as determined from the boundary-layer analysis and from the gas dynamics analysis of the local exhaust flow field. These thermal losses are converted to equivalent kinetic energy or specific impulse losses.

2.1.3.2.2 Simplified Analytical Prediction

From equation (2) and the definition of thrust coefficient, the following expression is obtained for one-dimensional, isentropic flow in an idealized converging-diverging nozzle (ref. 91):

$$C_{F_{ideal}} = \sqrt{\frac{2\gamma^2}{\gamma-1} \left[\frac{2}{\gamma+1} \right]^{(\gamma+1)/(\gamma-1)} \left[1 - \left(\frac{P_e}{P_c} \right)^{(\gamma-1)/\gamma} \right]} + \frac{P_e - P_a}{P_c} \left(\frac{A_e}{A_t} \right) \quad (22)$$

The maximum coefficient value corresponding to any fixed pressure ratio is achieved when $P_e = P_a$; the largest possible value occurs under vacuum conditions where $P_a = 0$. The effect of nonaxial exhaust velocities is treated through a divergence loss factor λ . For the conical nozzle, with point-source flow assumed,

$$\lambda = \frac{1 + \cos \alpha}{2} \quad (23)$$

where α is the nozzle-divergence half-angle.

As shown in figure 13 (from ref. 92), at high expansion ratios and moderate divergent angles, this relationship correlates well with losses predicted with detailed method-of-characteristics analyses. This detailed, two-dimensional analysis includes both the effects of nonaxially directed momentum at the nozzle exit and the effect of throat curvature on the discharge coefficient.

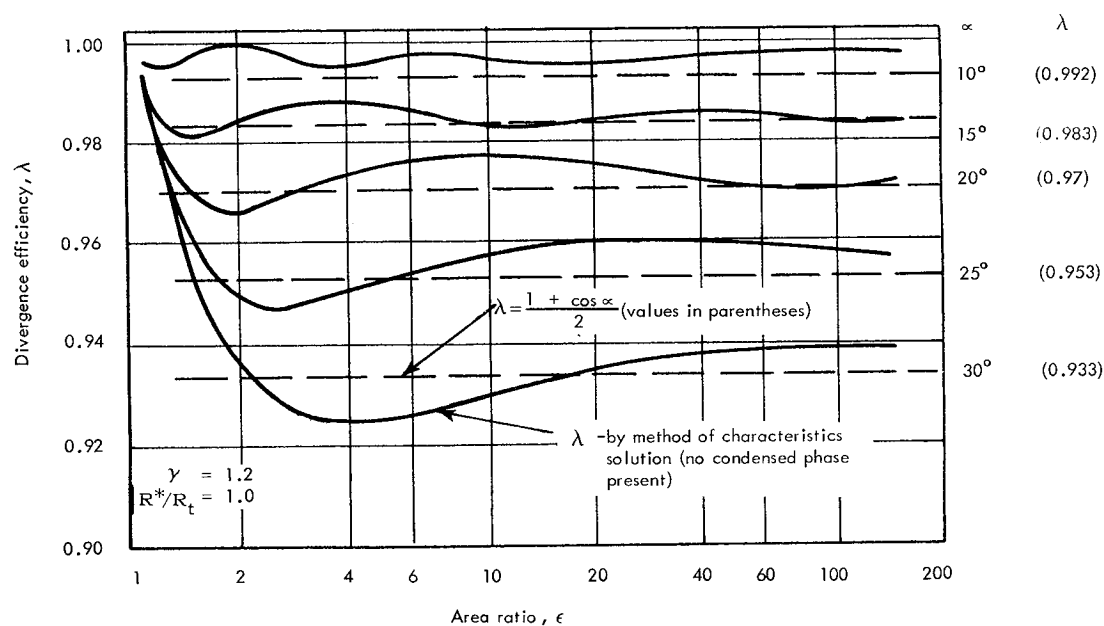
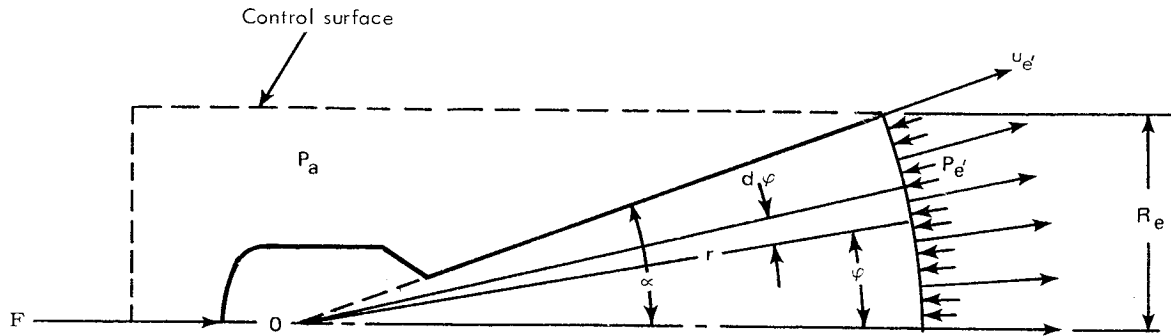


Figure 13.—Divergence efficiency for conical nozzles (adapted from ref. 92).

Presently, some confusion remains as to which terms in equation (22) are corrected for divergence losses. Therefore, a brief development of the point-source flow assumed in equation (22), originally derived by Malina (ref. 93) and later clarified by Landsbaum (ref. 94) and Rao (ref. 95), is presented below. Terms are identified in the accompanying sketch of a one-dimensional conical nozzle.



It is assumed that the streamlines in the expanding part of this conical nozzle are all straight lines that intersect at the point 0; this assumption provides the basis for the term "point-source flow." The control surface indicated passes through the spherical segment of radius r over which exhaust properties are constant. Vacuum thrust can be determined by integrating across this spherical area:

$$F_{\text{vac}} = \int \left[\left(\frac{\dot{m}_{e'} u_{e'}}{A_{e'} g_c} \right)_x + (P_{e'})_x \right] dA_{e'} \quad (24)$$

where the subscript e' refers to conditions evaluated at this spherical segment. In converting to the x -direction, the following substitutions are made:

$$(u_{e'})_x = u_{e'} \cos \phi \quad (24a)$$

$$(P_{e'})_x = P_{e'} \cos \phi \quad (24b)$$

$$\rho_{e'} u_{e'} = \dot{m}_{e'} / A_{e'} \quad (24c)$$

$$dA_{e'} = 2\pi r^2 \sin \phi d\phi \quad (24d)$$

Then equation (24) becomes

$$F_{\text{vac}} = \int_0^\alpha [\rho_{e'} u_{e'}^2 / g_c + P_{e'}] 2\pi r^2 \sin \phi \cos \phi \, d\phi \quad (25)$$

Upon integration, equation (25) becomes

$$F_{\text{vac}} = \left[\frac{\dot{m}_{e'}}{A_{e'}} u_{e'} / g_c + P_{e'} \right] \pi r^2 \sin^2 \alpha \quad (26)$$

The plane area A_e can be expressed as

$$A_e = \pi r^2 \sin^2 \alpha$$

and, with this substitution, equation (26) becomes

$$F_{\text{vac}} = \frac{\dot{m}_{e'} u_{e'} A_e}{A_{e'} g_c} + P_{e'} A_e \quad (27)$$

Further, the ratio of areas can be expressed in terms of λ as

$$\frac{A_e}{A_{e'}} = \frac{1 + \cos \alpha}{2} = \lambda$$

With this substitution, equation (27) becomes either

$$F_{\text{vac}} = \frac{\lambda \dot{m}_{e'} u_{e'}}{g_c} + P_{e'} A_e \quad (28)$$

or

$$F_{\text{vac}} = \lambda \left(\frac{\dot{m}_{e'} u_{e'}}{g_c} + P_{e'} A_{e'} \right) \quad (29)$$

In contemporary nozzles, the difference between $P_e A_e$ and $P_{e'} A_{e'}$ is a small contributor to the thrust (refs. 94 and 96). Consequently, the divergence loss factor λ frequently is applied only to the momentum component $\dot{m} u_e$ as in equation (28). For equation (28) to express thrust properly, the static exit pressure $P_{e'}$ must be based on the spherical segment expansion ratio $\varepsilon_{e'}$, where

$$\varepsilon_{e'} = \frac{A_{e'}}{A_t} \quad (30)$$

and A_t is the critical throat area corresponding to the deliverable mass flow \dot{m}_t (ref. 95).

Thrust efficiency factor η_F is an empirical parameter based on correlations with previously demonstrated performance. The range of this factor usually is from 0.92 to 0.98 with the typical value for a well-designed nozzle being 0.96 or greater. For new motor designs with propellant and nozzle systems similar to systems for which performance has been demonstrated, accurate thrust-time predictions can be made by using idealized thrust coefficients corrected for divergence losses by a demonstrated η_F value that includes the divergence loss factor λ . If a contoured nozzle is involved, an effective λ based on demonstrated performance correlations is used to modify η_F . One such relationship for effective half-angle loss for contoured nozzles (ref. 27) is

$$\lambda = 1/2 \left[1 + \cos \left(\frac{\alpha + \theta_{ex}}{2} \right) \right] \quad (31)$$

where

α = half-angle of inscribed cone
 θ_{ex} = lip angle of nozzle at exit plane

2.1.3.2.3 Flow Separation Effects

The performance of a rocket motor may be significantly reduced if the motor operates at an ambient pressure considerably higher than that for which the nozzle was designed (fig. 14). This over-expanded condition often is encountered in sea-level

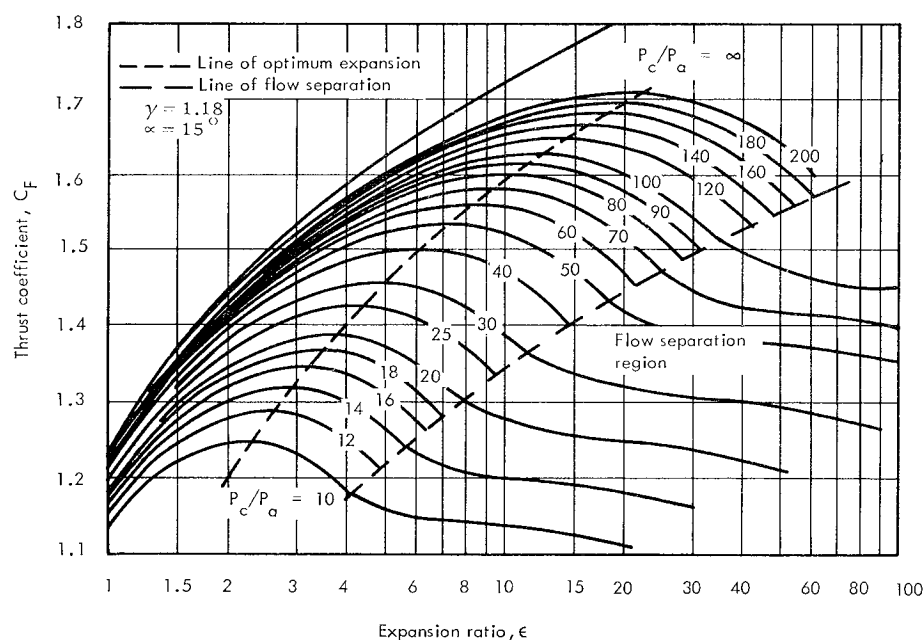


Figure 14.—Typical influence of expansion and pressure ratios on thrust coefficient (ref. 96).

static testing of motors that will operate at high altitudes or in launch vehicles that operate over a wide range of altitudes with the nozzle expansion ratio optimized for a mean altitude. The nozzle flow under such operational conditions frequently separates. When the ambient pressure is less than or only slightly greater than the nozzle exhaust pressure, the flow within the nozzle remains undisturbed (refs. 91 and 97). However, an ambient pressure considerably greater than the exhaust pressure can induce boundary-layer separation, oblique shocks, and flow separation as illustrated in figure 15. The thrust capability of a propulsion system is degraded when it operates in an overexpanded condition. Once the flow separates, some of the degradation is recovered because the static pressure on the nozzle will increase (fig. 15).

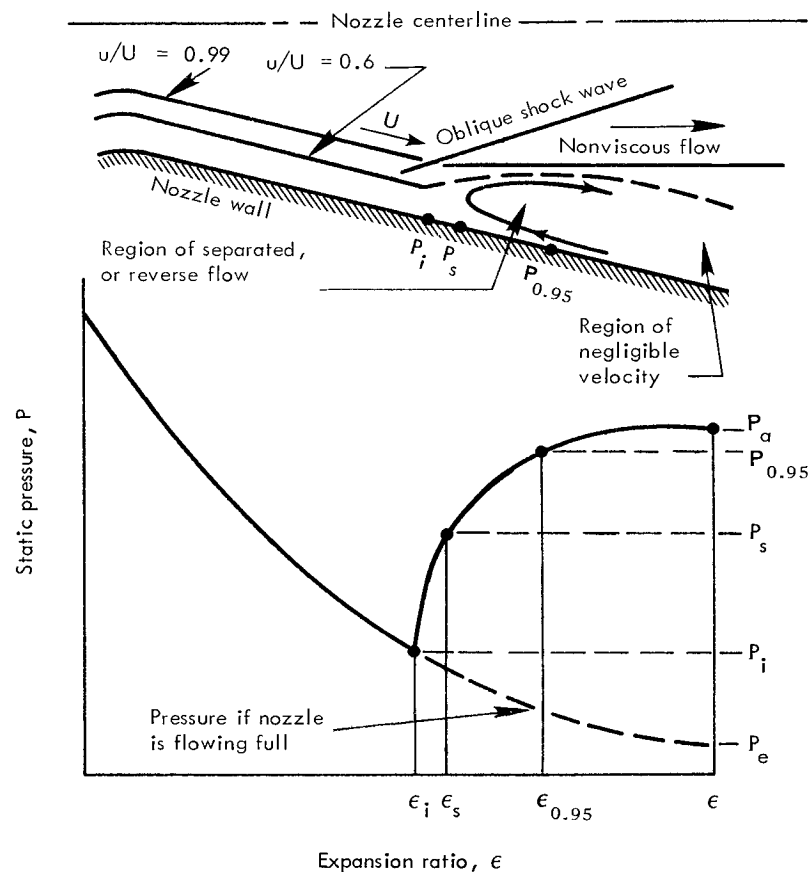


Figure 15.—Physical model of flow separation and static-pressure characteristics (ref. 96).

Many empirically based constants have been used for the pressure and Mach-number ratios at which flow separation is predicted to occur (refs. 25, 36, 91, and 98 through 102). However, a general relationship has been determined by Kalt and Badal

(ref. 96) from their extensive review of flow separation in conical nozzles. They relate separation, ambient, and chamber pressures in the expression

$$\frac{P_i}{P_a} = \frac{2}{3} \left(\frac{P_a}{P_c} \right)^{1/5} \quad (32)$$

where P_i is the pressure at initiation of separation (in psia).

Thus, when $P_i/P_a < P_c/P_a$ (where P_c for this check is based on one-dimensional isentropic flow) separation will begin at the nozzle area ratio for which the predicted static pressure is equal to P_i . Reference 1 utilizes an empirical series expression of third order in predicting the occurrence of separation. The prediction of the thrust developed over that region of the nozzle in which the flow is separated is made by integration of the pressure distribution over this nozzle region. The pressure distribution generally is approximated by an empirical relationship developed to simulate the typical distribution depicted in figure 15.

2.2 Prediction of Motor Mass and Motor Balance Versus Time

To satisfy flight-vehicle requirements for acceleration, dynamic stability, and control, motor mass and balance characteristics often must comply with specified envelopes. For unguided systems, general requirements specify only mass and center-of-gravity limits. In such a system operating in an atmospheric environment in which aerodynamic forces are present, the vehicle must be stable about the center of gravity. If the center of gravity does not stay within specified limits, it may shift aft of the aerodynamic center of pressure and make the vehicle unstable. Mass-time history is critical to vehicle performance because it is proportional to the vehicle velocity history. Failure to comply to the specified mass-time envelope could result in variations in the desired vehicle trajectory and range. For systems that are fully controlled during motor burning, operational envelopes are typically specified both for mass and center of gravity and for the principal moments of inertia. Principal moments of inertia significantly influence the dynamic response of the vehicle during maneuvers. Unless these and the center of gravity remain within specified design limits, controllability of the vehicle is reduced, and the vehicle may fail to achieve and maintain the desired flight path and flight orientation.

Certain programs currently used in predicting motor performance automatically calculate time histories of propellant mass, center of gravity, and principal moments of inertia (ref. 3). (References 2 and 4 treat only symmetrical grain configurations.) The longitudinal division of the propellant grain into small incremental volumes and the calculation of the propellant consumed in each volume during the analyzed time interval permit accurate predictions (sec. 2.1.1.1). Other programs provide only a history of propellant mass and thus require separate calculations for the prediction of balance characteristics. The discharge of inert components is not treated in these programs and also must be calculated separately.

Commonly used performance prediction programs treat the propellant only and do not account for the discharge of inert material. The source and quantity of inert discharge products are predicted from heat-transfer analyses of the thrust chamber made in the design of insulation and nozzle systems. These time histories for propellant and inert mass and balance are combined (as in ref. 103) with those of the hardware in separate predictions for the total motor.

2.3 Evaluation of Propellant Performance Parameters

To predict accurately the performance of a solid-propellant rocket motor by the aforementioned techniques, the values for propellant deliverable specific impulse, burning rate, and density must be determined. Analytical estimates are sometimes applicable; however, demonstrated characteristics generally are used in evaluating these parameters. Demonstration of the first two parameters usually is accomplished in ballistic evaluation motors (BEM's). These motors do not duplicate exactly all conditions that will exist in or with the full-scale motor; thus it is necessary to adjust or scale the test results. To make these adjustments correctly, the dependence of the parameters on propellant and motor characteristics and operational environments must be established by using analytical techniques that combine theory and empirical relationships.

2.3.1 Specific Impulse

A significant fraction of the theoretical specific impulse I_{sp}^o of a solid propellant is not delivered when the propellant is fired in a motor. This is illustrated by the data presented in figure 16, which also points out a dependency of delivered impulse on mass flowrate and thus on motor size. Therefore, to predict motor performance accurately, a deliverable specific impulse I_{spd} must be determined and used. I_{spd} is defined as the ratio of the sum of the forces acting on the rocket thrust chamber to the flowrate of the mass being discharged. I_{spd} is dependent not only on nozzle performance and ambient pressure conditions but is significantly dependent on (1) available combustion energy of the propellant; (2) energy lost from the combustion gases to the motor hardware; (3) extent of velocity and thermal equilibrium attained between the gaseous and solid phases of the exhaust products during flow through the nozzle; (4) combustion efficiency, i.e., the relative completeness of combustion in the motor chamber; and (5) contribution of discharge-inerts. In assessing these dependencies and establishing performance efficiency factors for prediction of full scale motor performance, the ideal rocket often is used as a basis for comparing and evaluating demonstrated performance. In so doing, characteristic velocity c^* and thrust coefficient C_F are used to evaluate the influence of the combustion chamber and nozzle, respectively. Specific impulse can be expressed as

$$I_{sp} = c^* C_F / g_c \quad (33)$$

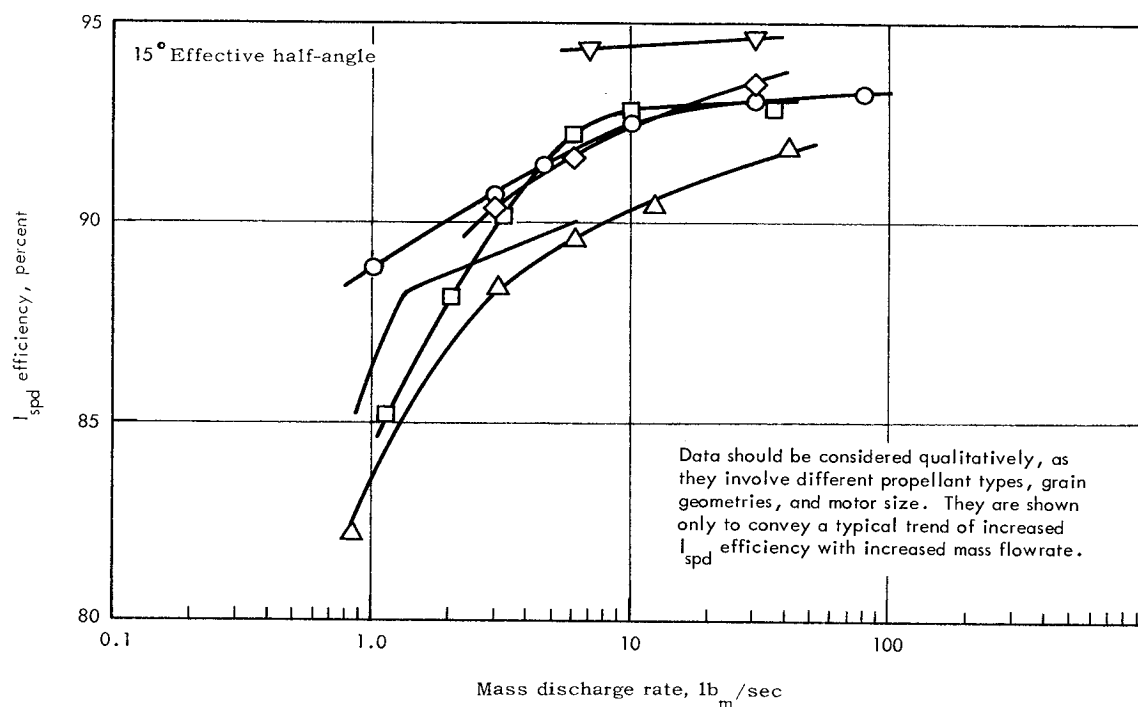


Figure 16.—Typical effect of mass flowrate on test motor I_{spd} efficiency (ref. 27).

The specific impulse of a propellant system in a one-dimensional perfect thrust chamber—predicted by utilizing Gibbs' minimization of free energy, assuming a shifting equilibrium and only a gaseous medium—often is used as the maximum theoretically achievable value I_{osp} . References 52 and 92 provide brief but comprehensive reviews of computer programs used by industry to calculate this idealized, theoretical performance. Analytical prediction of deliverable specific impulse must treat the aforementioned dependencies and finite chemical reaction kinetics. However, because of the complexity of these predictions and the many uncertainties associated with identifying these dependencies, it is common practice to demonstrate deliverable performance by BEM tests. Specific impulse values are qualified in accordance with the definitions set forth in the Glossary.

2.3.1.1 Analytical Prediction

Some organizations utilize empirical relationships to adjust I_{osp} by a single efficiency factor; some degrade I_{osp} by efficiency factors based on demonstrated values such as those in figure 16 or on separate detailed nozzle and flow analyses, e.g., Hoffman (ref. 104) and Crowe et al. (refs. 39 and 105); while some programs combine thermal energy conversion calculations with portions of the detailed flow analysis. For the latter approach, two programs have been prepared by Kliegel et al. for the analytical

prediction of specific impulse of two-phase media. The first is a one-dimensional two-phase reacting-gas nonequilibrium performance program (ref. 48), and the second treats an axisymmetric two-phase flow assuming a perfect gas (ref. 51) (i.e., the gas-phase expansion is treated as having a constant molecular weight and specific heat ratio). The one-dimensional program is completely self-contained, requiring specification only of the propellant properties (elemental composition and heat of formation), relaxation rates, and nozzle geometry. The program allows simultaneous consideration of both chemical and gas-particle relaxation losses in propellant systems having condensed exhaust products. The program is written in FORTRAN IV and allows equilibrium, frozen, and kinetic performance calculations to be performed during a single machine run.

Figure 17(b) is a plot presented by Kliegel (ref. 58) to compare the one- and two-dimensional predictions of I_{spd}^o/I_{sp}^o for the nozzle configuration shown in figure 17(a). The efficiency difference was attributed largely to the fact that particles separate from the wall and gather in the core of the gas flow, resulting in slightly less performance than in a one-dimensional fully flowing nozzle. Kliegel and Nickerson (ref. 50) reported this difference to be about 0.7 percent in conical nozzles. For the same nozzle configuration, figure 17(c) shows that the particle lags cause an appreciable loss of I_{sp} in the nozzle and that most of this loss occurs upstream of the nozzle throat; hence, the large loss at the throat. The one-dimensional constant-fractional-lag estimate of I_{sp} loss made in reference 58 is excellent for the throat and fairly good for the rest of the nozzle.

Figures 17(d) and 17(e) present some of the comprehensive comparisons made in reference 50 to evaluate for conical nozzles the effects of nozzle geometry on I_{spd}^o in small solid propellant motors. Kliegel (ref. 58) concluded from these tests that of all nozzle design parameters the nozzle throat radius of curvature has the greatest effect on delivered specific impulse. Limited investigations have indicated that values of R^*/R_t between 1.0 and 0.3 have little effect on I_{spd} efficiency. Mass discharge coefficient C_W , however, continues to decrease with reduced R^*/R_t and approaches a value of 0.85 when R^*/R_t approaches zero (the condition for a sharp-edge orifice).

With the exception of Kliegel's one-dimensional nonequilibrium program (ref. 48), the analytical prediction of deliverable specific impulse of a two-phase medium is made by degrading I_{sp}^o calculated with the assumption of infinite-rate shifting equilibrium. Typical thermo-chemistry programs (refs. 85 and 86) calculate I_{sp}^o by combining equations (2) and (3) to get

$$I_{sp}^o = u_e/g_c + \left(\frac{P_e - P_a}{\dot{m}} \right) A_e \quad (34)$$

With an ideal nozzle and vacuum operation, the equation reduces to

$$I_{spvac}^o = u_e/g_c + \frac{P_e A_e}{\dot{m}} \quad (35)$$

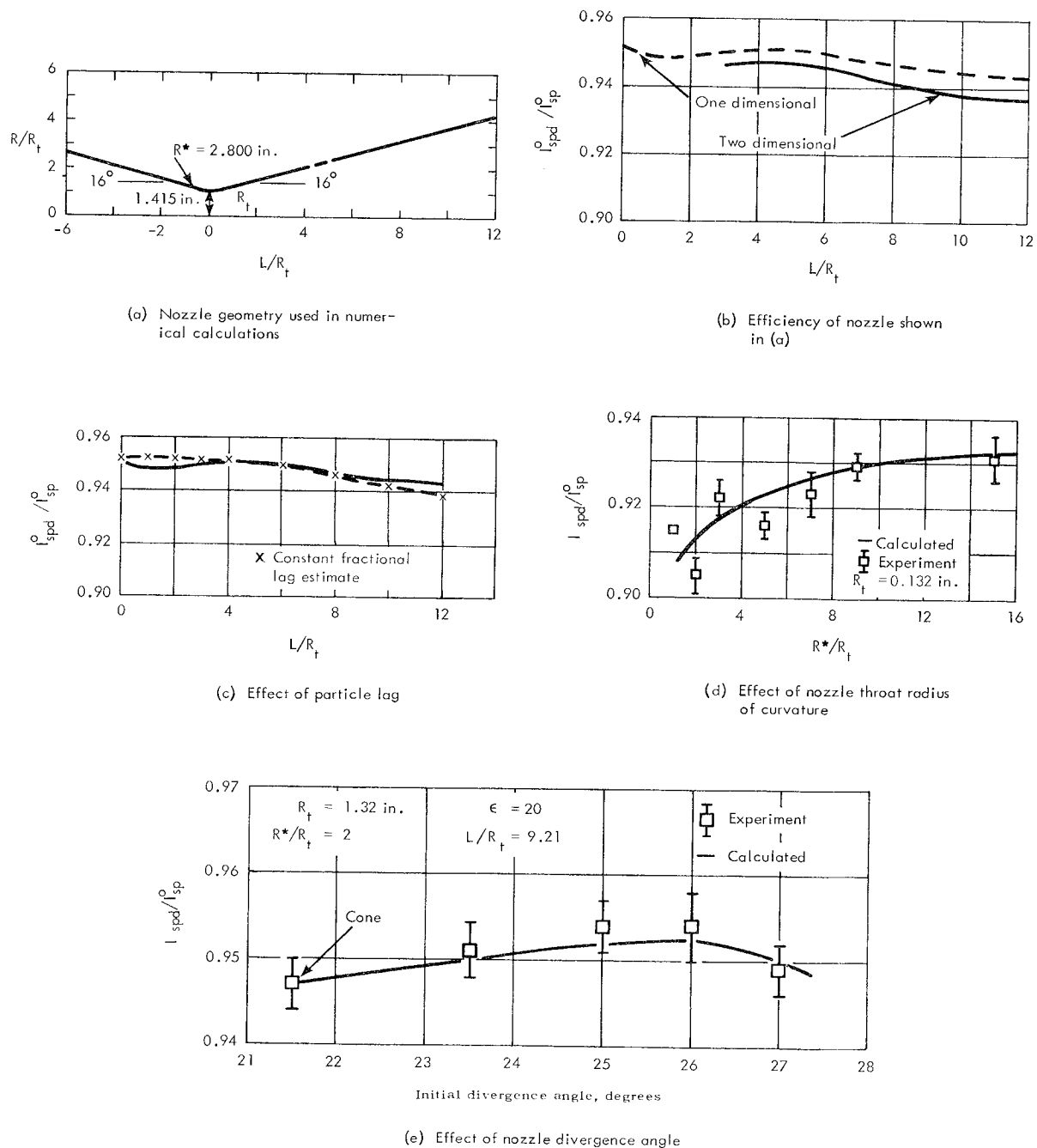


Figure 17.—Typical effects of nozzle parameters on test motor I_{sp} efficiency (adapted from ref. 58).

The velocity of the gas u_e is obtained by using

$$u_e = \sqrt{2J(H_c - H_e)g_c} \quad (36)$$

where J is the mechanical equivalent of heat, 778.2 ft-lb_f/Btu.

The ratio of A_e/\dot{m} is obtained from the mass flowrate equation

$$\dot{m} = \rho_e A_e u_e \quad (37)$$

where the density of the gas ρ_e is obtained from the equation of state.

As reviewed briefly in reference 27, the enthalpy in the chamber H_c is evaluated by an iterative procedure in which the temperature in the chamber T_c is varied until the enthalpy of the products H_c is equal to the potential enthalpy of the propellant H_p . Each time a new temperature is selected during the iteration, the chemical composition is determined so that the total free energy or Gibbs function of the combustion products is minimized. The chamber pressure P_c is held constant during the iteration process. After the chamber temperature has been determined, the entropy S_c of the mixture is calculated.

To find the static enthalpy H_e of the gas mixture at the exit conditions, the exit pressure P_e is set and isentropic expansion along the nozzle from the chamber to the exit plane is assumed. The exit temperature T_e is varied so that the entropy at the exit S_e is equal to the entropy in the chamber $S_e = S_c$. Whenever a new exit temperature is selected during the iteration, the chemical composition is determined by minimizing the total free energy.

For performance predictions, these theoretical values are adjusted to account for nozzle and motor losses and thus reflect deliverable specific impulse values. Adjustment is by one of two approaches. The first, and most simple, is to use a single correction factor that is based on historical performance data. This correction factor would reflect the characteristics shown in figure 16 and would be based on delivered performance for motor designs that incorporate similar grain and nozzle designs, propellant formulation, and motor size. If data are available, this can be a very successful technique.

The second and more complicated approach to adjusting $I_{o,sp}$ is to predict deliverable thrust coefficient and characteristic velocity efficiencies. Section 2.1.3.2.1 reviews the deliverable thrust coefficients that are calculated by using the gas-dynamic analysis techniques, particle size, drag coefficients, etc. (i.e., as used in refs. 39, 105, and 106.) Losses in the combustion chamber and upstream of the nozzle throat that affect characteristic velocity are attributed to a combination of combustion inefficiency, particle lag, and heat loss; particle lag and heat loss are also reviewed in section 2.1.3.2.1. Combustion efficiency has proven very difficult to predict. Crowe et al. have found combustion efficiency to be very sensitive to residence time and pressure as shown in figure 18.

Figures 18 and 19 (from ref. 105) depict experimentally determined correlations between specific impulse efficiency and motor chamber pressure and between specific

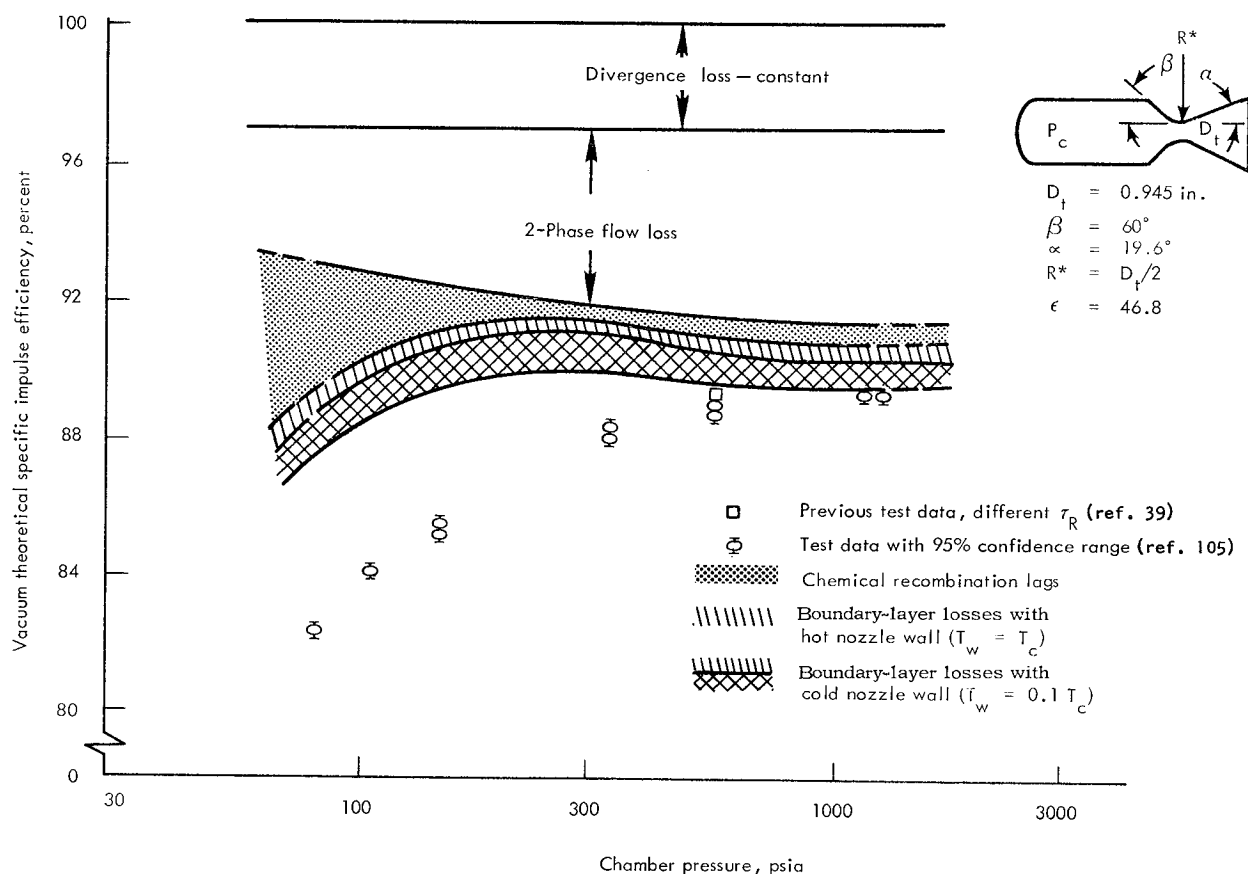


Figure 18.—Typical effect of chamber pressure on vacuum specific impulse efficiency (adapted from ref. 105).

impulse efficiency and motor size. Regarding chamber pressure sensitivity (ref. 87) (fig. 18), the following were noted analytically: (1) divergence losses λ are constant; (2) two-phase losses increase with pressure, as a result of increased particle size (figs. 9 and 10); (3) based on Bray's sudden freezing criterion (ref. 87), recombination losses decrease with pressure and approach a constant magnitude indicating reactions were nearly complete when the composition froze; and (4) boundary-layer and heat losses decreased slightly with increased pressure. It was shown that, for geometrically similar nozzles, the decrease in I_{sp} (ΔI_{sp}) resulting from boundary-layer and heat losses varies inversely with R_t and P_c according to the relationship

$$\frac{\Delta I_{sp}}{I_{sp}} \approx \frac{1}{(P_c R_t)^{0.2}} \quad (38)$$

Theory and experiment agreed at high pressure levels. At lower levels, however, demonstrated performance was considerably less than predicted performance. Crowe

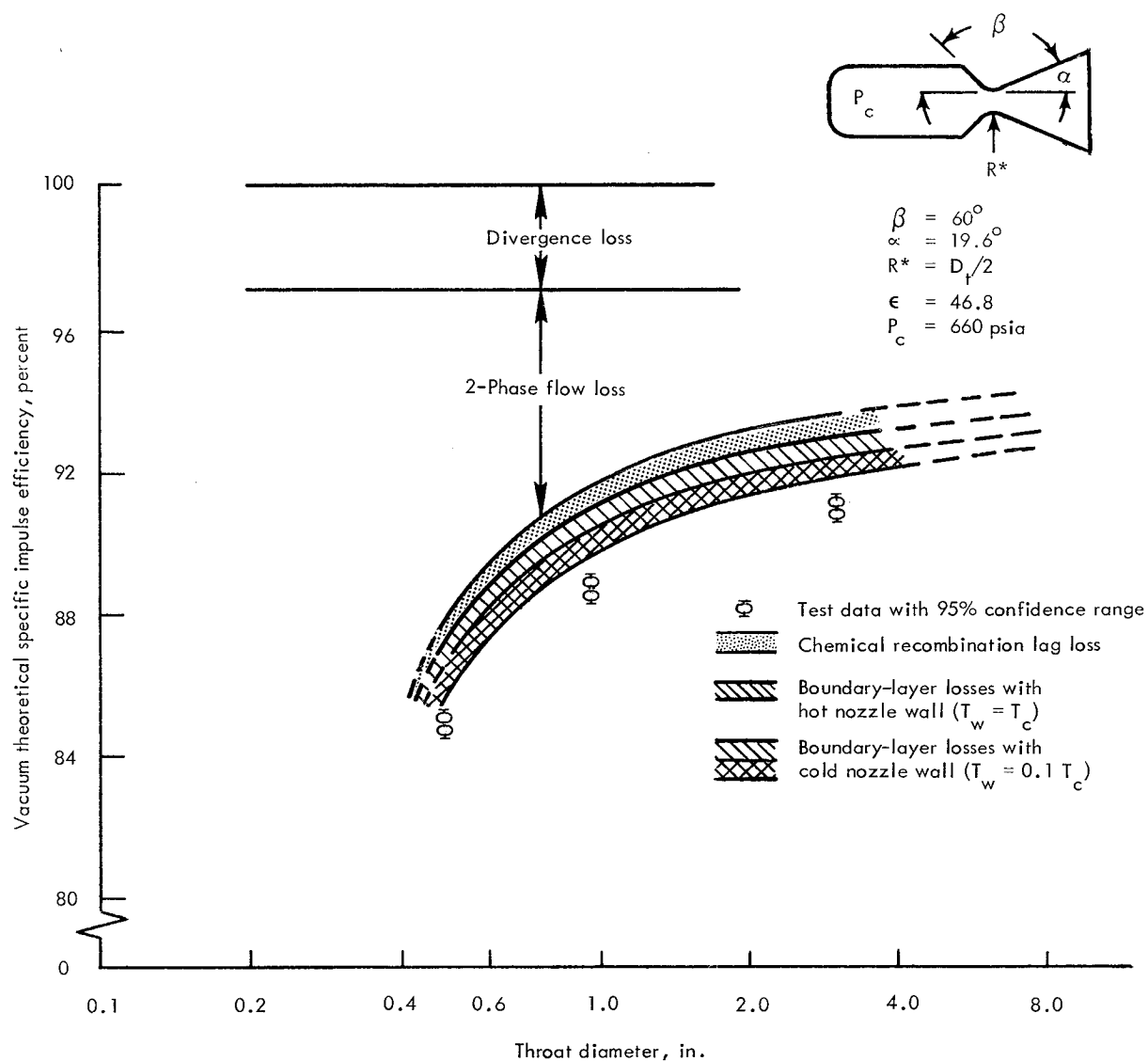


Figure 19.—Typical effect of motor size on vacuum specific impulse efficiency (adapted from ref. 105).

concluded that residence time (the time the gases and metal particles reside in the chamber during combustion process), defined as

$$\tau_R \equiv \frac{\rho_g V_c}{\dot{m}_g}, \text{ sec} \quad (39)$$

was the factor contributing to this additional loss. In these tests, the chamber volume was increased to increase burning surface and operational pressure levels; this volume

increase also resulted in an increased residence time. Short residence times, corresponding to the low pressure levels in figure 18, implied incomplete combustion. This is corroborated further by Crowe's earlier data (ref. 39 and fig. 18). These data are for the same propellant and nozzle geometry and scale, but the residence time was 1.75 times as long and therefore permitted more complete combustion of the aluminum particles. Analytical models and techniques are not satisfactory for predicting combustion efficiency for all types of propellant, although a correlation in combustion efficiency between strands and small motors has been reported (ref. 40). Combustion efficiency is thus determined experimentally from small test motors.

At constant chamber pressure, the degradation in specific impulse and the relative magnitudes of the various losses have been shown analytically and experimentally (refs. 27, 45, 105, and 107 through 109) to be highly dependent on motor size and mass flowrate (fig. 16). Crowe et al. (ref. 105) computed the loss breakdown over the nozzle-throat-diameter range shown in figure 19. The 0.485-in.-throat-diameter motor used a 5 lb end-burning grain; the 0.945-in.-throat-diameter motor used a 5.4-lb cylindrical port burner; and the 3.04-in.-throat-diameter motor contained 250 lbs of propellant in a cylindrical port burner. Crowe attributes the improvement in performance to the higher degree of gas-particle equilibrium that results from the lower gas velocity and the more gradual temperature gradients produced by increasing the size of the motor. As a result of these variations in efficiency, the selection of size for small BEM's has been a critical factor in establishing satisfactory techniques for scaling demonstrated propellant performance.

2.3.1.2 Demonstration

Three basic techniques are employed in the experimental evaluation of specific impulse of a propellant: the small rocket motor, the closed-bomb, and the pinwheel tests. The latter two generally are limited to use in propellant research (ref. 110).

2.3.1.2.1 Specific Impulse BEM Characteristics

Small BEM's typically are fired during the final phase of selecting a propellant for use in a particular motor design. In some instances they are scaled replicas of the full-scale motor. This has been the practice in the design of extremely large solid propulsion systems (ref. 111). However, more often than not, the specific impulse predicted for a propellant is based on performance demonstrated in a small BEM of simple design. Characteristically, these evaluation motors are similar to those used by the Air Force for the BATES motor (ref. 112) and to those recommended by the ICRPG Static Test Working Group (ref. 27).

2.3.1.2.2 Specific Impulse Scaling

As previously discussed, propellant I_{spd} is greatly dependent on design characteristics and operational conditions of the motor in which the propellant is used. This dependency often necessitates scaling small-motor delivered specific impulse before

analyzing and predicting the full-scale motor performance. References 45 and 105 report the results of rather extensive tests conducted to determine the primary considerations in scaling motor specific impulse. The significant factors that require adjustment are losses resulting from heat transfer, two-phase flow, and nozzle divergence. Smith et al. (ref. 113), using the basic approach recommended in reference 45, scaled up the BATES motor performance to levels comparable to the I_{sp}^o and I_{spd} values demonstrated in large motors (156- and 260-in. diam.). They concluded that "calculated two-phase flow losses, when combined with nozzle-divergence losses and experimentally determined heat-transfer losses on the BATES motors, correctly account for the difference between theoretical and delivered specific impulse. Finally, scaling these losses to large motors provides a satisfactory means of estimating delivered performance."

In assessing individual losses, one of the aforementioned two-phase flow analysis programs is used to evaluate both motors. Heat loss is predicted analytically although it is often measured for the BEM. The magnitude of inert products discharged during motor firing is predicted by heat-transfer analyses. Empirical values often are used for the specific impulse of this discharging inert material. Values for $(I_{sp})_{inert}$ range from 120 to 200 lb_f-sec/lb_m and are dependent on the oxidation ratio, i.e., the oxygen available within the chamber to support combustions of inerts. One accepted practice for inert liners having the same binder as the propellant is to use one-half the value of the propellant's specific impulse. Gordon (ref. 114) developed an expression to relate insulation loss due to pyrolysis or erosion to the increase in deliverable specific impulse.

2.3.2 Density

Thrust and impulse are direct functions of the flowrate of the mass being discharged by a rocket motor. For accurate performance predictions, the density of the propellant generating this discharging mass must be known. Propellant density is determined from samples of the propellant being used in the motor design under analysis by one of the following general methods for measuring density of solids:

- (1) Weight/volume method: A propellant specimen is cut to specified dimensions and weighed. This weight is divided by the volume calculated from the specific dimensions to determine propellant density.
- (2) Liquid-displacement method: A temperature-conditioned propellant sample of predetermined weight is immersed in a liquid. The volume of the sample then is calculated by dividing the weight of the displaced liquid by the specific gravity of the liquid at test temperature. Density is the quotient of sample weight and volume.
- (3) "Sink-float method" (ref. 110): A sample is immersed in a series of solutions of $ZnCl_2$ differing in specific gravity by 0.002 g/cc. The specific gravity of the sample is greater than the solution in which the sample sinks and less than the solution possessing the next higher specific gravity in which the sample floats.

The first two techniques are most commonly used.

2.3.3 Burning Rate

Propellant burning front progression rate r_b is an empirically determined function of propellant composition, conditions within the combustion chamber, and vehicle dynamics. Pertinent combustion-chamber conditions include pressure, initial propellant temperature, combustion-product temperature, and the velocity of the gaseous combustion products parallel to the grain surface. Appreciable vehicle spin, velocity of combustion gases, or chamber pressure variations can augment the basic rate. Burning-rate values used in propellant performance predictions are based either on rates demonstrated in small BEM's or on empirical relationships correlating linear and augmented rates that are applicable to the particular propellant formulation.

2.3.3.1 Linear Burning-Rate Characteristics

Dependencies of burning rate on propellant formulation, temperature, and chamber pressure during steady-state burning are termed "linear burning-rate characteristics." Three common experimental methods are used for measuring burning rates of solid propellants: the closed bomb, the small BEM, and the strand burner. The closed bomb provides burning characteristics under a constant-volume condition, but pressure varies over a wide range during a single firing. Thus, instantaneous burning rates obtained with this technique require many approximations and assumptions. As a result, the use of this technique generally is confined to preliminary screening or propellant research (refs. 107 and 110). The other two techniques are used extensively in the development of solid propellant rocket motors when the absolute level of burning rate must be determined as the basis for an accurate prediction of motor performance. In predicting burning rates for propellant in a particular motor design, the current practice is to demonstrate the linear burning rates over the operating range of the motor by utilizing the small BEM. The third technique, the strand burner, is reserved for propellant screening and quality control testing.

2.3.3.1.1 Burning-Rate BEM Characteristics

Small BEM's used throughout industry for burning-rate determination differ considerably in grain design, motor size, and burning duration. Grain geometric shapes include (1) internal-external burning tube without inhibitor; (2) internal-burning cylinders, possibly with restricted ends that can be case-bonded or suspended with outside diameters restricted; and (3) an external-burning slab. For the determination of basic linear burning-rate characteristics, the motors are typically from 2 to 6 inches in diameter; and the grain is designed to produce a rather neutral pressure-time trace with sharp tailoff characteristics. The port-to-throat area ratio generally is greater than 6 to maintain the gas flow below the threshold value for erosive burning.

The burning rate obtained from this neutral burner corresponds to a single motor operational pressure and temperature. For complete identification of linear burning-rate characteristics, small motor tests are fired over the pressure and temperature operational ranges specified for the full-scale motor. If proper experimental and data reduction techniques are used in determining these linear burning rates, the $P-r$ and π_K data obtained in small BEM tests do not require significant scaleup (refs. 45, 103, 115, 116). References 45 and 103 critically review discrepancies between demonstrated small BEM test and large motor test rates and conclude that the primary cause of disagreement is the improper definition of the burning time of the small motors. In these two references, the small motor "web burnout point" was determined by the widely used tangent-bisector method. References 117 and 118 recommend defining web burnout as occurring at the point of maximum rate of change in curvature near the onset of pressure tailoff. A test technique occasionally used to produce a very sharp tailoff is that of water quenching (ref. 119).

It is recognized that not all the physical phenomena involved in burning-rate scaleup have been identified and assessed by current technology. Some investigators have found that linear burning rates demonstrated in BEM's must be scaled 5 to 7 percent to predict and correlate with full-scale motor rates. In these instances, the diameters of the full-scale motors were an order of magnitude larger than those of the ballistic motors. The greatest scaling values required for correlation were obtained from full-scale motors using fiber glass cases where changes in grain web thickness accompany grain bore and case expansion upon motor pressurization. Another strain-inducing factor is propellant thermal shrinkage that occurs at temperatures lower than the apparent strain-free temperature. Both strain-inducing phenomena typically lead to a slight reduction in propellant grain web and frequently to an increase in exposed burning surface. Failure to acknowledge this reduction in web and increase in burning surface accentuates the apparent scaleup factor. However, even when these slight changes in effective web are properly treated, some scaleup remains. This has been shown by back-calculating motor performance using conventional ballistic relationships and maximum values for all related parameters. From these calculations, the lack of proper burning-rate scaleup has been the only logical explanation of deviations observed between measured and predicted motor performance.

Some small motors are designed purposely to produce progressive or regressive pressure-time traces. From such a trace, attempts are made to evaluate the burning rate over a range of pressures. Motor tests are conducted to provide some overlapping rate data. This technique has been used by some to reduce the number of small motor tests (ref. 120). Although this is an economical technique, an accurate assessment of linear burning-rate pressure exponent is not provided.

The number of tests required to identify propellant pressure and temperature dependencies is based on the degree of confidence desired for performance predictions, the type of small test vehicle being used, and the operational envelope of the full-scale motor.

When a solid propellant with a given temperature-conditioned grain is burned in a vented vessel and exhibits a straight-line relationship between log burning rate and log pressure, the propellant can be characterized by de Saint Robert's burning-rate equation (eq. 11). The exponent n is the slope of this straight line (fig. 20). However, for many propellants, the value of n deviates greatly in various pressure regimes. Two types of propellants with variable values for n are illustrated in figure 21.

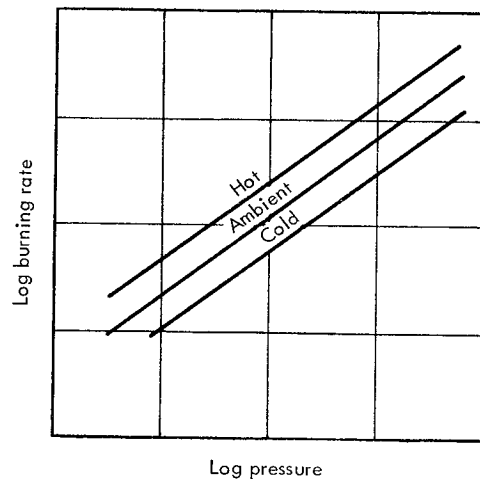


Figure 20.—Burning-rate/pressure relationship for propellants for which $r = aP^n$.

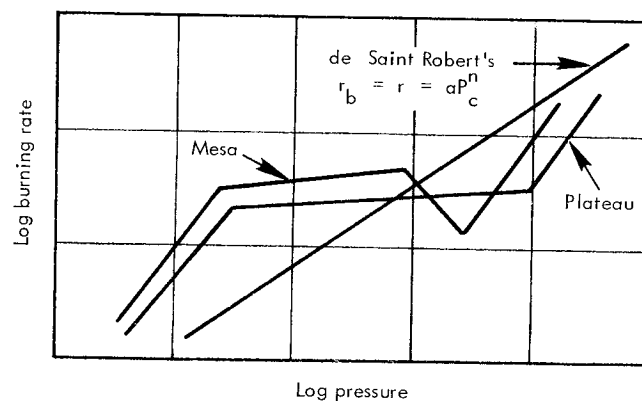


Figure 21.—Burning-rate/pressure relationship for three types of propellants.

Propellants showing a region of markedly reduced n are known as "plateau" propellants. Certain double-base propellants containing small amounts of lead compounds and some polymer binder/ammonium perchlorate composites exhibit a reduced n . Lead compounds increase the burning rate in the plateau region and at

lower pressures; without the lead, the propellant would show a normal curve coinciding with the high-pressure branch of the plateau propellant's curve and continuing normally into the lower pressure region (ref. 121). The mechanism of plateau formation has not been fully clarified.

Propellants that show negative values of n over short pressure ranges are known from the shape of the curves as "mesa" propellants. In the region of negative slope, if the pressure increases as a result of sudden exposure of additional burning surface or partial constriction of the throat, the rate will drop immediately to restore the balance. The close approach of the isotherms also contributes to a low temperature coefficient of performance for vented vessels designed to operate in this region. Crossing of isotherms indicates a region of negative temperature coefficient.

Although the basic propellant composition is selected during the early design stages, detailed analyses may show that it is necessary to control burning temperatures and rates independently to meet, simultaneously, performance limits and envelope requirements. Therefore, propellant compositions usually contain additives, termed "burning-rate modifiers," that alter burning-rate characteristics. The choice and quantity of these modifiers are determined experimentally. In addition to altering linear burning characteristics, a modifier can alter propellant temperature coefficients and erosivity constants.

2.3.3.1.2 Strand Burning Rates

In strand burning-rate tests, a long and relatively slender section of propellant, in which wires have been embedded at specified intervals, is burned in an inert atmosphere. The sides of the propellant section are inhibited to permit burning on only the end of the specimen. The embedded wires have a relatively low melting point and are connected to a timing circuit. As the strand burns, in cigarette fashion, the time required to burn from one wire to an adjacent wire can be measured, thus establishing a burning rate. Strands are conditioned to the desired temperature and burned in a closed chamber in which pressure can be closely controlled by utilizing a large surge tank in series with the chamber. Pressure rise in the chamber is held to a minimum, permitting the burning rate to be determined at a near-constant pressure. Sometimes thermocouples are used instead of fuse wires; other conditions are unchanged.

An improved technique (ref. 122) is to notch the specimen rather than to insert wires or thermocouples. The notch produces an instantaneous reduction in burning-surface area and, therefore, a sharp drop in the pressure-time trace. A burning rate can be obtained with this trace and the known distance between notches. This method reduces test time and avoids some of the uncertainties believed to be associated with burning characteristics of the propellant in proximity to fuse wires or thermocouples.

Strand burners have been modified further to permit special types of burning; e.g., the uncured propellant is drawn into a soda straw and burned in the uncured state,

or the strands are burned under water or oil so that no external inhibitor is required to induce cigarette-type burning. The latter tests are particularly useful for quality control.

Strand burning-rate data are normally used for research, screening, preliminary development, and quality-control purposes. Reasonably good correlations between strand rates and rates demonstrated in test motors have been reported for the nitrocellulose-type propellants if the effect of gas erosion on the propellant is considered (refs. 122 and 123). There is less agreement with the composite-type propellants (refs. 115 and 116), although Hermance (ref. 123) and Herrington (ref. 124), by using Summerfield's granular diffusion flame model (ref. 125), have indicated that strand rates can be correlated with data taken from small motors. However, coefficients used in this expression must be determined experimentally for each propellant. Thus, the cured and liquid strands can be of great use in quality control and the prediction of motor performance when correlations have been established during the development program (reviewed in detail by Jacoby et al., ref. 126).

2.3.3.2 Augmentation of Linear Burning Rates

Linear burning rates increase under certain conditions. To predict accurately the performance of a solid propellant motor, comprehensive analyses must assess susceptibility to burning-rate augmentation and properly account for its effects. Conditions that affect burning-rate augmentation include gas flow, high pressure transients, vehicle acceleration, propellant strain, and propellant homogeneity adjacent to liner bondlines.

2.3.3.2.1 Effect of Gas Flow

The increase in burning rate produced by combustion products flowing over the burning surface of a propellant (figs. 1 and 2) has been termed "erosive burning." Numerous empirical and theoretically based relationships have been developed in attempts to assess this characteristic. With low port-to-throat area ratios, the influence of erosive burning becomes increasingly important in the aft end of the motor where mass flux is high and is critical in the prediction of the high pressure peak immediately following ignition. Failure to predict this maximum pressure can result in motor failure. Further, the nonuniform burning rate that occurs down the length of the grain can alter tailoff characteristics.

Comprehensive reviews of the work on this subject were prepared by the Jet Propulsion Center of Purdue University (refs. 17 and 18). From these, the current status of erosive burning of solid propellant rockets may be summarized as follows:

- (1) A totally successful method of obtaining experimental erosive-burning data has not been developed.
- (2) With either double-base or composite propellants,
 - (a) Slow-burning propellants are more erosive than fast-burning propellants;

- (b) There is a threshold gas velocity and mass flux below which erosive burning does not occur (figs. 1 and 2), but whether the threshold value is a real or an apparent effect is not known;
 - (c) The flame temperature of the propellant appears to have no effect on erosive burning; and
 - (d) The geometry of the propellant grain influences erosive burning.
- (3) The theoretical approaches to erosive burning are inadequate.

It was noted further that, although the effects of erosive burning are known, these effects are impossible to predict without the experimental data obtained under the operating conditions of the solid rocket motor. To compare accurately the erosivity of different solid propellants, the following experimental data must be known for each propellant:

- The effect of combustion gas velocity and mass flux on the burning rate of the propellant for different operating conditions.
- The influence of the geometry of the propellant grain on the burning rate.
- The effect of oxidizer particle size of the propellant (for composite and composite modified double-base propellants) on the burning rate of the propellant.

Finally, it was noted that theoretical approaches to erosive burning will remain inadequate until the combustion mechanism of solid propellants is understood.

2.3.3.2.2 Effect of Pressure Transients

Von Elbe (ref. 127) originally developed the following burning-rate pressure/transient relationship, which subsequently was modified by Paul et al. (ref. 128) and Parker and Summerfield (ref. 129):

$$r_b = aP_c^{n_c} \left[1 + \frac{k_{11} k_p^n}{c_p \rho_p (aP_c^{n_c})^2 P_c} - \frac{dP_c}{dt} \right] \quad (40)$$

where

- k_{11} = empirical proportionality constant
- k_p = thermal conductivity of propellant, Btu/hr-ft-°F
- c_p = specific heat of propellant, Btu/lb-°F

The three analyses cited differ only in the value assigned to k_{11} : Von Elbe uses 2.0, Paul et al. use 1.0, and Parker and Summerfield use 0.5. With chamber pressurization, the effective burning rate is higher than the steady-state burning rate for the corresponding instantaneous pressure. Likewise, with chamber depressurization the burning rate becomes less than for steady-state conditions. Numerous simplifying assumptions have been made in the development of equation (40); in addition, the constant k_{11} is determined experimentally for each application. Therefore, equation (40) is used with confidence only when the conditions being analyzed are similar to those for which data are available.

2.3.3.2.3 Effect of Spin

Burning-rate augmentation produced by the spinning of a rocket motor about its longitudinal axis has been the subject of a series of recent studies and experiments (ref. 23). Usually the spin tests were conducted on a specific motor or series of motors containing a given propellant. Examination of the test results in reference 21 reveals that acceleration level, orientation of burning surface to acceleration vector, and metal content and particle size have the most effect on the performance of the motor in the spin environment (figs. 22, 23, and 24).

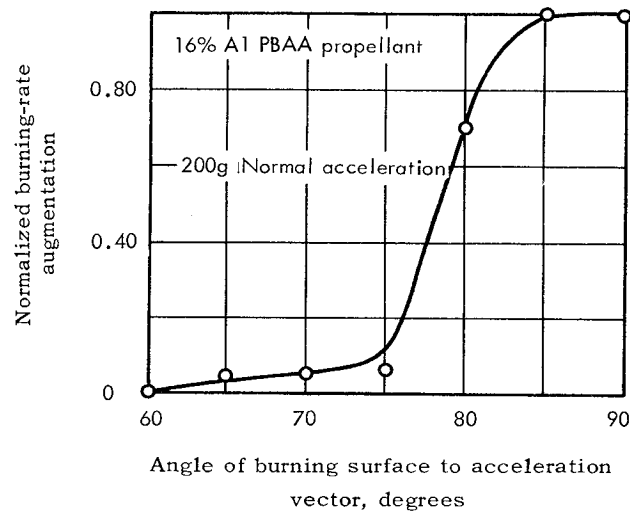


Figure 22.—Effect of acceleration direction on burning rate (ref. 21).

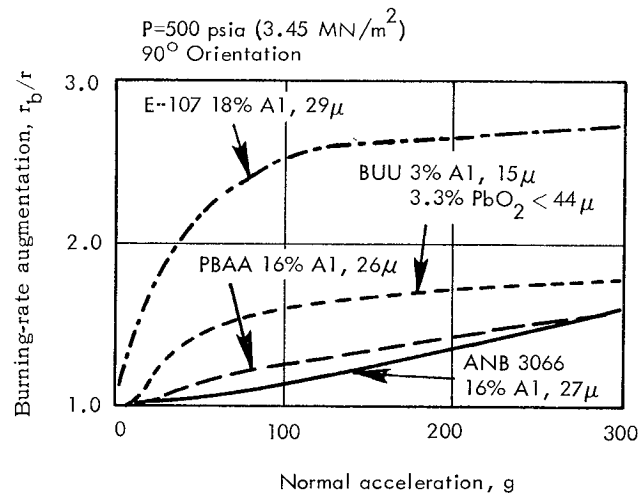


Figure 23.—Effect of acceleration on burning rate for different propellants (ref. 21).

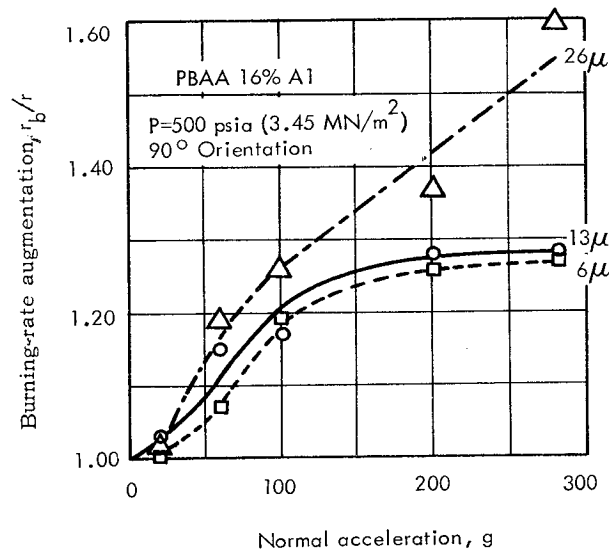


Figure 24.—Effect of aluminum particle size on burning rate (ref. 21).

In the test data plotted in figure 22, the propellant was a standard PBAA formulation containing 16 percent by weight of 10μ aluminum, and the motor firing pressures ranged from 500 to 600 psi. Propellant specimens were exposed to acceleration forces of 200 g at different angles with respect to the propellant surface orientation. A surprising and very significant result was that burning-rate augmentation was almost negligible at orientation angles less than 75° and nearly all the augmentation occurred between the angles of 75° and 90° .

As shown in figure 23, the propellant type, aluminum concentration, and aluminum and oxidizer particle size affected burning-rate augmentation. These data illustrate general trends that are associated with particle size. Figure 24 shows the effect of aluminum particle size on burning rate of a PBAA propellant containing 16 percent aluminum. Here, the propellant with the smaller aluminum particle size had less burning-rate augmentation than the others, showing that initial as-cast aluminum particle size, as well as oxidizer particle size, has a decided effect on ballistic performance.

The increase in burning rate is attributed to the presence of molten metal and metal oxide particles that are retained against the grain surface by the radial acceleration and cause a higher rate of heat transfer into the propellant. Further, there are apparent agglomerations of aluminum particles collecting on the propellant surface until particle sizes of 90 to 100μ are formed, even though a much smaller aluminum particle size is used in the propellant mix. The 90 to 100μ particle diameter is critical at a 20 to 25 g level in the motor and increases the burning rate by a factor of 1.45 for some propellants (ref. 66).

Whitesides and Hodge (ref. 130) recently have prepared a computer program on internal ballistics treating the effects of spin on pressure- and thrust-time histories.

However, as pointed out in section 2.1.2, much remains to be learned about the effects of spin on gas dynamics of the nozzle and the rocket motor combustion chamber. Quantitative assessment of the effects of acceleration on potential ballistic aberration is not yet a state-of-the-art technique; but the designer and analyst must be aware of the influence this environment can exert on the performance of solid rocket motors.

2.3.3.2.4 Effect of Strain

Studies with uniaxial tensile specimens have indicated that certain propellants exhibit an increase in burning rate because of strain (refs. 131 through 133). These studies, conducted with few propellant types, indicate that for certain propellants a strain-induced increase in burning rate occurs that has been related to the compressibility of the propellant, i.e., the value of Poisson's ratio decreases with induced strain. The more compressible the propellant (i.e., the greater the reduction in Poisson's ratio from the incompressible propellant value of 0.5) the more significant was the increase in burning rate. It should be noted, however, that a few tests revealed an opposite trend (ref. 133).

2.3.3.2.5 Effect of Bondlines

Recent studies with end-burning grain configurations have attributed pressure-time trace progressivity of supposedly neutral burning motors to burning-rate augmentation by bondline effects. Three primary suspects in contributing to this augmentation are (1) heat transfer along or from the backside of the liner to the propellant but ahead of the flame front, (2) concentration of fine particles adjacent to the bondline, or (3) chemical migration between propellant and liner. The latter has been identified as the principal augmenting factor. The region or depth of affected propellant typically is less than one-half inch. With internal-burning grains, the augmented burning rate leads to a pressure spike just prior to motor burnout and usually has little significance on the motor's ballistic performance. However, with end burners, as described in the design criteria monograph "Solid Propellant Grain Design and Internal Ballistics,"² the grain cones, and pressure is progressive from the onset of motor duration. Improperly designed liner/propellant bond interfaces have resulted in increases in propellant burning rate as great as 30 percent. With a pressure exponent n of 0.5 this increase would result in a 60 percent increase in chamber pressure, probably far in excess of motor case allowances. Various techniques have been used to negate chemical migration and bondline augmentation. The most successful to date are saturating the liner to the point where migration will not occur or incorporating, in the liner design at the bondline, a barrier that is impermeable to chemical diffusion.

²To be published as NASA SP-8076.

2.4 Prediction of Performance Variability

In predicting the propulsive performance of a motor, variations associated with the characteristics of the propellants and tolerances associated with the grain and hardware designs must be considered to ensure that the final design will comply with specified performance limits at the required confidence level.

2.4.1 Variables

In the final critical review of a motor design, the propellant parameter variations (demonstrated in small motor firings and dimensional tolerances and identified on detailed drawings) are used to determine the probability that the design will comply with specifications. Frequently, estimates of variations based on assimilated demonstration data, such as those shown in table III, are superior to variations derived from subscale motor tests. This is especially true if the BEM tests are not closely controlled or are very limited in number.

In table III the burning-rate variation was obtained from BEM data; the other parameters reflect typical variation for full-scale motors. It also should be pointed out that the variations themselves are dependent on propellant properties such as pressure exponent n and the coefficients σ_P , π_K . For example, the data in the table are for an $n = 0.2$ whereas, if $n = 0.5$, the burning-rate variation that would result in a 2-percent pressure variation would only be 1 percent. This results because $P_c \cong (r)^{1/1-n}$ and, if a given condition (1) is assumed to be the nominal, the variation condition (2) can be ratioed as $P_2/P_1 = (r_2/r_1)^{1/1-n}$.

Table III.—Ballistic Performance Variation Summary

Parameter	s/\bar{X}^a	Percent
Specific impulse	0.002	0.2
Propellant weight	0.0015	0.15
Action time	0.020	2.0
Inert weight	0.0059	0.59
Expended inert weight	0.11225	11.0
Total impulse	0.003	0.3
Average thrust	0.021	2.1
Instantaneous thrust	0.023	2.3
Pressure	0.020	2.0
Instantaneous pressure	0.027	2.7
Burning rate	0.020	2.0

^aExpressed as coefficient of variation s/\bar{X} , where s is an estimate of standard deviation and \bar{X} the population mean.

The propellant parameters requiring consideration include burning rate, pressure exponent, temperature sensitivity, and characteristic velocity. Specific impulse is influenced by both propellant and nozzle variations; thus, characteristic velocity and thrust coefficient generally are examined. Mean values for the variation about the mean for these parameters are determined by statistical analyses of the experimental data assuming normal distributions. Binomial, Poisson, and Students *t* distribution functions, as described in reference 134, are other distributions that may be used to evaluate experimental data.

Dimensional tolerances on grain web, slot width, length, burning surface, and port area contribute to performance variations by influencing grain geometry and weight. Thermal shrinkage of the propellant and grain and case deformation accompanying motor ignition pressurization also influence these geometric characteristics. Burning surface is influenced by (1) thermal shrinkage that accompanies a reduction in grain temperature, (2) expansion of the inner bore surface caused by ignition pressurization, (3) tolerances associated with restricted regions of the grain, and (4) the aforementioned geometric tolerances. Tolerances on the liner thickness, motor case inside diameters, and nozzle geometry are the inert component items that most significantly influence propulsive performance variability.

2.4.2 Prediction of Variations

Several mathematical techniques are used in combining tolerances to predict the performance variation associated with a given motor design. The simplest and the most restrictive from the standpoint of allowable tolerance is the summing of all tolerances. This method predicts maximum-maximum and minimum-minimum performance by simple addition or subtraction, respectively, of every possible tolerance as it would individually tend to increase or decrease performance.

A more common mathematical technique (refs. 103 and 135) is that of taking the square root of the sum of the squares of the tolerances of the individual parameters. This predicted variation represents the most probable combination of tolerances. A third technique is the more sophisticated, computerized "Monte Carlo" prediction, in which the computer has been programmed to select at random a point from the distribution of each variable in an expression. After many solutions of the expression utilizing this random sampling technique, a distribution for the solution can be generated.

3. DESIGN CRITERIA and Recommended Practices

3.1 Prediction of Pressure and Thrust Versus Time

3.1.1 Internal Flow-Field Modeling

Selection of the mathematical model used to simulate the motor internal flow field shall be based on the equations of continuity, momentum, and energy and on quasi-steady-state or transient gas dynamics.

One-dimensional gas dynamic models should be used to simulate the combustion chamber internal flow fields. Computer programs of the type documented in references 2 and 3 are recommended for general use. The program described in reference 2 is recommended for motors with relatively high length-to-diameter ratios characterized by a significant pressure drop down the length of the grain. The program described in reference 3 is recommended for motors with low length-to-diameter ratios where a three-dimensional geometric analysis is required. These programs calculate ignition, quasi-steady-state, and tailoff phases of motor operation. The equations of continuity,

$$\frac{\partial}{\partial x} (\rho u A) + \frac{\partial}{\partial t} (\rho A) = 0 \quad (41)$$

momentum,

$$\frac{\partial}{\partial t} (\rho u A) + \frac{\partial}{\partial x} (\rho u^2 A) = -A g_c \frac{\partial P}{\partial x} \quad (42)$$

(assuming flow along the x-axis, for example),

and the general conservation of energy,

$$T = T_c - \frac{(\gamma - 1)u^2 \bar{M}}{2 \gamma R_0 g_c} \quad (43)$$

are the basic gas dynamic and thermodynamic relationships used in predicting these internal flow fields. The following assumptions are basic in the application of these equations:

- (1) Mass addition occurs as an instantaneous process with no velocity component parallel to the motor axis.
- (2) The products of combustion obey the perfect gas law.
- (3) The gas flow is one-dimensional and adiabatic.
- (4) Combustion temperature, specific heat ratio, and molecular weight are constant throughout the motor.
- (5) Friction forces of the combustion gases in the port cavity are negligible.
- (6) Isentropic flow exists between the grain-exit and nozzle-entrance planes.

3.1.1.1 Quasi-Steady-State Performance

3.1.1.1.1 Uniform Pressure Within Combustion Chamber

Pressure and thrust predictions shall utilize the "equilibrium" pressure equation whenever the solid propellant grain configuration is such that the motor chamber pressure is essentially constant over the entire propellant burning surface.

The following expression for equilibrium pressure is recommended for use in thrust-time predictions (ref. 6, p. 239):

$$P_c = \left[\frac{A_b a_o \rho_c^*}{A_t g_c} \right]^{\frac{1}{1-n}} \quad (44)$$

Thrust should then be calculated by using equation (3). Equation (44) is valid if the magnitude of the time rate of change of chamber pressure is low enough to cause an insignificant effect on propellant ballistic characteristics, and the pressure over the entire burning surface is essentially constant. Equilibrium predictions are recommended with end burners and simply designed, ported grains with $L/D \leq 4 \leq A_p/A_t$. This generalized port-to-throat area ratio is dependent on the tendencies of the particular propellant toward erosive burning, and must be further qualified for long constant-diameter or tapered motor designs and for spherical and cylindrical motor designs in which relatively high gas velocities may be encountered locally in slotted regions of the grain. The susceptibility to erosive burning can be established from past experience with the formulation or from small motor tests. If the mass flux is above the threshold level, steady balanced-mass-flow analytical techniques must be used.

3.1.1.1.2 Nonuniform Pressure Within Combustion Chamber

Pressure and thrust predictions shall utilize the "steady-flow" gas dynamic equations whenever the solid propellant grain is such that a significant pressure drop along the axis of the grain exists or when the mass flux exceeds a threshold level.

For ported charges with a high volumetric loading, the method of incremental analysis should be used. The recommended procedure is to approximate a head-end pressure (using eq. (44) to calculate approximate value) and thus establish the gas generation conditions at that point (mass is being added to the flow at zero longitudinal velocity). The mass flowrate, port flow area, and approximated pressure are then used to predict the gas velocity and the mass being added in the second increment. These values, in turn, are used to determine the pressure and mass flow at the entrance to the third increment, etc. This is repeated for successive increments down the propellant cavity until a nozzle-entrance pressure is obtained. Nozzle-entrance stagnation pressure P_c should be predicted by using

both the momentum and continuity principles expressed in Bernoulli's equation for one-dimensional, isentropic gas flow (does not treat particle flow):

$$P_c = P_N \left[1 + \frac{\gamma - 1}{2} \frac{\bar{M} u_N^2}{g_c \gamma R_0 T_N} \right]^{\frac{\gamma}{\gamma - 1}} \quad (45)$$

(where N refers to a motor longitudinal station coinciding with the nozzle entrance plane) and the expression for the mass discharged through the nozzle throat is

$$P_c = \frac{c^* \dot{m}_t}{A_t g_c} = \frac{c^*}{A_t g_c} \left[p_p \sum_{i=1}^{i=N} \frac{(\Delta \text{vol})_i}{\Delta t} \right] \quad (46)$$

It is recommended that the two values for stagnation chamber pressure thus predicted agree within ± 0.5 percent. Thrust calculations should be made using the resulting stagnation pressure, the mass flowrate, and equation (3).

This incremental evaluation, summation, and comparison procedure is repeated for each interval of burn time for which values for thrust and pressure are predicted. Thrust- and pressure-time histories are generated from the plotted time summary of these values. The burn-time interval and magnitude of the increment of web consumed between evaluations should be selected after careful consideration of both required prediction accuracy and increased computation time and costs associated with increased frequency of evaluation.

3.1.1.2 Transient Performance

3.1.1.2.1 Ignition Transient

Pressure and thrust predictions shall account for the ignition transient whenever limitations on rate of pressurization are imposed on the rocket motor or when the firing duration of the motor is such that the impulse delivered during the ignition phase is a significant portion of the total impulse.

Ignition transient predictions should be made with the procedures given in reference 8. In differential form, the recommended expression for ignition pressurization is

$$\frac{dP_c}{dt} = \left[\dot{m}_{ig} + r_b \rho_p A_b(t) - \frac{P_c A_t g_c}{c^*} \right] \frac{R_0 T_c}{\bar{M} V_c} \quad (47)$$

assuming that

- (1) Combustion gas temperature and pressure are uniform throughout the motor.
- (2) Perfect gas laws are valid.
- (3) Igniter gas has same temperature and heat capacity as propellant gas.
- (4) Burning surface $A_b(t)$ is a function of flame propagation rate.
- (5) Only sonic conditions for nozzle discharge exist.

The igniter mass discharge rate m_{ig} should be predicted from an independent ballistic analysis of the igniter. Predicted values should be confirmed by igniter demonstration firings conducted in a large vented or closed-volume test chamber. The mass of combustion products being added from the main propellant charge, $r_b \rho_p A_b(t)$, should be calculated using the incremental element analysis. Burning-front progression rate r_b should combine influences of chamber pressurization, mass flux, grain temperature, and vehicle acceleration (see secs. 3.2.1 and 3.3.3.2).

3.1.1.2.2 Tailoff Transient

Pressure and thrust predictions shall account for the tailoff or bleeddown transient whenever limitations of the rate of depressurization are imposed on the rocket motor or when the motor operating pressure and chamber free volume are such that a significant amount of propellant mass is still in the chamber at the time of propellant burnout or at the onset of bleeddown.

When tailoff begins with significant propellant remaining in the chamber but is very rapid and the tailoff time interval is very critical, it is recommended that burning rate be based on Von Elbe's relationship (sec. 2.3.3.2.2). The empirical constant k_{11} should be determined from previous correlations with similar propellants and motor transient conditions. The relationship for predicting transient pressure thus will become

$$\frac{dP_c}{dt} = \frac{R_0 T_c}{\bar{M} V_c} \left\{ \rho_p A_b a P_c^n \left[1 + \frac{k_{11} k_p^n}{c_p \rho_p (a P_c^n)^2 P} \times \frac{dP_c}{dt} \right] - \frac{A_t P_c g_c}{c^*} \right\} \quad (48)$$

When tailoff or bleeddown begins with significant propellant remaining but the depressurization rate is not sufficient to influence burning rate, the linearized burning-rate characteristics should be used. Thus, if the linear rate is characterized by de Saint Robert's law, the transient-pressure expression will have the form

$$\frac{dP_c}{dt} = \frac{R_0 T_c}{\bar{M} V_c} \left[\rho_p A_b a P_c^n - \frac{A_t P_c g_c}{c^*} \right] \quad (49)$$

After propellant burnout, chamber pressure should be predicted by using equation (10).

3.1.2 Burning-Front Progression

Burning-rate relationships utilized in prediction of burning-front progression shall account for the effects of internal flow, propellant temperature, and motor dynamics.

Propellant burning-front progression rate should be calculated by using sections 3.1.2.1, 3.1.2.2, and 3.1.2.3. The necessary semi-empirical relationships should be developed from the results of propellant tests in small BEM firings as recommended in section 3.3.3.

3.1.2.1 Local Flow-Field Effects

Burning-rate relationships shall utilize locally predicted static pressure and gas mass flux.

If the gas velocity is greater than the experimentally established threshold level—figures 1 and 2 are typical examples—use an erosive burning relationship; if it is less than the threshold value, use a linear burning-rate relationship. Local static pressures should be used in both relationships. A suggested form for the expression of this threshold value is given by equation (17).

3.1.2.1.1 Linear and Semilinear Burning

Prediction of burning-front progression rate shall be based on linear or semilinear burning-rate expressions whenever

- (1) *The solid propellant grain configuration is such that the chamber pressure is essentially constant over the propellant burning surface.*
- (2) *The mass flux in the grain cavity is less than the threshold value.*

For “equilibrium” steady-state performance predictions, a burning-rate expression such as de Saint Robert’s law, $r = aP^n$, is recommended for use. If a plateau or mesa type of propellant is being used or if a composite propellant is being used at high chamber pressures, the coefficient a and exponent n should be expressed as functions of pressure and determined by recommendations in section 3.3.3.1.

3.1.2.1.2 Erosive Burning

Whenever the mass flux exceeds the threshold value, prediction of burning-front progression rate shall be based on the use of an empirical burning-rate equation that has been demonstrated to be applicable to the particular propellant being used.

It is recommended that the semi-empirical expression developed by Lenoir and Robillard (ref. 136) be used to treat erosive burning analytically. Their model

combines aspects of fluid flow and heat transfer and postulates a central core of flowing combustion gases surrounded by transpiring propellant walls. The augmentation term δ in equation (18) is related to heat flow acting through convection and thus is dependent on combustion-gas flowrate. The following burning-rate expression results:

$$r_b = r \{ 1 + [\alpha G^{0.8} \exp (-\beta r_b \rho_p / G)] / r L^{0.2} \} \quad (50)$$

where

β = proportionality constant in relationship between the heat-transfer coefficient h under conditions of transpiration and the coefficient h_0 for zero transpiration, i.e., $h = h_0 \exp (-\beta r_b \rho_p / G)$

α = proportionality factor = $(0.0288 k_g) c_p \mu^{0.2} Pr^{-0.667}$; results from postulation that $\delta = k_g h / r$ and utilizes the Chilton-Colburn expression for turbulent flow over a flat plate, i.e., $h_0 = 0.0288 G c_p Re^{-0.2} Pr^{-0.667}$

G = mass flux in grain port parallel to burning surface, $\text{lb}_m/\text{sec-in.}^2$

L = grain length, in.

However, empirical expressions of Kreidler and Peretz or Saderholm can be used effectively. These equations are fits of experimentally determined curves of burning rate as a function of pressure and mass flux and gas velocity. Figures 1 and 2, respectively, are typical examples. Kreidler's expression (ref. 16) (recently examined by Peretz (ref. 137)) is

$$r_b = a P^n \left[1 + \frac{k_1 (G - G_{tv})}{P^{k_5}} \right] \quad (51)$$

where

$$G_{tv} = k_2 + k_3 P^{k_4}$$

k_1, k_2, k_3 = experimentally determined coefficients

k_4, k_5 = experimentally determined exponents

Saderholm's (ref. 138) empirical expression has the form

$$r_b = r (M / M_{tv})^{k_6} \quad (52a)$$

for $M_{tv} < M \leq 0.5$, and

$$r_b = k_7 (M P_c)^{k_8} \quad (52b)$$

for $M > 0.5$,

where

k_6, k_7, k_8 = experimentally determined coefficient and exponents, respectively

M = Mach number

M_{tv} = threshold Mach number

A fourth alternate is a simple burning-rate/pressure/velocity tabular input to the computer program. The recommended computer programs (refs. 2 and 3) have the option of using any of these alternates plus others. In any event, the relationship or tabular input selected should be demonstrated to be applicable for the particular propellant being used, either by small motor tests (sec. 3.3.3.2) or by correlations with full-scale motor performance.

3.1.2.2 Temperature Effects

Prediction of burning-front progression rate shall account for thermal gradients across the grain web or for a wide range of operating temperatures whenever either is imposed by the rocket motor environment.

It is recommended that the effect of grain temperature on burning rate be predicted with the expression

$$a_o = a_{\text{ref}} \exp (\sigma_P \Delta T) \quad (53)$$

The reference burning-rate coefficient a_{ref} and the coefficient σ_P should be determined as recommended in section 3.3.3.1. The temperature increment ΔT is the difference between the firing and reference temperatures. It is recommended that the grain firing temperature be an input as a tabular function of web burned for firing conditions, aerodynamic heating, etc., in which symmetrical thermal gradients exist across the grain web. For complex grain cross-sectional configurations, thermal gradients are often nonsymmetrical. In these instances, the influence of temperature on surface progression should be evaluated graphically and the effects averaged over the grain length.

It is recommended that the effect of grain temperature on pressure be predicted with the expression

$$P_o = P_{\text{ref}} \exp (\pi_K \Delta T) \quad (54)$$

where

P_o = pressure at firing temperature, lb_f/in.²
 P_{ref} = pressure at reference temperature, lb_f/in.²
 ΔT = firing temperature minus reference temperature, °F

3.1.2.3 Motor Dynamic Effects

Performance predictions of a motor subject to high linear or angular accelerations during operation shall account for possible burning-rate augmentation and acknowledge possible gas dynamic effects.

It should be emphasized that there is an inadequate basis for accurate predictions of the influence of acceleration on motor performance. However, the effect of ac-

celeration cannot be ignored; and, to provide the best available basis for analytical treatment, the following recommendations are made:

The influence of longitudinal acceleration should be treated as in reference 2 and included in the steady-flow, incremental pressure expression developed in section 2.1.1.1. The influence of spin should be treated as a direct increase in linear burning rate as in equation (18), where δ is a function of propellant composition, spin rate, and burning-surface orientation (see sec. 3.3.3.2). In addition, the techniques developed and reviewed by Norton et al. (ref. 24) are recommended as guides for estimating the relative influence of spin on motor gas dynamics.

3.1.3 Nozzle Performance

The prediction of motor pressure- and thrust-time histories shall include the evaluation of the nozzle performance parameters (throat area and thrust coefficient) as functions of motor operation time.

The dependency of chamber pressure on the nozzle throat area is expressed by equation (44); equation (3) relates the instantaneous value of thrust-to-nozzle characteristics and chamber pressure. The variations in these parameters with motor operating time should be determined by the methods described in sections 3.1.3.1 and 3.1.3.2. These variations should then be provided as tabular functions of motor operating time for computerized predictions of pressure and thrust.

3.1.3.1 Area Variations

The analytical prediction of nozzle area variations during motor operation shall utilize demonstrated nozzle material performance data and characteristics of the exhaust gases.

In calculating motor ballistic performance, nozzle throat and exit area calculations can, with equal adequacy, utilize any one of the three techniques reviewed in section 2.1.3.1 for relating nozzle surface changes to motor operating time. Nozzle dimensions before motor ignition are obtained from detailed drawings. During motor firing, however, these dimensions may change as metal oxide deposition, thermal expansion, and nozzle erosion are induced by the flow of the high-temperature, two-phase exhaust products.

Instantaneous erosion or deposition rates should be determined from subscale or small-motor material evaluation firings conducted in the manner discussed in reference 111. In these tests, the species of exhaust gas, chamber pressure, and mass

flowrate per unit area should duplicate those expected in the full-scale motor. Lack of exact duplication of the latter two parameters can be approximated by scaling erosion rates, utilizing Bartz's (ref. 139) simplified equation for estimating convective heat-transfer coefficient:

$$\dot{\epsilon} = \dot{\epsilon}_{\text{mem}} (P_c/P_{c_{\text{mem}}})^{0.8} (D_{t_{\text{mem}}}/D_t)^{0.2} \quad (55)$$

where

$\dot{\epsilon}$ = instantaneous nozzle throat erosion rate, in./sec
 D_t = throat diameter, in.
 mem = material evaluation motor

Often the nozzle geometry and gas-particle flow patterns in the material evaluation motor differ from those of the full-scale motor. Therefore, erosion rates demonstrated in the small evaluation motor should be used only as inputs to detailed analytical predictions for full-scale nozzle surface regression. The methods for correlating these erosion rates and analytically predicting full-scale erosion rates should comply with the practices recommended in reference 32. As previously noted, there are no equivalent techniques for predicting or scaling deposition rates. Consequently, deposition is not treated analytically. Assessment of this phenomenon depends entirely on experimental observation.

3.1.3.2 Thrust Coefficient

Prediction of nozzle thrust coefficient shall account for the various flow regimes and other factors influential in converting thermal energy to kinetic energy.

Exhaust products, nozzle design complexity, size, and the similarity of the design to one for which performance has been demonstrated should be considered when selecting the method to be used for predicting thrust coefficient. If performance has been demonstrated in other motor system applications, this demonstrated nozzle thrust efficiency often is acceptable for use in a simplified analytical prediction of thrust coefficient as described in section 3.1.3.2.2. However, detailed gas-dynamic analytical techniques as recommended in section 3.1.3.2.1 are required for designs that are more complex, for which demonstrated performance data are not available or for which heat-transfer and structural analysis input data require detailed flow-field characterization. In the use of either approach, the influence of ambient back pressure and the occurrence of flow separation must be treated (sec. 3.1.3.2.3). The recommended computer programs (refs. 2 and 3) automatically treat the simplified analytical prediction and flow separation. Thrust coefficients predicted by means of the detailed gas-particle flow analyses are input in tabular form to the programs. The deliverable thrust coefficient is used in one of the following expressions to predict thrust-vs.-time histories:

$$F = P_c A_t C_F \quad (3)$$

or

$$F = \dot{m}_t c^* C_F / g_c \quad (56)$$

3.1.3.2.1 Detailed Analytical Prediction

Detailed analytical predictions of nozzle thrust coefficient shall account for losses in exhaust gas momentum attributable to nozzle divergence, two-phase flow lags, recombination, friction, and heat transfer.

Nozzle thrust coefficient should be predicted by numerical integration of the thrust function across the exit control surface, C-E, depicted in figure 3 (p. 16) and expressed numerically by

$$C_F = \frac{F_x}{P_c A_t} = \frac{\sum_C^E (\text{mass flow}) (\text{velocity}) + (\text{delta pressure}) (\text{area}) \times \vec{i}}{P_c A_t} \quad (57)$$

where \vec{i} is the unit vector in the x-direction.

The techniques reviewed in section 2.1.3.2.1 are recommended for calculating discharge and nozzle thrust coefficients.

3.1.3.2.1.1 Flow-Field Analyses

Gas-particle flow analyses used in the detailed prediction of thrust coefficient shall adequately evaluate subsonic, transonic, and supersonic flow regimes.

Programs prepared by Kliegel and Nickerson (ref. 50) and Hoffman (ref. 49) are recommended for analyzing the flow of gas-particle mixtures in conventional nozzle designs. These two programs assume inviscid, axisymmetric flow of two-phase, chemically nonreacting mixtures. The following general assumptions are characteristic: (1) the total mass and energy of the gas-particle mixture are constant; (2) the volume occupied by the condensed particles is negligible; (3) condensed particles do not interact, and shattering does not occur; (4) the internal temperature of the condensed particles is uniform, and thermal energy exchange between gas and particles is by convection only; (5) the only forces on the condensed particles are viscous drag forces, and the gas is inviscid except for its interaction with the condensed particles; (6) the gas obeys the perfect-gas law; and (7) the particles are spherical. Hoffman's analysis treats particles of three discrete sizes, whereas Kliegel's analysis approximates a particle size distribution by groups of different size (up to 10 discrete sizes) spheres. Kliegel assumes constant molecular weight and specific heat ratios, while Hoffman accounts for actual variations.

For nozzle designs with generous inlet characteristics, subsonic flow fields should be analyzed assuming one-dimensional, gas-particle flow (refs. 42 and 58) as in

the computer programs described in references 49 and 50. However, for subsonic gas-particle flow fields associated with submerged nozzle entrance sections, etc., two-dimensional steady-potential-flow theory (ref. 53) should be used to assess the entrance losses. Reference 140 presents details of this recommended treatment, and reference 34 presents several applicable semi-empirical expressions. Cold-flow model tests (ref. 111) should be conducted to support theoretical analyses of flow disturbance, particle concentration, and separation in the subsonic flow regime for extremely complicated nozzle entrance geometries. These tests use a gaseous medium. To evaluate entrance performance, static and stagnation pressures and mass discharge characteristics should be obtained in these tests.

Crowe et al. (ref. 39), Kliegel (ref. 58), Hoglund (ref. 42), and others have shown that one-dimensional, gas-particle flow analyses adequately predict the performance of conical nozzles. Data shown in figures 17, 18, and 19 are typical. Gas-particle flow analysis programs recommended for use with conical nozzles are described in references 42, 47, and 58.

3.1.3.2.1.2 Particle Characterization

For two-phase flow analyses, the characterization of metal oxide particles shall include particle size, drag coefficient, and convective heat-transfer coefficient.

Spherical particle shapes and a logarithmic normal size distribution should be assumed. With aluminized propellant, these have been substantiated by grab samples. Samples of beryllium fuel exhaust products, however, have indicated irregular particle shapes.

Unless particle size data are available for the propellant under analysis, the particle size data presented in figures 9, 10, and 11 are recommended for use in selecting a mean diameter. Residence time, chamber pressure, and throat size of the motor under analysis should be assessed with respect to these data. Crowe and Willoughby (ref. 63) in a recent comparison of particle size related mass-median diameter D_m , volume-mean diameter \bar{D}_v , and Sauter-mean diameter D_{32} and obtained the following correlations for a log-nominal distribution:

$$D_{32} = 0.88 D_m \quad (58a)$$

and

$$\bar{D}_v = 0.69 D_m \quad (58b)$$

A mass-median diameter based on these correlations is recommended for use in performance predictions (ref. 71). Delaney's maximum stable drop diameter model (ref. 62) and the data in figure 11 should be used to predict oxide coagulation or agglomeration. Two-phase programs currently available do not handle growth or shatter; therefore, maximum particle size should be used for a conservative per-

formance analysis. Particle drag coefficient should be expressed by Carlson's and Hoglund's (ref. 72) semi-empirical relationship for spherical shapes:

$$C_D = \frac{24}{Re} \left[\frac{(1 + 0.15 Re^{0.687}) (1 + \exp[(0.427/M^{4.63}) - (3.0/Re^{0.88})])}{1 + (M/Re)[3.82 + 1.28 \exp(-1.25 Re/M)]} \right] \quad (59)$$

where

M = Mach number
 Re = Reynolds number

In the two-phase flow analyses, two assumptions are made with respect to particle thermodynamics: (1) the internal temperature of the particle is uniform, and (2) the gas and particles exchange thermal energy by convection only. Further, Kliegel's program requires the assumption of constant specific heat. The recommended expression for Nusselt number Nu calculation is also taken from reference 72. This semi-empirical expression is

$$Nu = \frac{2 + 0.459 Re^{0.55} Pr^{0.33}}{1 + 3.42 (M/Re Pr) (2 + 0.459 Re^{0.55} Pr^{0.33})} \quad (60)$$

where Pr is the Prandtl number.

The convective heat-transfer coefficient is then calculated with the standard equation

$$h_c = \frac{k Nu}{D} \quad (61)$$

where

h_c = convective heat-transfer coefficient, Btu/hr-ft²-°F
 k = thermal conductivity, Btu/hr-ft-°F
 D = diameter, ft

3.1.3.2.1.3 Recombination Losses

Prediction of recombination losses shall utilize finite chemical reaction rates and one-dimensional flow analyses.

Currently, there are no actively used analytic techniques for predicting finite-rate performance loss for two-dimensional two-phase flow. To assess the performance degradation resulting from finite-rate chemical kinetics, a one-dimensional two-phase flow program such as that prepared by Kliegel et al. (ref. 48) is recommended. This program performs exact step-by-step integration of equations that describe an arbitrary set of relaxation or recombination processes. The enthalpy and composition of the expanding nonequilibrium gas flow can be found at any point in the nozzle with the solution of these equations. Input chemical data,

i.e., enthalpy, heats of formation, and specific heats, should be from the JANAF tables (ref. 141). Relaxation rates may be obtained from sources such as reference 142.

A recommended alternate is the use of a program (ref. 39) in which the flow is assumed to be in complete equilibrium up to some station in the nozzle—the freezing point—whose location is determined by comparing the available rates of chemical reaction to the rates required to keep the flow in equilibrium. Beyond the freezing point, the flow is considered to be completely frozen; that is, no further composition change takes place. The transition from equilibrium to frozen flow should logically take place quickly because the reaction rates are very sensitive to changes in density and temperature. This sudden-freezing approximation was originally discussed by Bray (ref. 87), who demonstrated that only small fractional changes in composition, density, temperature, and velocity occur in the transition region. In figures 18 and 19, the results of Crowe et al. (ref. 105) using this approach are presented as functions of chamber pressure and throat diameter (discussed in detail in section 2.3.1.1).

3.1.3.2.1.4 Boundary-Layer Losses

Boundary-layer analyses shall evaluate exhaust-stream momentum loss due to friction and to displacement thickness and shall predict convective heat-transfer coefficients.

To predict nozzle frictional and heat-transfer losses, the analytical techniques developed in reference 89 should be used. Therein friction, heat transfer, and boundary-layer growth are calculated for axisymmetric geometries by simultaneous solution of the integral momentum and energy equations. Analytically, nozzle boundaries should be displaced by the calculated boundary-layer thicknesses, and these displaced nozzle boundaries should be used in the detail flow analyses (sec. 3.1.3.2.1.1). Reference 92 provides examples of calculations using the methods given in reference 89 to determine boundary-layer momentum and displacement thickness; these examples may be used as guides.

Using the subscript i to indicate ideal flow in a nozzle unaffected by a boundary layer and assuming choked conditions at the throat, the difference in thrust coefficient between an "ideal-flow" motor and a "real" motor can be expressed as (ref. 143)

$$\begin{aligned} \Delta C_{F_{BL}} = & \int_0^1 \left(\frac{P}{P_o} \right)_i d \left(\frac{A}{A_t} \right) - \int_0^1 \left(\frac{P}{P_o} \right) d \left(\frac{A}{A_t} \right) \\ & + \int_0^1 \frac{(\rho u^2)_i}{P_c g_c} d \left(\frac{A}{A_t} \right) - \int_0^1 \frac{\rho u^2}{P_c g_c} d \left(\frac{A}{A_t} \right) \\ & + \int \left(\frac{A_s}{A_t} \right) \frac{\rho u^2}{2P_c g_c} C_f \cos \alpha d \left(\frac{A_s}{A_t} \right) \\ & + \int \left(\frac{A_s}{A_t} \right) \frac{(P_i - P)}{P_c} \sin \alpha d \left(\frac{A_s}{A_t} \right) \end{aligned} \quad (62)$$

where A_s is the local nozzle surface area downstream of the throat, C_f is the skin friction coefficient of the nozzle wall, and the final term treats the effect of changes in nozzle wall pressure due to effective displacement of the flow boundaries and the effects of heat transfer.

In nozzles with low expansion ratios, boundary-layer frictional loss often can be neglected. However, heat losses become relatively more important. Thus, in low-expansion nozzle applications, a simplified approach to boundary-layer and heat-transfer determination often becomes more practical. One recommended prediction technique is that of Bartz (ref. 139); convective heat-transfer coefficients predicted by this method are based on average mass flowrates. As previously pointed out, the true significance of the boundary-layer and heat losses depends on the required accuracy of the motor performance predictions.

3.1.3.2.1.5 Heat Losses

Prediction of heat losses shall be based on integration of the heat flux over the surfaces of the affected hardware for the period of motor operation.

Loss in exhaust-gas momentum due to the transfer of heat to the combustion chamber is frequently treated as an incremental loss in specific impulse. In small BEM's ($\dot{m} < 1 \text{ lb}_m/\text{sec}$) significant amounts of heat are lost to both the combustion chamber and nozzle hardware. On the other hand, in conventional full-scale motors a significant percentage of heat is lost to the nozzle primarily through convection. The magnitude of this loss is determined normally during the nozzle heat-transfer analysis using procedures recommended by Wong (ref. 32). To evaluate this loss, wall heat flux should be calculated from the relation (ref. 34)

Wall heat flux = convective heat flux + radiant heat flux

$$\dot{q} = h_c (T_{aw} - T_w) + \epsilon_r \alpha (T_c^4 - T_w^4) \quad (63)$$

where

- \dot{q} = heat flux, Btu/hr-ft²
- T_{aw} = adiabatic wall recovery temperature on the gas side of the boundary layer, °R
- T_w = wall temperature of the nozzle material, °R
- ϵ_r = particle cloud emissivity
- α = Stefan-Boltzmann constant
- T_c = combustion-chamber temperature, °R

The heat flux distribution should be integrated over the nozzle surface for the action time of the motor and the calculated thermal energy converted to an incremental specific impulse loss:

$$\Delta I_{sp} = \sqrt{\frac{2 \eta Q J}{W_p g_c}} \quad (64)$$

where

$$\begin{aligned} \eta &= 1 - (T_e/T_c) \\ T_e &= \text{exit temperature, } ^\circ\text{R} \\ Q &= \text{total heat loss, Btu} \\ W_p &= \text{propellant weight, lb}_m \end{aligned}$$

3.1.3.2.2 Simplified Analytical Prediction

Prediction of thrust coefficient shall utilize simplified analytical techniques only when the performance efficiency of the design has been demonstrated in similar applications.

Similar applications must include comparable nozzle geometry and size, propellant basic formulation and metal content, motor size, operational duration, and pressure level and nozzle-grain geometric interrelations. The following expression combines the thrust coefficient relation for one-dimensional, isentropic, idealized converging-diverging nozzle flow with the demonstrated thrust efficiency factor η_F (divergence correction factor λ included):

$$\begin{aligned} C_{F_{\text{delivered}}} = \eta_F \left\{ \sqrt{\frac{2\gamma^2}{\gamma-1} \left(\frac{2}{\gamma+1}\right)^{\frac{(\gamma+1)}{(\gamma-1)}} \left[1 - \left(\frac{P_{e'}}{P_c}\right)^{\frac{(\gamma-1)}{\gamma}} \right]} \right. \\ \left. + \left(\frac{P_{e'} - P_a}{P_c}\right) \varepsilon_{e'} \right\} \quad (65) \end{aligned}$$

All gas properties should be evaluated on throat discharge area and the point source-flow spherical exit area, not on the planar exit area (refs. 93 through 95).

This simplified prediction method is satisfactory in the analysis of propulsive systems with conventional, convergent-divergent conical nozzles. Both recommended computer programs (refs. 2 and 3) perform this computation automatically. Parameters that must be input directly or calculated indirectly include nozzle expansion ratio, half-angle, and thrust efficiency factor; ambient pressure; and exhaust gas specific heat ratio.

3.1.3.2.3 Flow Separation Effects

The prediction of nozzle flow separation and its influence on deliverable thrust coefficient shall utilize semi-empirical relationships derived from the available data.

For a nozzle in which the flow has separated from the nozzle wall, C_F should be expressed as the sum of two terms: the flow upstream of the point of flow separation, and the flow downstream of that point. For the first term, the techniques recommended in sections 3.1.3.2.1 or 3.1.3.2.2 should be used. For the second term (in the case of conical nozzles), equation (32) should be used to predict static pressure at which separation occurs. The expansion ratio ε_i (fig. 15) should then be determined from one-dimensional, isentropic, inviscid flow relationships if the simplified approach to predicting thrust coefficient is being used. If a method-of-characteristics analysis of the supersonic flow field is being made, ε_i is the expansion ratio at which P_i is reached. The thrust coefficient increment for this separated flow region should be predicted by using the empirical expression developed by Kalt and Badal (ref. 96):

$$(\Delta C_F)_s = 0.55 \left[\frac{P_i + P_{0.95}}{P_c} \right] \left[\varepsilon_{0.95} - \varepsilon_i \right] + 0.975 \frac{P_a}{P_c} \left[\varepsilon_e - \varepsilon_{0.95} \right] \quad (66)$$

where

$$\varepsilon_{0.95} - \varepsilon_i = \frac{\varepsilon_i - 1}{2.4} \quad \text{if } \varepsilon_i \leq \frac{\varepsilon_e}{1.604} + 0.377 \quad (66a)$$

$$\varepsilon_{0.95} - \varepsilon_i = \frac{\varepsilon_e - \varepsilon_i}{1.45} \quad \text{if } \varepsilon_i > \frac{\varepsilon_e}{1.604} + 0.377 \quad (66b)$$

and subscript 0.95 is the position in nozzle where static pressure equals 0.95 of the ambient pressure value.

The thrust coefficient for the total is expressed as

$$C_{F_{\text{total}}} = (C_F)_{\text{upstream of plane of separation}} + (\Delta C_F)_{\text{downstream of plane of separation}} - \left(\frac{P_a}{P_c} \right) \varepsilon_e \quad (67)$$

These semi-empirical relationships were based on a detailed review of available data. However, other relationships (ref. 1) have been successful and can be used as alternates. Little data are available on contoured nozzle separation, and the procedures and relationships recommended for conical nozzles should likewise be used with contoured designs.

In general, subscale nozzle performance tests to establish the point of separation are not warranted. However, if such tests are conducted, empirical relationships for the particular nozzle design under analysis can be developed for use in predicting full-scale motor performance.

3.2 Prediction of Motor Mass and Motor Balance Versus Time

3.2.1 Motor Mass Versus Time

Mass-time predictions shall account for the discharge of both propellant and inert products.

The computer programs in references 2 and 3 should be used to calculate propellant discharge (eq. (4)). The discharge of inert materials should be predicted separately from heat-transfer analyses of the thrust chamber made during the design of the insulation and nozzle systems. The two should then be combined with hardware mass to predict motor mass as a function of time.

3.2.2 Motor Mass and Motor Balance Versus Time

Prediction of motor center of gravity and moment of inertia shall be based on the motor station distribution of the discharged propellant and inert material.

The predictions should be based on both longitudinal and circumferential motor stations from which propellant and inert materials are discharged. If the internal ballistic program in reference 3 or a program of this type is used, the remaining propellant mass, center of gravity, and principal moments of inertia are calculated automatically. The magnitude and distribution of inerts should be predicted from the heat-transfer analyses of the thrust chamber. These propellant and inert material mass- and balance-time histories are combined with those of the hardware components to predict total motor mass- and balance-time histories.

If the internal ballistic program discussed in reference 2 or a program of this type is used, propellant mass and center-of-gravity are calculated automatically. Propellant principal moments of inertia, however, are only calculated for symmetrical grains. For nonsymmetrical geometries, these principal moments of inertia must be calculated separately for the remaining web of propellant. These histories should be combined with those of inert component material and motor hardware to predict total motor histories. Use standard mathematical techniques in calculating centers of gravity and in calculating and shifting principal moments of inertia.

3.3 Evaluation of Propellant Performance Parameters

3.3.1 Specific Impulse

The propellant specific impulse value used in motor performance predictions shall be the specific impulse that can be delivered by the motor.

The methods provided in section 3.3.1.1 should be used to account for losses and to predict I_{spd} ; the techniques of section 3.3.1.2 should be used to confirm and verify the predicted values. In the final evaluation of the motor design, the demonstrated values for I_{spd} obtained as recommended in section 3.3.1.2 provide the basis for performance predictions. The analytic techniques of section 3.3.1.1, however, are most useful in the design evaluation phase when demonstrated values may not be available; furthermore, they are fundamental to accurate scaling of the BEM values to full-scale motor values.

The chief deficiency in currently available techniques is that losses associated with combustion inefficiency and finite-rate chemical kinetics in a two-phase axisymmetrical or two-dimensional flow cannot be analyzed successfully. In terms of motor performance, most of the losses due to lag are reflected in the characteristic velocity c^* rather than in the thrust coefficient C_F . In fact, for large fractions of particles, Hoglund (ref. 42) shows that C_F increases with the magnitude of lag for certain ranges of particle size. This illustrates the fallacy involved in using c^* as a measure of combustion efficiency for particle-laden combustion products. Hoglund further notes that losses caused by particle lag may be attributed incorrectly to combustion inefficiency if c^* is regarded as a measure of combustion efficiency. The majority of the lag effects appear in c^* because most of the lag develops in the nozzle throat region originating ahead of the sonic point where the limiting mass flow is determined (fig. 17). Therefore, separate efficiency factors should be used with the expressions

$$I_{spd} = \eta_\mu I_{spd}^0 \quad (68)$$

and

$$I_{spd} = \eta_\theta c^* \eta_F C_F / g_c \quad (69)$$

where

$$\begin{aligned} \eta_\mu &= \text{motor efficiency factor} \\ \eta_\theta &= c^* \text{ efficiency factor} \\ \eta_F &= C_F \text{ efficiency factor} \end{aligned}$$

Also, the performance of the propellant should be substantiated by demonstration in small BEM's that simulate as closely as practical conditions under which the full-scale motor will operate. This demonstrated propellant performance should be scaled analytically to deliverable full-scale motor values using methods recommended in section 3.3.1.2.2.

3.3.1.1 Analytical Prediction

The analytical prediction of deliverable specific impulse shall account for losses upstream and downstream of the nozzle throat attributable to combustion inefficiency; entrance, divergence, friction, heat, and recombination losses; and two-phase flow lag.

As specific impulse is a direct function of thrust coefficient, the recommendations made for the analytical prediction of this coefficient also apply to specific impulse. The programs prepared by Kliegel et al. (refs. 48 and 51), or equivalent programs, should be used in predicting deliverable specific impulse. The composition and heats of formulation data should be obtained from JANAF standard tables (ref. 141). Relaxation rates may be obtained from reference 142. Semi-empirical drag and Nusselt number relationships as determined by Hoglund and Carlson (ref. 72) should be used in characterization of the particles. Boundary-layer and heat-transfer losses should be predicted using methods recommended in sections 3.1.3.2.1.4 and 3.1.3.2.1.5, respectively.

A program such as the one written by Zeleznik and Gordon (refs. 85 and 86) is recommended as an alternate. This program calculates one-dimensional, idealized flow in chemical equilibrium. Theoretical specific impulse values predicted by this type program are reduced by the efficiency factor η_μ to predict deliverable values. This factor is the product of the efficiencies associated with deliverable characteristic velocity and thrust coefficient as shown in equation (69). It can also be determined as the ratio of the product of the deliverable values to the product of the theoretical values, assuming idealized one-dimensional flow. These theoretical values are calculated automatically by this theoretical performance program. The deliverable thrust coefficient should be predicted by the method recommended in section 3.1.3.2, and the deliverable characteristic velocity should be determined from BEM tests. Frequently and satisfactorily the efficiency factor η_μ is taken from a set of full-scale motor data such as that depicted in figure 16.

3.3.1.2 Demonstration

The specific impulse values used in predicting motor performance shall be based on values demonstrated in ballistic evaluation motor tests.

Deliverable specific impulse values for the particular propellant should be obtained from BEM's under chamber and ambient conditions simulating those specified for full-scale motor operation. The measured values should be used in predicting the performance of the full-scale motor. If I_{spd} is adjusted to standard conditions and reported as I_{spg} ,³ the corresponding I_{spd} and motor characteristics also must be reported.

3.3.1.2.1 Specific Impulse BEM Characteristics

The characteristics of the ballistic evaluation motor used in evaluating the deliverable specific impulse of a propellant shall minimize the extent of performance scaling required.

The basic procedures used in small-motor measurement of propellant specific impulse should comply with those suggested in reference 27. Motor and propellant geometrical design characteristics should be a blend of those suggested in references 27, 45, and 112.

³See Glossary.

The design should provide a neutral pressure-time trace (within $\pm 10\%$); a sharp tailoff (burning time ≥ 0.87 action time, and tailoff pressure integral $< 5\%$ action time pressure integral); a grain port-to-throat area ratio $A_p/A_t \geq 6$; and a low length-to-diameter ratio $L/D \leq 2$, to minimize erosive-burning influence. Burning duration should be short, 2 to 10 seconds, to minimize heat loss and nozzle erosion. Nozzle throat insert material and size should be selected to minimize throat erosion and produce a chamber pressure that is within ± 10 percent of the full-scale motor operational value. The nozzle should be conical with a $15^\circ \pm 0.5$ exit cone half-angle and an expansion ratio slightly less than optimum. The latter is necessary for full-flow attachment throughout motor "equilibrium" burning. To avoid unwanted mass-flow contributions from inerts, little or no liner should be used. Specific impulse should be based on propellant charge weight. Consumed weight should be determined by pre- and post-firing motor weight measurements.

3.3.1.2.2 Specific Impulse Scaling

Analytical scaling shall account for the differences in heat loss, two-phase flow lag, nozzle geometry, the contribution of inerts, and the operational conditions that exist between the ballistic evaluation motor and the full-scale motor.

The analytical procedure outlined in figure 25 is recommended for scaling small-motor delivered specific impulse to that expected in the full-scale motor.

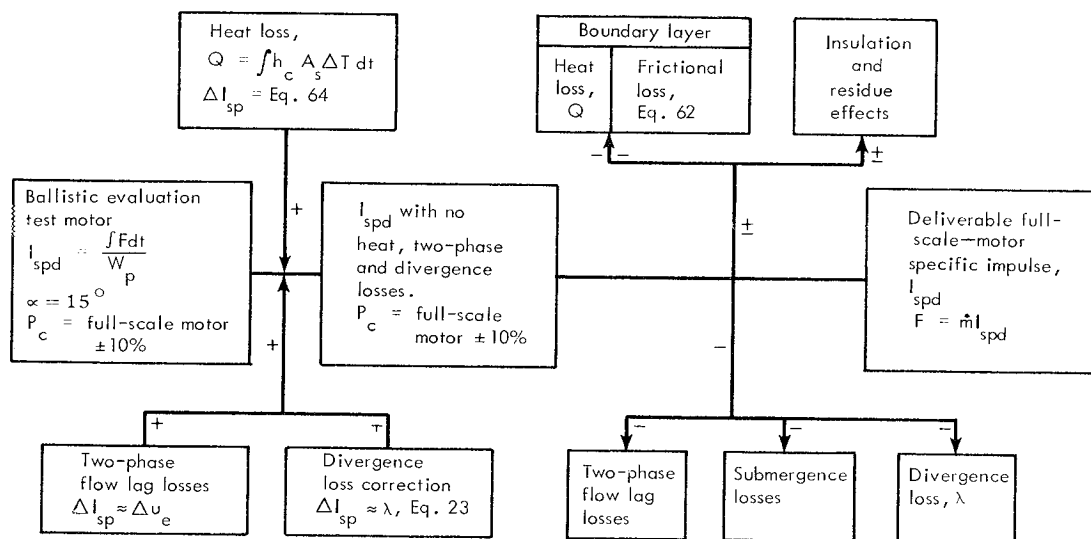


Figure 25.—Specific impulse scaling schematic

A propellant weight of about 50 pounds is recommended for the general small BEM charge. This will permit satisfactory scaling to all motor sizes. However, for

a full-scale motor of nominal design and 30 inches or less in diameter, a satisfactory scaleup can be made from BEM's with a 5- to 10-pound propellant charge. BEM's that meet these general requirements are the AFRPL BATES motor (ref. 112) and the Rohm and Haas 6C5-11.4 motor (ref. 45), respectively. The recommendations made in section 3.4 should be used as a basis for establishing the number of test motor firings.

Heat losses should be determined with a calorimeter. If measured heat losses are not available, as will be the case for the full-scale motor, losses should be predicted analytically with the methods recommended in section 3.1.3.2.1.5.

A particle size analysis of exhaust species is desirable; however, if an analysis is not permissible, use the data shown in figures 9, 10, and 11. Two-phase flow losses should be predicted with the analytical techniques and computer programs recommended in section 3.1.3.2.1.1. If the full-scale motor has a short conical nozzle and the expansion ratio is relatively low, the more simple, one-dimensional, constant-lag, gas-particle flow analysis (fig. 17) may be used (ref. 44). This type of analysis can be used typically for scaling BEM two-phase lag. In this case the two-phase lag can be evaluated at the nozzle throat by making a variable-lag analysis up to the throat, assuming that the lag will remain constant during the nozzle expansion process. Divergence loss can be calculated with the aid of equation (23) and figure 13. However, if the expansion section is long or the area ratio is high, a constant-lag solution should not be used because it does not account for the partial recovery of gas-particle dynamic and thermal equilibrium. Rather, one-dimensional gas-particle flow programs of the type described in references 47 and 48 should be used for conical nozzles, while those of the two-dimensional type described in references 49 and 50 should be used for contoured nozzles.

Combustion-chamber liner material discharged during motor burning contributes to the momentum of the exhaust primarily through addition of mass. Under certain conditions and combinations, however, some kinetic energy is added to the exhaust stream. Insulation loss can be attributed to pyrolysis and erosion; its contribution to specific impulse has been expressed by Gordon (ref. 114) as

$$(I_{spd})_g = (I_{spd})_p \left[\frac{W_p + W_L \left(\frac{T_L}{T_c} \right) - \left(\frac{W_L q}{c_p T_c} \right)}{W_p + W_L} \right]^{-1/2} \quad (70)$$

where

W_p = propellant weight, lb_m

W_L = weight of liner lost upon firing, lb_m

c_p = specific heat of combustion products, Btu/lb_m

q = heat required for pyrolysis of unit weight of liner, Btu/lb_m

T_c = combustion temperature of propellant, °R

- T_L = initial temperature of liner, °R
 $(I_{spd})_g$ = delivered specific impulse of mixed gases as expanded through nozzle, lb_f-sec/lb_m
 $(I_{spd})_p$ = delivered specific impulse of propellant, lb_f-sec/lb_m

If the heat of pyrolysis and interaction is ignored or can be neglected, the following simplified expression is obtained:

$$(I_{spd})_g = (I_{spd})_p \left(\frac{W_p}{W_p + W_L} \right)^{-1/2} \quad (71)$$

These relationships are recommended for use in approximating the contribution of inert material to motor performance.

3.3.2 Density

Values for propellant density utilized in performance predictions shall be known to a degree of accuracy commensurate with program requirements.

The density measurements should be made on small specimens of the propellant being considered for use. The liquid displacement method of determining propellant density is recommended; it provides a more reliable determination because geometry is not involved. Two weight measurements and a well-established value for specific gravity of a liquid are required. However, care must be exercised in selecting the liquid to minimize both liquid absorption by the specimen and any liquid-induced deterioration of the specimen. These sources of inaccuracy should be evaluated by conducting laboratory compatibility tests of the propellant and candidate liquid. The weight-volume method can be used confidently as an alternate if the geometry of the weighed specimen permits an accurate volume calculation.

3.3.3 Burning Rate

Burning rates used in motor performance predictions shall be based on results of experimental tests.

In motor performance predictions, linear-type burning-rate relationships should be used in steady-state analyses where equilibrium conditions prevail. These rates also should serve as the basic regression rates on which augmented rates are based. The latter rates frequently are required in ignition transient and steady-flow quasi-steady-state analyses. Linear burning rates should be determined by the method recom-

mended in section 3.3.3.1. The recommended techniques to be used in determining augmented rates are presented in section 3.3.3.2.

3.3.3.1 Linear Burning-Rate Characteristics

Prediction of full-scale-motor propellant linear burning rates shall be based on the characteristics demonstrated in small-ballistic-evaluation-motor tests.

Linear burning rates of solid propellants depend primarily on formulation, chamber pressure, and temperature of the propellant grain. To provide burning-rate data for motor performance predictions, the propellant under analysis should be tested over the ranges of pressure and temperature expected to be encountered in and by the full-scale motor (see secs. 3.3.3.1.1.1 and 3.3.3.1.1.2, respectively, for detailed recommendations). As reviewed previously, several state-of-the-art techniques have been used in the experimental determination of linear burning rate. Of these, use of the small BEM is recommended; this motor should satisfy criterion of section 3.3.3.1.1.

3.3.3.1.1 Burning-Rate BEM Characteristics

Motors used to evaluate linear burning rates shall provide burning under equilibrium pressure conditions and a neutral pressure-time trace with sharp ignition and tailoff transients.

A neutral pressure-time trace can be achieved by the use of a grain design that will produce a burning surface/web history progressive enough to account for nozzle throat erosion. The motor grain port-to-throat area and length-to-diameter ratios should be selected to eliminate erosive burning. In general, the port-to-throat area ratio should be 6 or greater and the length-to-diameter ratio less than 4 and more desirably about 2. Minimum and maximum possible values, however, are dependent on the susceptibility of the particular propellant to exhibit erosive burning tendencies, and this susceptibility is established only by tests or by experience with the formulation.

Burning rate is determined by dividing the propellant web by the burning time. Values for these parameters must be determined accurately. Webs generally are measured at an ambient temperature of about 70° F. Web thicknesses are kept small to eliminate essentially any change resulting from thermal shrinkage. The pressure-time trace should be analyzed carefully to identify propellant burn time properly. The ignition transient and tailoff regions should be of relatively short duration and readily identifiable. The start of web burning should correspond to that point on the trace where an inflection point occurs in the ignition transient phase of the motor pressure-time trace. However, examples presented in reference 45 can aid in establishing this point. Web burnout corresponds to the point of maximum rate of change of curvature in the tailoff region of the pressure-time trace as described in

detail in reference 117. If the trace is not reduced by computer or if this latter point is not clearly distinguishable, the web burnout point may be determined (as suggested in ref. 118) by the widely used tangent-bisector method.

In many instances a one-to-one correlation has been demonstrated between burning rates for the small and full-scale motors; in others, some scaling was necessary. However, no satisfactory scaling relationship for universal application has been found. Inconsistent reduction of small-motor data frequently has introduced a necessity for scaling burning rates, and failure to account fully for propellant web changes due to thermal shrinkage and ignition pressurization in full-scale motors also has made scaling necessary. Therefore, scaling of demonstrated small-motor burning rates should be based on factors established from demonstrated correlations for similar operational ranges, motor sizes, and propellant formulation.

3.3.3.1.1.1 Chamber Pressure Sensitivity

Sensitivity of burning rate to chamber pressure shall be known over the operational pressure range predicted for the full-scale motor.

The variation in linear burning rate with pressure should be determined by firing BEM's over the complete range of chamber pressure expected for the full-scale motor. Varying the nozzle throat area or the grain burning surface provides this variation at a particular grain temperature. The coefficient of pressure a and the pressure exponent n of the linear burning-rate equation should be calculated from these test results.

The number of tests required depends on whether $\log r$ vs. $\log P$ is essentially linear over the pressure range of interest or whether the propellant is of the plateau or mesa type. Additional factors are the desired probability and confidence levels, program economics, and often scheduling. Over a pressure range in which the burning rate coefficient a and exponent n remain constant, a minimum of seven motors should be fired. Two of the seven motors should be fired at the lowest and two at the highest expected pressure levels, and the other three should be fired at the nominal pressure level. An extremely large pressure range, as might be encountered in boost-sustain applications, would require additional BEM tests.

3.3.3.1.1.2 Temperature Sensitivity

Sensitivity of burning rate to propellant temperature shall be known for the operational temperature range specified for the full-scale motor.

Motors used to evaluate linear burning rates should be conditioned at each of the temperature levels of interest and then fired. Data from these tests should be displayed in a $\log r$ vs. $\log P$ plot for each test temperature and specified propellant

type as illustrated in figures 20 and 21. With the data plotted in this form, coefficients that describe the propellant burning rate as a function of temperature

and pressure can be determined. The four most commonly used coefficients, π_K , σ_P , σ_K , and $\pi_{P/T}$, were defined in equations (12) through (15), respectively.

Coefficients π_K and σ_P are of primary importance in performance predictions. In motors where pressure drop in the chamber is not large, π_K should be used to estimate variation of operating pressure with temperature. However, for motors with significant flow velocity in the grain port, the burning-rate pressure characteristics of the propellant can best be defined using σ_P . These data are then used at the temperature of interest to calculate pressure and thrust as previously described.

The exact number of tests required to determine these coefficients is dependent on propellant characteristics, desired probability and confidence levels, and economics involved. For a propellant with characteristics as shown in figure 20 and for the typical case of three temperature levels, five tests at each temperature extreme and seven at the nominal temperature are the minimum number of tests from which both temperature coefficients and the pressure coefficient a and exponent n can confidently be determined. Thus, at least 17 tests are required to identify the sensitivity of linear burning rate to both pressure and temperature. This minimum is further restricted to those tests that provide good data with limited scatter and in which the operational pressure range is not extremely large. Additional tests would be required for boost-sustain designs.

3.3.3.2 Augmentation of Linear Burning Rates

Prediction of augmentation of propellant burning due to erosive burning, pressurization, or vehicle acceleration shall use empirical relationships based on demonstrated correlations.

Proportionality constants in the semi-empirical relationships used in predicting full-scale motor augmented rates should be based on correlation with small-motor demonstrated rates. The recommended relationships for erosive burning and transient-pressure effects are those of Lenoir and Robillard (eq. (50)) and Von Elbe (eq. (40)), respectively. As alternates for erosive burning, Kreidler's (eq. (51)) or Saderholm's (eq. (52)) empirical expressions are recommended (see also sec. 3.1.2.1.2). Instrumentation and small-evaluation-motor design characteristics used by Lawrence et al. (ref. 144) are recommended for the erosive-burning study although slab tests can be used advantageously (ref. 136). Erosive-burning rates demonstrated in these small motor tests should be scaled to predict full-scale motor rates. The ratio of the hydraulic radii should be used to adjust the augmentation term δ in equation (18):

$$\delta_{fsm} = \delta_{bem} (R_{h_{bem}}/R_{h_{fsm}})^{0.2} \quad (72)$$

where

$$R_h = \text{hydraulic radius} = 2 \times \left(\frac{\text{port cross-sectional area}}{\text{port perimeter}} \right), \text{ in.}$$

fsm = full-scale motor

bem = ballistic evaluation motor

These tests, of course, are not necessary if the pressurization and erosive-burning constant have been determined for the propellant in a previous full-scale motor design with characteristics closely related to those of the motor under analysis.

Proven empirical relationships and internal ballistic programs for predicting burning-rate augmentation due to vehicle angular acceleration are not current state-of-the-art practice. As pointed out in section 2.3.3.2.3, spin-induced augmentation is a function of acceleration magnitude, of orientation of the acceleration vector relative to the burning surface, and of propellant formulation. Thus, to determine spin-induced burning rate adequately, the propellant charge design used in the small BEM must be a scaled replica of the full-scale charge design. If propellant slabs are used, employ the techniques developed by Northam et al. (ref. 145). From these data, the δ from equation (18) can relate burning-rate augmentation to acceleration level and direction as described in reference 21. For motor designs in which bondline burning-rate augmentation can have a significant influence on ballistic performance, particularly end-burning grains, subscale motors duplicating exact liner design and processing and propellant formulation should be prepared and fired. Thus the burning rate used in calculating full-scale motor internal ballistics should combine the various augmenting effects, i.e.,

$$r_b = r(1 + \delta_{\text{erosive burning}} + \delta_{\text{pressurization}} + \delta_{\text{acceleration}} + \delta_{\text{bondline}}) \quad (73)$$

3.4 Prediction of Performance Variability

3.4.1 Variables

Variables shall include both the variations in propellant ballistic characteristics and the dimensional tolerances on the grain and inert components.

Propellant ballistic parameter variations considered should be those demonstrated in small motor tests and substantiated, if possible, by variations determined from statistical analyses of similar full-scale motors. Parameters for which variations should be determined include burning rate, pressure exponent, temperature sensitivity, specific impulse, and characteristic velocity. Propellant density variations and thermal shrinkage should also be established.

The mean value, standard deviation, and tolerance limits for these experimentally determined propellant characteristics should be established by assuming normal distributions. Calculations should be as shown.

$$\text{Mean value, } \bar{X} = \frac{\sum X_i}{N} \quad (74)$$

where

X_i = experimentally determined values that make up the sample
 N = the number of data points in the sample

The standard deviation is estimated by

$$s = \sqrt{\frac{N \sum X_i^2 - (\sum X_i)^2}{N(N-1)}} \quad (75)$$

Variation limits are determined as the bounds which, with a certain probability, will contain at least a certain percent of the data population and are expressed by the relationship

$$v = \bar{X} \pm K_s \quad (76)$$

where

v = parameter variation on which limits are being established
 K = variation factor, considering probability desired

Variation factors used in this expression can be found in statistical tables for normal distributions as presented in reference 146. If the data sampling is small ($N < 30$), the small-sampling theory (Students t distribution) should be assumed. The number of ballistic evaluation firings should be based on an analysis that assumes a normal distribution of the data and considers the combined effects of (1) specified performance limits; (2) required reliability and confidence level; (3) test uncertainties; (4) test model—size, type, and degree of similarity; and (5) program economics. The initial two factors are established by contract requirements. Instrumentation uncertainties are generally well-established factors for the test equipment being used but vary among facilities and types of instrumentation. Statistical tables for nominal distribution will indicate the number of tests required for certain reliability and confidence levels. The extent to which the BEM's simulate conditions expected with the full-scale motor should be assessed by considering past experience with similar formulations and previous correlations with demonstrated motor performance. To determine an allowable number of tests, this information must be combined with performance limits and levels contractually specified for the total motor, available funds, and test uncertainties.

Detailed drawings of the motor case, grain assembly, and tooling should be used to determine dimensional tolerances on grain length, web, burning surface, weight, and port area. Variations in the thermal shrinkage of the propellant should be established in laboratory tests and used in predicting the changes in grain web, burning surface, and propellant density with motor conditioning temperature and ignition pressurization. These thermally induced changes in burning surface are especially critical in designs with high ignition-pressure spikes and should be predicted from analyses made for the evaluation of the structural integrity of the grain. Becker's and Brisbane's (ref. 147) computer programs are typical of those that will provide this information. Because thrust and total impulse are dependent on density, variations in this parameter should be within the limits allowed by the process specification or determined from laboratory-measured data (sec. 3.3.2).

Dimensional tolerances on linear thickness, motor case inside diameter, and nozzle geometry should be determined from detailed drawings. Case and liner tolerances can influence propellant weight and motor total impulse. Burning duration is subject to these tolerances as influenced by web thickness. Nozzle tolerances associated with throat area, exit area, contour half-angle, and axial misalignment should be combined so that the possible variation in thrust coefficient may be predicted. Throat area variations also should be examined for the effect on chamber pressure and thus on burning rate.

3.4.2 Prediction of Variations

Prediction of variability for a performance parameter shall utilize a mathematical combination of propellant variations and grain and inert component tolerances.

To make a prediction of variability, all variables that affect a single performance parameter must be combined. The mathematical technique recommended is to take the square root of the sum of the squares of tolerances and variations involved. This technique is applicable when taking the sum or difference of independent errors. A more general form, applicable to independent variables related by various powers, products, or quotients, is presented in references 148 and 149. The general rule for propagation of error states that, if $f = f(x, y, z)$, then

$$\sigma_f^2 = \left(\frac{\partial f}{\partial x} \right)^2 \sigma_x^2 + \left(\frac{\partial f}{\partial y} \right)^2 \sigma_y^2 + \left(\frac{\partial f}{\partial z} \right)^2 \sigma_z^2 \quad (77)$$

or the variance of f is equal to the sum of the partial derivatives of f with respect to each variable times the variance of the variable. For the special case wherein $f(x, y, z)$ is a sum or a difference, then $(\partial f/\partial x)^2 = (\partial f/\partial y)^2 = (\partial f/\partial z)^2 = 1$, and σ_f^2 reduces to the sum of the variances.

However, if the maximum or minimum possible performance limit for a particular parameter must be predicted with a high degree of confidence, the algebraic addition of geometric tolerances and parameter variations should be used. In this technique, the maximum or minimum tolerances and variations are combined in the manner that will predict the greatest total variation in the value of the particular performance parameter under evaluation. Variations may be evaluated with respect to minimum or maximum (whichever is the limit of interest) performance variability.

REFERENCES

1. Threewit, T. R.; Rossini, R. A.; and Uecker, R. L.: The Integrated Design Computer Program and the ACP-1103 Interior Ballistics Computer Program. STM-180, Aerojet-General Corp., Dec. 1964 (AD 466965).
2. Anon.: Solid Propellant Rocket Motor Internal Ballistics Computer Programs. Program Manual, RK-TR-67-7, The Boeing Co., Sept. 1967 (AD 822349).
3. Anon.: Grain Design and Internal Ballistics Evaluation Program (IBM 7094 FORTRAN IV), Program 64101. Bacchus Works, Hercules Powder Co., July 1967 (AD 818321).
4. Anon.: A Research Study To Advance the State-of-the-Art of Solid Propellant Grain Design. E70-62, Thiokol Chemical Corp., May 1962 (N62-14025).
5. Streeter, F. W.; and Friedman, I. H.: The Design of High Mass Flow Solid Propellant Rocket Motors (U). CPIA no. 18A, Bulletin of the Interagency Solid Propulsion Meeting, vol. IV, July 1963 (AD 346945). (Confidential)
6. Barrere, M.; Jaumotte, A.; Fraeijs de Veubeke, B.; and Vandekerckhove, J.: Rocket Propulsion. D. Van Nostrand Co., 1960, pp. 237-239.
7. Liepmann, H. W.; and Roshko, A.: Elements of Gas Dynamics. GALCIT Aeronautical Series, Third ed., John Wiley and Sons, Inc., Feb. 1960, pp. 39-61.
8. Anon.: Solid Rocket Motor Igniters. Space Vehicle Design Criteria Monograph, NASA SP-8051, 1971.
9. Price, E. W.; Bradley, H. H.; DeHORITY, G. L.; and Iliricu, M. M.: Theory of Ignition of Solid Propellant. NOTS TP 3954, Naval Ordnance Test Station, China Lake, Calif., Mar. 1966.
10. Price, E. W.: Status of Solid Rocket Combustion Instability Research. NOTS TP 4275, Naval Ordnance Test Station, China Lake, Calif., Feb. 1967.
11. Hart, R. W.; and McClure, F. T.: Theory of Acoustic Instability in Solid Rocket Combustion. Tenth Symposium (International) on Combustion, Combustion Inst. (Pittsburgh), 1965, pp. 1045-1065.
12. Bird, J. F.; McClure, F. T.; and Hart, R. W.: Acoustic Instability in the Transverse Modes of Solid Propellants. Proceedings of the Twelfth International Astronautical Congress, Academic Press, 1963, pp. 459-473.
13. Coates, R. R.; and Horton, M. D.: Design Considerations for Combustion Stability. AIAA Paper 68-532, ICRPG/AIAA Third Solid Propulsion Conference (Atlantic City), June 4-6, 1968.
14. Trubridge, G.: Tentative Prediction Criteria for Acoustic Combustion Instability in Solid Propellant Rocket Motors. Third ICRPG Combustion Conference (Cocoa Beach, Fla.), Oct. 17-21, 1966, CPIA no. 138, vol. 1, Feb. 1967.
15. Zucrow, M. J.; Osborn, J. R.; and Murphy, J. M.: An Experimental Investigation of the Erosive Burning Characteristics of a Non-Homogeneous Solid Propellant. AIAA Preprint 64-107, Solid Propellant Rocket Conference (Palo Alto, Calif.), Jan. 29-31, 1964.

16. Kreidler, J. W.: Erosive Burning: New Experimental Techniques and Methods of Analysis. AIAA Preprint 64-155, AIAA Solid Propellant Rocket Conference (Palo Alto, Calif.), Jan. 29-31, 1964 (A64-13075).
17. Murphy, J. M.: Technical Memorandum on the Current Status of Erosive Burning in Solid Propellant Rocket Motors (U). Rep. TM-62-6, Jet Propulsion Center, Purdue Univ., Aug. 1962 (X62-11543). (Confidential)
18. Zucrow, M. J.; Osborn, J. R.; Murphy, J. M.; and Kershner, S. D.: Investigation of Velocity Upon Burning Rate of Solid Propellants (U). Rep. F-63-3, JPC 352, Jet Propulsion Center, Purdue Univ., Dec. 1963 (AD 346175). (Confidential)
19. Anon.: Symposium—The Behavior of Propellants Under Acceleration Fields (U). NOTS TP 3770, Naval Ordnance Test Station, China Lake, Calif., June 1965 (AD 363903). (Confidential)
20. Lucy, M. H.: Spin Acceleration Effects on Some Full-Scale Solid Rockets. J. Spacecraft Rockets, vol. 5, no. 2, Feb. 1968, pp. 179-185.
21. Northam, G. B.; and Lucy, M. H.: On the Effects of Acceleration Upon Solid Rocket Performance. AIAA Paper 68-530, Third ICRPG/AIAA Solid Propulsion Conference (Atlantic City), June 4-6, 1968 (A68-32437).
22. Sturm, E. J.; and Reichenback, R. E.: An Experimental Study of the Burning Rates of Aluminized Composite Solid Propellants in Accelerating Fields. AIAA Paper 68-529, Third ICRPG/AIAA Solid Propulsion Conference (Atlantic City), June 4-6, 1968 (A68-32436).
23. Manda, L. J.: Compilation of Rocket Spin Data. Vol. II: Literature Survey, Final Report. NASA CR-66641, 1968.
24. Norton, D. J.; Farquhar, B. W.; and Hoffman, J. D.: Analytical Studies of the Interior Ballistics of Spinning Rocket Motors—A Literature Survey. TM 67-1, JPC 431, Jet Propulsion Center, Purdue Univ., Jan. 1967 (AD 814933).
25. Sutton, G. P.: Rocket Propulsion Elements. John Wiley & Sons, Inc., 1964, pp. 37-83.
26. Anon.: Weapon System 133-A Minuteman Stage III, Quarterly Progress Rep. MCS-51 (U). Chemical Propulsion Div., Bacchus Works, Hercules Powder Co., June 1960 (AD 319693). (Confidential)
27. Anon.: Recommended Procedure for the Measurement of Specific Impulse of Solid Propellants. ICRPG Solid Propellant Rocket Static Test Working Group, CPIA Publ. 174, Aug. 1968.
28. Anon.: Thiokol 260-SL Subscale Nozzle Verification Program. NASA CR-54869, 1966.
29. Anon.: Annular Nozzle Program (U). Rep. R-4313-2, Rocketdyne, Solid Rocket Div., July 1967 (AD 363314). (Confidential)

30. Smallwood, W. L.; et al.: Beryllium Erosion Corrosion Investigation for Solid Rocket Nozzles (U). Rep. AFRPL-TR-67-82, Air Force Rocket Propulsion Lab., Edwards Air Force Base, June 1967 (AD 382136).
31. Desmon, L. G.; Hoffman, P. D.; Chao, G. T. Y.; Lesslie, J. C.; and Mancus, H. V.: Heat Transfer in Nozzle Systems (U). Final Rep. ABL/ARPA/X-143, Allegany Ballistics Lab., Hercules Powder Co., June 1965 (AD 364549). (Confidential)
32. Wong, E. Y.: Solid Rocket Nozzle Design Summary. AIAA Preprint 68-655, AIAA Fourth Propulsion Joint Specialist Conference (Cleveland), June 1968 (A68-33838).
33. Kordig, J. W.; and Fuller, G. H.: Correlation of Nozzle Submergence Losses in Solid Rocket Motors. AIAA J., vol. 5, no. 1, Jan. 1967, pp. 175-177.
34. Browning, S. C.; et al.: Structural and Thermal Analysis Report, Poseidon First Stage. Vol. II: Nozzle Analysis (U). SE025-A2A00HTJ, Chemical Propulsion Div., Bacchus Works, Hercules Powder Co., Apr. 1967. (Confidential)
35. Hagewood, J. R.: Convergent-Divergent Nozzle Contour Optimization Techniques. BOE-D5-13300, The Boeing Co., Mar. 1967 (AD 812244L).
36. Farley, J. M.; and Campbell, C. E.: Performance of Several Method-of-Characteristics Exhaust Nozzles. NASA TN D-293, 1960.
37. Rao, G. V. R.: Optimum Thrust Performance of Contoured Rocket Nozzles. LPIA—First Meeting JANAF Liquid Propellant Group, vol. I, Johns Hopkins Univ., Nov. 1959 (AD 319657).
38. Kliegel, J. R.: Nonequilibrium Phenomena of Two-Phase Nozzle Flows (U). AFRPL-TR-67-223, vol. 1, Air Force Rocket Propulsion Laboratory Two-Phase Flow Conference (San Bernardino, Calif.), Mar. 1967 (AD 387746). (Confidential)
39. Crowe, C. T.; et al.: High-Performance Nozzles for Solid-Propellant Rocket Motors (U). UTC 2025-FR, United Technology Center, Feb. 1967 (X65-14273). (Confidential)
40. Brown, B.: A Review of Multiphase Flow Through Converging-Diverging Rocket Nozzles. CPIA Publ. 44, Proceedings of the First Meeting, CPIA Working Group on Thermochemistry (Silver Spring, Md.), Feb. 1964 (AD 359497).
41. Delaney, L. J.; Hoglund, R. F.; and Smith, P. W., eds.: Proceedings of the Air Force Rocket Propulsion Laboratory Two-Phase Flow Conference (U). AFRPL-TR-67-223, vol. I (X68-16231), vol. II (X68-16247), Norton Air Force Base (San Bernardino, Calif.), Mar. 1967. (Confidential)
42. Hoglund, R. F.: Recent Advances In Gas-Particle Nozzle Flows. ARS J., vol. 32, May 1962, pp. 662-671.
43. Caswell, V. D.: Two-Phase Nozzle Flow: An Annotated Bibliography (U). Rep. L567-19, Lockheed Missiles and Space Co., June 1967 (AD 817602L). (Confidential)

44. Kliegel, J. R.: One Dimensional Flow of a Gas-Particle System. IAS Preprint 60-5, Inst. Aeron. Sciences, Jan. 1961.
45. Anon.: Ballistic Evaluation of Propellants in Micro-Motors. Rep. S-49, Redstone Arsenal Research Div., Rohm and Haas Co., Oct. 1964 (N65-13293).
46. Glauz, R. D.: Combined Subsonic-Supersonic Gas-Particle Flow. Preprint 1717-61, American Rocket Society Propellants, Combustion, and Liquid Rockets Conference (Palm Beach, Fla.), Apr. 1961.
47. Anon.: Dynamics of Two-Phase Flow in Rocket Nozzles. Final Tech. Rep. UTC 2102-FR, United Technology Center, Div. of United Aircraft Corp., Sept. 1965 (AD 471996).
48. Kliegel, J. R.; et al.: One-Dimensional Two-Phase Reacting Gas Non-Equilibrium Performance Program. Vol. I: Engineering and Programming Description. Rep. MSC-11780, TRW Systems, Aug. 1967.
49. Hoffman, J. D.: Analysis of the Flow of Gas-Particle Mixtures in Two-Dimensional and Axisymmetric Nozzles. Tech. Note BSD-TDR-62-144, Aerojet-General Corp., Dec. 1962 (AD 294956).
50. Kliegel, J. R.; and Nickerson, G. R.: Flow of Gas-Particle Mixtures in Axially Symmetric Nozzles. Detonation and Two-Phase Flow, S. S. Penner and F. A. Williams, eds., Academic Press, Inc., 1962, pp. 173-194.
51. Kliegel, J. R.; et al.: Axisymmetric Two-Phase Perfect Gas Performance Program. Vol. I: Engineering and Programming Description. Rep. MSC-11774, TRW Systems, Apr. 1967.
52. Anon.: Performance Evaluation Methods for Liquid Propellant Rocket Thrust Chambers. CPIA Publ. 132, ICRPWG on Performance Standardization, Nov. 1966 (X67-10715).
53. Pai, S.: Introduction to the Theory of Compressible Flow. D. Van Nostrand Co., 1959, pp. 114-131.
54. Oswatitsch, K.; and Rothstein, W.: Flow Pattern in a Converging-Diverging Nozzle. NACA TM-1215, 1949.
55. Sauer, R.: General Characteristics of the Flow Through Nozzles at Near Critical Speeds. NACA TM-1147, 1947.
56. Hall, I. M.: Transonic Flow in Two-Dimensional and Axially-Symmetric Nozzles. Quart. J. Mech. and Appl. Math., vol. XV, pt. 4, 1962, pp. 487-508.
57. Hopkins, D. F.; and Hill, D. E.: Effect of Small Radius of Curvature on Transonic Flow in Axisymmetric Nozzles. AIAA J., vol. 4, no. 8, Aug. 1966, pp. 1337-1343.
58. Kliegel, J. R.: Gas Particle Nozzle Flows. Ninth Symposium on Combustion, Academic Press, Inc. (New York and London), 1963, pp. 811-826.

59. Shapiro, A. H.: The Dynamics and Thermodynamics of Compressible Fluid Flows. Vols. I and II, Ronald Press, 1953, pp. 595-609.
60. Dillaway, R. B.: A Philosophy for Improved Rocket Nozzle Design. Jet Propulsion, vol. 27, no. 10, Oct. 1957, pp. 1088-1093.
61. Courtney, W. G.: Review of Particle Size Determination Techniques (U). AFRPL-TR-67-223, vol. I, Air Force Rocket Propulsion Laboratory Two-Phase Flow Conference, Norton Air Force Base (San Bernardino, Calif.), Mar. 1967 (AD 387746). (Confidential)
62. Brown, B.: Oxide Particles in Solid Rocket Exhausts. AFRPL-TR-67-223, vol. I, Air Force Rocket Propulsion Laboratory Two-Phase Flow Conference, Norton Air Force Base (San Bernardino, Calif.), Mar. 1967 (AD 387746). (Confidential)
63. Crowe, C. T.; and Willoughby, P. G.: A Study of Particle Growth in a Rocket Nozzle. AIAA J., vol. 5, no. 7, July 1967, pp. 1300-1304.
64. Brown, B.; and McAarty, K. P.: Particle Size of Condensed Oxide From Combustion of Metallized Solid Propellant. Proceedings of the Eighth International Combustion Symposium, Williams and Wilkins, 1962, p. 814.
65. Cheung, H.; and Cohen, N. S.: Performance of Solid Propellants Containing Metal Additives. AIAA J., vol. 3, no. 2, Feb. 1965, pp. 250-257.
66. Crowe, C. T.; et al.: Investigation of Particle Growth and Ballistic Effects on Solid-Propellant Rockets. UTC 2128-FR, United Technology Center, June 1966 (AD 486262).
67. Davis, L. J.: High Energy Solid Propellant Combustion Efficiency Investigation (U). Final Tech. Rep. AFRPL-TR-67-23 (Contract AF 04(611)-10814), Aug. 1966 (AD 380265). (Confidential)
68. Dobbins, R. A.: Particle Size of Aluminum Oxide Produced by a Small Rocket Motor, NASA CR-71208, Nov. 1964 (N66-19627).
69. Sehgal, R.: An Experimental Investigation of a Gas-Particle System. Tech. Rep. 32-238, Jet Propulsion Laboratory, California Institute of Technology, Pasadena, Calif., Mar. 1962 (N62-11504).
70. Cheung, H.; and Cohen, N. S.: On the Performance of Solid Propellants Containing Metal Additives. AIAA Preprint 64-116, Solid Propellant Rocket Conference (Palo Alto, Calif.), Jan. 1964 (A64-13046).
71. Smith, P.; Delaney, L. J.; and Radke, H. H.: Summary Results of Particle Size Measurements. AFRPL-TR-67-223, vol. I, Air Force Rocket Propulsion Laboratory Two-Phase Flow Conference, Norton Air Force Base (San Bernardino, Calif.), Mar. 1967 (AD 387746).
72. Carlson, D. J.; and Hoglund, R. F.: Particle Drag and Heat Transfer in Rocket Nozzles, AIAA J., vol. 2, no. 11, Nov. 1964, pp. 1980-1984.

73. Schlichting, H.: Boundary Layer Theory. McGraw-Hill, Inc., Mar. 1958, pp. 97-98.
74. Bolt, J. A.; and Wolf, L. W.: Drag Coefficient for Burning Kerosene Drops. Project 2253:3-6-P, Engineering Research Institute, Univ. of Mich., 1954.
75. Ingebo, R. D.: Drag Coefficient for Droplets and Solids Sphere in Clouds Accelerating in Air Streams. NACA TN-3762, 1956.
76. Torobin, L. B.; and Gauvin, W. H.: The Drag Coefficient of Single Spheres Moving in Steady and Accelerated Motion in a Turbulent Fluid. TR-193, Pulp and Paper Research Institute of Canada, Aug. 1960.
77. Hanson, A. R.: Effect of Relative Velocity on the Evaporation of a Liquid Fuel Spray. Ph.D. Thesis, Univ. of Mich., 1951.
78. Rabin, E.; Schallenmuller, A. R.; and Lawhead, R. B.: Displacement and Shattering of Propellant Droplets—Final Summary Report. R-2431, AFOSR-TR-60-75, Rocketdyne, 1960 (N-86368).
79. Rudinger, G.: Particle Drag Coefficient in Gas-Particle Flows (U). AFRPL-TR-67-223, vol. I, Air Force Rocket Propulsion Laboratory Two-Phase Flow Conference, Norton Air Force Base (San Bernardino, Calif.), Mar. 1967 (AD 387746). (Confidential)
80. Selberg, B. P.: Shock Tube Determination of the Drag Coefficient of Small Spherical Particles (U). AFRPL-TR-67-223, vol. II, Air Force Rocket Propulsion Laboratory Two-Phase Flow Conference, Norton Air Force Base (San Bernardino, Calif.), Mar. 1967 (AD 387746). (Confidential)
81. Crowe, C. T.; et al.: Measurement of Particle Drag Coefficients in Flow Regimes Encountered by Particles in a Rocket Nozzle. UTC 2296-FR, United Technology Center, Mar. 1969.
82. McAdams, W.: Heat Transmission. Third ed., McGraw-Hill, Inc., 1954, pp. 265-266.
83. Emmons, H. W.: Fundamentals of Gas Dynamics, High Speed Aerodynamics and Jet Propulsion. Vol. 3, Princeton University Press, 1958, p. 725.
84. Wiederkehr, R. R. V.: A General Method for Calculating the Specific Impulse of Propellant Systems. AR-1S-60, The Dow Chemical Co., June 1960 (N-84819).
85. Zeleznik, F. J.; and Gordon, S.: A General IBM 704 or 7090 Computer Program for Computation of Chemical Equilibrium Compositions, Rocket Performance, and Chapman-Jouguet Detonations. NASA TN D-1454, 1962.
86. Zeleznik, F. J.; and Gordon, S.: A General IBM 704 and 7090 Computer Program for Computation of Chemical Equilibrium Compositions, Rocket Performance, and Chapman-Jouguet Detonations. NASA TN D-1737, suppl. 1, 1963.
87. Bray, K. N. C.; and Appleton, J. P.: Atomic Recombination in Nozzles, Methods of Analysis for Flows With Complicated Chemistry. Department of Aeronautics and Astronautics, Univ. of Southampton, England, Apr. 1961.

88. Unger, E. W.: Heat Transfer to a Solid Propellant Rocket Motor Nozzle. ARS Preprint 2333-62 (IAA Abstract 62-10244), Jan. 1962.
89. Elliott, D. G.; Bartz, D. R.; and Silver, S.: Calculation of Turbulent Boundary Layer Growth and Heat Transfer in Axisymmetric Nozzles. JPL Tech. Rep. 32-387, Jet Propulsion Laboratory, Feb. 1963 (N63-14465).
90. Anon.: Analytical and Experimental Investigations of High Expansion Area Ratio Nozzles (U). RPL-TDR-64-3, vol. 1, Rocketdyne Div., North American Aviation, Inc., Dec. 1964 (AD 356121). (Confidential)
91. Hill, P. G.; and Peterson, C. R.: Mechanics and Thermodynamics of Propulsion. Addison-Wesley Publishing Company, Inc., 1965, pp. 353-424.
92. Anon.: ICRPG Liquid Propellant Thrust Chamber Performance Evaluation Manual. CPIA Publ. 178, Performance Standardization Working Group, Chemical Propulsion Information Agency, Sept. 1968.
93. Malina, F. J.: Characteristics of the Rocket Motor Based on the Theory of Perfect Gases. J. Franklin Inst., vol. 230, 1940, pp. 433-454.
94. Landsbaum, E. M.: Thrust of a Conical Nozzle. ARS J., vol. 29, no. 3, Mar. 1959, pp. 212-213.
95. Rao, G. V. R.: Evaluation of a Conical Nozzle Thrust Coefficient. ARS J., vol. 29, no. 8, Aug. 1959, pp. 606-607.
96. Kalt, S.; and Badal, D. L.: Conical Rocket Nozzle Performance Under Flow-Separated Conditions. J. Spacecraft and Rockets, vol. 2, no. 3, May-June 1965, pp. 447-449.
97. Garrett, J. W.; Simmons, M.; and Gobbell, W. C.: Exit Nozzle Flow Separation As Influenced By Nozzle Geometry, Fuel-Oxidizer Ratio, and Pressure Level. AEDC-TR-67-122, Arnold Engineering Development Center, Arnold Air Force Station, July 1967 (AD 816650).
98. Arena, M.; and Spiegler, E.: Separated Flow in Overexpanded Nozzles at Low Pressure Ratios. Bulletin of Research Council of Israel, Section C, Technology, 11C, Apr. 1962, pp. 45-55.
99. Altman, D.; Carter, J. M.; Penner, S. S.; and Summerfield, J.: Liquid-Propellant Rockets. Princeton Aeronautical Paperbacks, Princeton University Press, 1960.
100. Bloomer, H. E.; Antl, R. J.; and Renas, P. E.: Experimental Study of Effects of Geometric Variables on Performance of Conical Rocket-Engine Exhaust Nozzles. NASA TN D-846, 1961.
101. Roschke, F. J.; and Massier, P. F.: Flow Separation in a Contour Nozzle. ARS J., vol. 32, no. 10, Oct. 1962, pp. 1612-1613.
102. Campbell, C. E.; and Farley, J. M.: Performance of Several Conical Convergent-Divergent Rocket-Type Exhaust Nozzles. NASA TN D-467, 1960.

103. Witney, C. E.; Owens, T. F.; Paskind, J.; and Rubin, M. B.: Scout Motor Performance Analysis and Prediction Study (PAPS). NASA CR-336, 1965.
104. Hoffman, J. D.: An Analysis of the Effects of Gas-Particle Mixtures on the Performance of Rocket Nozzles. TM-63-1, Jet Propulsion Center, Purdue Univ., Jan. 1963 (N63-17595).
105. Crowe, C.; et al.: Effect of Nozzle Pressure Level and Scale on Performance of Solid-Propellant Rocket Motors. Final Rep. UTC 2094-FR, United Technology Center, Apr. 1965 (X65-16776).
106. Hoffman, J. D.; and Lorenc, S. A.: A Parametric Study of Gas-Particle Flows in Conical Nozzles. AIAA J., vol. 3, no. 1, Jan. 1965, pp. 103-106.
107. Lowrey, R. M.; and Brown, L. M.: Ballistic Evaluation of Solid Propellant (U). SPIA, Bulletin of the 17th Meeting, JANAF-ARPA-NASA Solid Propellant Group, May 1961 (N-60773). (Confidential)
108. Peterson, J. A.: The Selection of the Optimum Solid Propellant. Paper presented at Fifty-Third National Meeting of American Institute of Chemical Engineers (New York), May 1964.
109. Collins, R. G.: The AFRPL Ballistic Test and Evaluation System (BATES Program) (U). AFRPL-TR-65-7, Air Force Rocket Propulsion Laboratory, Edwards Air Force Base, May 1965 (AD 366289). (Confidential)
110. Warren, F. A.: Evaluation of Solid Propellant Properties. Part II: A Critical Examination of Current Methods (U). R-RS-289, Southwest Research Institute, Jan. 1959 (N-71399). (Confidential)
111. Moody, H. L.; and Price, F. C.: The Prediction of Nozzle Material Performance for NASA's 260 SL-3 Motor. AIAA Paper 68-504, ICRPG/AIAA Third Solid Propulsion Conference (Atlantic City), June 1968 (A68-32416).
112. Gale, H. W.: Development and Evaluation of the USAF Ballistic Test Evaluation System for Solid Rocket Propellants. SSD-TDR-62-45, Air Force Space System Division, Edwards Air Force Base, Apr. 1962 (AD 276424).
113. Smith, P. W.; Stetz, G. A.; and Delaney, L. J.: Impulse Scaling Prediction (U). AFRPL-TR-66-297, Air Force Rocket Propulsion Laboratory, Edwards Air Force Base, Nov. 1966 (AD 378211). (Confidential)
114. Gordon, L. J.: Ballistic Effect of Pyrolyzed Liner in Solid Propellant Motor Firings. ARS J., vol. 30, no. 5, May 1960, pp. 502-503.
115. Herty, C. H.; and Ratliff, O. D.: Prediction of Ballistic Performance of Solid Propellant Rockets From Strand and Small-Scale Motor Tests. Publ. SPS-NDT/1A, JANAF Symposia on Scale and Nondestructive Testing, Jan. 1960 (N-64740).
116. Witcraft, G. M.; and Liebman, M. E.: Correlation of Small Scale and Full Scale Rocket Motor Burning Rates. Publ. SPS-NDT/1A, JANAF Symposia on Scale and Nondestructive Testing, Jan. 1960 (N-64740).

117. Jessup, H. A.; and VanWie, H. B.: Proposed Technique for Determination of End Pressure. CPIA Publ. 24, CPIA Working Group on Static Testing, Sept. 1963 (AD 345567).
118. Anon.: Solid Propellant Nomenclature Guide. CPIA Publ. 80, Chemical Propulsion Information Agency, May 1965 (AD 465058).
119. Cooke, E. M. G.; Hodge, D. L.; and Pape, R.: Measurement of Burning Rate of Rocket Propellants by the 5-inch Vented Vessel (U). Tech Memo No. 4/M/56, Ministry of Supply, Explosives Research and Development Establishment, Feb. 1956 (CN-50115). (Confidential)
120. Bartley, C. E.: Application of Simplified Method for Determining the Internal-Ballistic Characteristics of Solid Propellants (U). CIT/JPL-PR-20-153, Jet Propulsion Laboratory, Nov. 1951. (Confidential)
121. Anon.: Engineering Design Handbook, Explosive Series, Solid Propellants, Part One. AMC Pamphlet AMCP-706-175, Headquarters, U. S. Army Material Command, Sept. 1964.
122. Stewart, D. H.; and Moon, E. L.: An Improved Method for the Measurement of Solid-Propellant Strand-Burning Rates in Closed Bombs. NAVWEPS Rep. 8070, NOTS TP 3076, Naval Ordnance Test Station, China Lake, Calif., May 1963 (AD 411911).
123. Hermance, C. E.; and Summerfield, M.: Comparison of Solid Propellant Burning Rates in Strands and Rocket Motors. Aeronautical Engineering Laboratory Rep. 556, Princeton Univ., May 1961 (N-100779).
124. Herrington, L. E.: Correlation of Motor and Strand Burning Rate. Preprint 64-150, AIAA Solid Propellant Rocket Conference (Palo Alto, Calif.), Jan. 1964 (A64-13004).
125. Summerfield, M.: Burning Mechanism of Ammonium Perchlorate Propellants. Part II: Theory of Burning of a Composite Solid Propellant. Paper presented at Thirteenth Annual Meeting, American Rocket Society (New York), Nov. 1958 (N-67168).
126. Jacoby, M. H.; Gulde, R. J.; and Bloom, L.: Predicting the Performance of Solid-Propellant Rocket Motors (U). CPIA Publ. 111, vol. II, ICRPG/AIAA Solid Propulsion Conference (Wash., D. C.), July 1966 (AD 373908). (Confidential)
127. Von Elbe, G.: Theory of Solid Propellant Ignition and Response to Pressure Transients. CPIA Publ. 13, Bulletin of the Interagency Solid Propulsion Meeting (Seattle, Wash.), July 1963 (AD 338667).
128. Paul, B. E.; Lovine, R. L.; and Fong, L. Y.: A Ballistic Explanation of the Ignition Pressure Peak. AIAA Preprint 64-121, AIAA Solid Propellant Rocket Conference (Palo Alto, Calif.), Jan. 1964 (A64-13017).
129. Parker, K. H.; and Summerfield, M.: Response of the Burning Rate of a Solid Propellant to a Pressure Transient. AIAA Preprint 66-683, Second Propulsion Joint Specialists Conference (Colorado Springs, Colo.), June 1966.

130. Whitesides, R. H., Jr.; and Hodge, B. K.: Theoretical Study of the Ballistics and Heat Transfer in Spinning Solid-Propellant Rocket Motors (U). NASA CR-66639, 1968. (Confidential)
131. Anon.: A Research Study To Advance the State-of-the-Art of Solid-Propellant Grain Design. Summary Rep. E92-63, RTD-TDR-63-1049, Elkton Div., Thiokol Chemical Corp., Oct. 1963 (AD 420826)
132. Coy, J. B.: Influence of Strain on Burning Rate (U). Quarterly Summary Rep. CIT/JPL-QSR-38-4 for period 1 April to 30 June 1961, California Institute of Technology, July 1961. (Confidential)
133. Saylak, D.: The Effect of Strain on the Burning Rate of Solid Propellants. CPIA Publ. 27, Bulletin of Second ICRPG Working Group on Mechanical Behavior, Hill Air Force Base, Nov. 1963 (AD 345530).
134. Mood, A. M.: Introduction to the Theory of Statistics. Second ed., McGraw-Hill, Inc., 1963.
135. Ditore, M. J.; and Haigh, W. S.: Minuteman Nozzle Contour Development Program: Phases I and II (U). AGC-TN-61-35 (TM-158 SRP), Aerojet-General Corp., Nov. 1961. (Confidential)
136. Lenoir, J. M.; and Robillard, G.: A Mathematical Method To Predict the Effects of Erosive Burning in Solid-Propellant Rockets. Sixth Symposium on Combustion (Reinhold, N. Y.), 1957, pp. 663-667.
137. Peretz, A.: Experimental Investigation of the Erosive Burning of Solid Propellant Grains With Variable Port Area. AIAA J., vol. 6, no. 5, May 1968, pp. 910-912.
138. Saderholm, C. A.: A Characterization of Erosive Burning for Composite H-Series Propellant. AIAA Solid Propellant Rocket Conference (Palo Alto, Calif.), Jan. 29-31, 1964.
139. Bartz, D. R.: A Simple Equation for Rapid Estimation of Rocket Nozzle Convection Heat Transfer Coefficients. Jet Propulsion, Jan. 1957, pp. 49-51.
140. Anon.: Third Stage Minuteman Production Support Program Quarterly Progress Rep. MCS-701-15 (U). Hercules Powder Co., Nov. 1965 (AD 367760). (Confidential)
141. Anon.: JANAF Thermochemical Data Book. (N-90810) Dow Chemical Co., Aug. 1963. (Confidential)
142. Cherry, S. S.: Phase II Final Report—Screening of Reaction Rates. TRW Rep. 08832-6002-T000, Dec. 6, 1967 (AD 828795).
143. Ditore, M. M.; Hartsell, J. O.; and Thomas, R. M.: Investigation of Heterogeneous Propellant Two-Phase Flow Criteria (U). AGC Rep. 11205-F-1, Aerojet-General Corp., Apr. 1967 (AD 380486). (Confidential)

144. Lawrence, W. J.; Matthews, D. R.; and Deverall, L. I.: The Experimental and Theoretical Comparison of the Erosive Burning Characteristics of Composite Propellants. AIAA Preprint 68-531, Third ICRPG/AIAA Solid Propulsion Meeting (Atlantic City), June 1968 (A68-32438).
145. Northam, G. B.: Effects of Steady-State Acceleration on Combustion of an Aluminized Composite Solid Propellant. NASA TN D-4914, 1968.
146. Eisenhart, C.; Hastay, W. M.; and Wallis, W. A.: Techniques of Statistical Analysis. McGraw-Hill, Inc., 1947.
147. Becker, E. B.; and Brisbane, J. J.: Application of the Finite Element Method to Stress Analysis of Solid Propellant Rocket Grain. Rep. S-76, vol. 2, Rohm and Haas Company, Jan. 1966 (AD 476515, 476735).
148. Beers, Y.: Introduction to the Theory of Error. Addison-Wesley Publishing Company, Inc., 1955, pp. 26-34.
149. Geckler, R. D.; and Sprenger, D. F.: The Correlation of Interior Ballistic Data for Solid Propellants. ARS J., vols. 1-2, Feb. 1954, pp. 22-26.

GLOSSARY

The nomenclature used in the preceding text basically is that presented in CPIA Publication 80, "Solid Propellant Nomenclature Guide" (ref. 118). Identification and brief explanations for symbols taken from this reference are included. Frequently used subscripts are presented at the end of the Glossary for combination with general symbols; for example, subscripts e and t combined with symbol A are to be interpreted as A_e , the area at the nozzle exit plane, and A_t , the area at the nozzle throat. The guide should be reviewed for complete coverage of recommended solid propulsion symbols and subscripts, as only those used in this monograph are presented herein.

<u>Symbol</u>	<u>Definition</u>	<u>Remarks</u>
A	area, in. ²	
A_b	area of propellant burning surface	
A_p	cross-sectional flow area for grain port	
A_s	local nozzle surface area	
a	coefficient of pressure in linear burning-rate equation	$r = aP^n$
BEM	ballistic evaluation motor	
C_D	mass flow factor, sec ⁻¹	$C_D = g_c/c^*$, in eq. (7a)
C_D	drag coefficient	
$C_{D_{inc}}$	drag coefficient assuming incompressible fluid	table I
C_F	nozzle thrust coefficient	$C_F = F/(P_c A_t)$
$C_{F_{ideal}}$	idealized nozzle thrust coefficient	eq. (22)
C_f	skin friction coefficient	
C_W	discharge coefficient	defined in eq. (19)
C, E	limits on control surface passing through exit of nozzle and intersecting meridional plane	fig. 3; eq. (21)
c	effective exhaust velocity, ft/sec	in instantaneous form, $c = F/\dot{m}_p$
c^*	characteristic exhaust velocity	in instantaneous form, $c^* = (P_c A_t)/\dot{m}_p$
c_p	propellant specific heat, Btu/lb _m -°F	

<u>Symbol</u>	<u>Definition</u>	<u>Remarks</u>
D	diameter, in. or ft	
D_m	mass-median particle diameter, μ	ref. 63
D_{32}	Sauter-mean particle diameter, μ	ref. 63
\bar{D}_v	volume-mean particle diameter, μ	ref. 63
dA	elemental control surface area	
F	thrust, lb_f	eqs. (1) and (2)
G	mass flux, $\text{lb}_m/\text{sec-in.}^2$	mass flowrate per unit of cross-sectional flow area
g	acceleration of gravity, ft/sec^2	32.17 ft/sec^2
g_c	gravitational conversion constant	$32.17 \text{ lb}_m\text{-ft/lb}_f\text{-sec}^2$, where $1 \text{ lb force} = 1 \text{ lb mass} \times 32.17$
H	enthalpy, Btu	
h	coefficient of heat transfer, $\text{Btu/hr-ft}^2\text{-}^\circ\text{F}$	
h_c	convective heat-transfer coefficient	
I	impulse, $\text{lb}_f\text{-sec}$	$I = \int_{t_1}^{t_2} F dt$
I_{sp}	propellant specific impulse, $\text{lb}_f\text{-sec/lb}_m$	Used only in general reference to propellant specific impulse or in reporting nonstandard corrected values of I_{sp} . All numerical values must be accompanied by specification of the following assumptions: (1) chamber pressure P_c (2) ambient pressure P_a (3) nozzle area expansion ratio ε and whether or not this is optimum (4) nozzle divergence half-angle α . Use the same time interval and propellant mass assumptions as for I_{sp} ; therefore, do not report a numerical value of I_{sp} without reporting the corresponding value of I_{sp} .

<u>Symbol</u>	<u>Definition</u>	<u>Remarks</u>
I_{sp}^o	theoretical propellant specific impulse	Calculated from propellant thermodynamic properties. All numerical values must be accompanied by specification of items (1) through (4) as for I_{sp} plus (5) assumption of frozen or equilibrium exit composition (6) physical state of exhaust condensables.
I_{spd}	measured (delivered) propellant specific impulse	Calculated from data from an actual motor firing. All numerical values must be accompanied by specification of motor conditions (1) through (4) for I_{sp} plus (5) time interval used for impulse determination (6) propellant mass assumption.
I_{spd}^o	theoretical delivered propellant specific impulse	Calculated from propellant thermodynamic properties assuming same conditions (1) through (4) reported for I_{spd} with added specification of either frozen or equilibrium exit composition and physical state of exhaust condensables. Use I_{spd}^o only when it can be compared with an available I_{spd} . If no I_{spd} is available, use I_{sp}^o instead of I_{spd}^o .
I_{sp8}	standard delivered propellant specific impulse	I_{spd} corrected to the following standard conditions: (a) chamber pressure $P_c = 1000$ psia (b) ambient pressure $P_a = 14.7$ psia (c) nozzle area expansion ratio $\epsilon = \text{optimum}$ (d) nozzle divergence half-angle $\alpha = 0^\circ$ The time interval and propellant mass assumptions are the same as for I_{spd} ; therefore, I_{sp8} should not be reported without also reporting the corresponding I_{spd} and motor description.

<u>Symbol</u>	<u>Definition</u>	<u>Remarks</u>
i	unit vector in x-direction	
J	mechanical equivalent of heat, 778.2 ft-lb _f /Btu	
K	variation factor, considering probability desired	eq. (76)
Kn	Knudsen number	$Kn = \frac{\text{length of mean free path}}{\text{characteristic dimension of system}}$
K_n	ratio of area of burning surface to area of throat	$K_n = A_b/A_t$
k	thermal conductivity, Btu/hr-ft-°F	
k_i	proportionality constants	where $i = 1, 2, \dots$
L	length, in.	
L/D	ratio of length to diameter	
M	Mach number	
\dot{M}	mass flowrate summation, lb _m /sec	defined in eq. (7a)
\bar{M}	average molecular weight, lb _m /lb _m -mole	
m	mass, lb _m	
\dot{m}	mass flowrate, lb _m /sec	
N	number of data points in sample	
Nu	Nusselt number	eqs. (60) and (61), table II
n	pressure exponent in linear burning-rate relationships	
\hat{n}	unit vector normal to control surface	
P	pressure, lb _f /in. ²	All pressures are static unless otherwise specified.
P_{bo}	chamber stagnation pressure at burn-out	
Pr	Prandtl number	$Pr = \mu g c_p/k$
Q	total heat loss, Btu	
q	heat required for pyrolysis of unit weight of liner, Btu	
\dot{q}	heat flux, Btu/hr-ft ²	
R	radius, in.	
R^*	radius of curvature at nozzle throat, in.	
Re	Reynolds number	$Re = D u \rho/\mu$

<u>Symbol</u>	<u>Definition</u>	<u>Remarks</u>
R_h	hydraulic radius, in.	$2 \times \left(\frac{\text{port cross-sectional areas}}{\text{port perimeter}} \right)$
R_0	universal gas constant, 1545.5 ft-lb _f /lb _m -mole-°R	
r	propellant linear burning rate, in./sec	
r_b	propellant burning front progression rate, in./sec	
S	entropy, Btu/lb _m -°R	
s	estimate of standard deviation	defined in eq. (75)
T	temperature, °F or °R	
T_{aw}	adiabatic wall temperature	recovery temperature on gas side of boundary layer
T_w	wall temperature	
t	time, sec	
u	velocity, ft/sec	
\vec{u}	local velocity vector, ft/sec	
V	volume, in. ³	
V_c	chamber free volume	
v	parameter variation on which limits are being established	defined in eq. (76)
W	weight, lb _f	
W_L	weight of liner lost during firing	
\bar{X}	data population mean	defined in eq. (74)
X_i	datum for the i th term or the i th test	where $i = 1, 2, \dots$
x	component along x-axis	
α	erosive burning-rate constant	$\alpha = 0.0288 k_q c_p \mu^{0.2} Pr^{-0.667}$ in eq. (50)
α	nozzle-divergence half-angle, or half-angle of inscribed cone, deg	eqs. (23) and (31); fig. 25
α	Mach angle, deg	$\sin \alpha = \frac{1}{M}$, in eq. (21)
α	Stefan-Boltzmann constant	eq. (63)
β	erosive burning-rate constant	eq. (50)

<u>Symbol</u>	<u>Definition</u>	<u>Remarks</u>
β	nozzle - entrance convergence half-angle, deg	
γ	ratio of specific heats	$\gamma = \frac{\text{heat capacity at constant pressure}}{\text{heat capacity at constant volume}}$
δ	burning-rate augmentation term	
ε	ratio of given area to the nozzle throat area	$\varepsilon = A/A_t$
$\dot{\varepsilon}$	instantaneous nozzle surface erosive rate, in./sec	
ε_τ	particle cloud emissivity	eq. (63)
η	efficiency factor	
η_F	nozzle thrust coefficient efficiency	$\eta_F = C_F/C_{F_{ideal}}$
η_θ	c* efficiency	$\eta_\theta = \frac{\text{delivered characteristic exhaust velocity}}{\sqrt{\frac{g_c}{\gamma} \left(\frac{\gamma+1}{2} \right)^{(\gamma+1)/(\gamma-1)} \left(\frac{R_0 T_c}{M} \right)}}$
η_μ	deliverable motor efficiency	$\eta_\mu = I_{spd}/I_{o_{spd}}$
θ_{ex}	nozzle-exit-plane lip angle, deg	
λ	divergence loss factor	
μ	viscosity, lb _f -sec/ft ²	
π_K	temperature sensitivity of pressure at a particular value of K_n	$\pi_K = \left[\frac{\partial \ln P}{\partial T_o} \right]_{K_n}$
$\pi_{P/r}$	temperature sensitivity of pressure at a particular value of P/r	$\pi_{P/r} = \left[\frac{\partial \ln P}{\partial T_o} \right]_{P/r}$
ρ	mass density, lb _m /in. ³	
σ_K	temperature sensitivity of burning rate at a particular value of K_n	$\sigma_K = \left[\frac{\partial \ln r}{\partial T_o} \right]_{K_n}$
σ_P	temperature sensitivity of burning rate at a particular value of P	$\sigma_P = \left[\frac{\partial \ln r}{\partial T_o} \right]_P$
τ_R	residence time, sec	
ϕ	angle between local velocity vector and motor centerline, deg	

Subscripts

<i>a</i>	ambient
<i>BL</i>	boundary layer
<i>bem</i>	ballistic evaluation motor
<i>c</i>	local stagnation conditions in combustion chamber
<i>cs</i>	surface of control volume
<i>cv</i>	control volume
<i>e</i>	nozzle-exit plane
<i>e'</i>	spherical exit control surface for point-source flow model
<i>fsm</i>	full-scale motor
<i>g</i>	combustion products
<i>i</i>	ideal
<i>i</i>	initiation of shock/turbulent-boundary-layer interaction
<i>ig</i>	igniter
<i>L</i>	liner
<i>m</i>	motor
<i>mem</i>	material evaluation motor
<i>o</i>	condition of motor and propellant just prior to ignition
<i>p</i>	propellant
<i>ref</i>	value at reference conditions
<i>s</i>	separation
<i>s</i>	nozzle submergence depth in motor
<i>t</i>	nozzle throat
<i>tv</i>	threshold value
<i>vac</i>	vacuum
<i>x</i>	component along x-axis
Δ	incremental value
1	forward end of motor element
2	aft end of motor element

NASA SPACE VEHICLE DESIGN CRITERIA

MONOGRAPHS ISSUED TO DATE

ENVIRONMENT

SP-8005	Solar Electromagnetic Radiation, June 1965
SP-8010	Models of Mars Atmosphere (1967), May 1968
SP-8011	Models of Venus Atmosphere (1968), December 1968
SP-8013	Meteoroid Environment Model—1969 (Near Earth to Lunar Surface), March 1969
SP-8017	Magnetic Fields—Earth and Extraterrestrial, March 1969
SP-8020	Mars Surface Models (1968), May 1969
SP-8021	Models of Earth's Atmosphere (120 to 1000 km), May 1969
SP-8023	Lunar Surface Models, May 1969
SP-8037	Assessment and Control of Spacecraft Magnetic Fields, September 1970
SP-8038	Meteoroid Environment Model—1970 (Interplanetary and Planetary), October 1970
SP-8049	The Earth's Ionosphere, March 1971

STRUCTURES

SP-8001	Buffeting During Atmospheric Ascent, revised November 1970
SP-8002	Flight-Loads Measurements During Launch and Exit, December 1964
SP-8003	Flutter, Buzz, and Divergence, July 1964
SP-8004	Panel Flutter, July 1964
SP-8006	Local Steady Aerodynamic Loads During Launch and Exit, May 1965
SP-8007	Buckling of Thin-Walled Circular Cylinders, revised August 1968
SP-8008	Prelaunch Ground Wind Loads, November 1965

SP-8009	Propellant Slosh Loads, August 1968
SP-8012	Natural Vibration Modal Analysis, September 1968
SP-8014	Entry Thermal Protection, August 1968
SP-8019	Buckling of Thin-Walled Truncated Cones, September 1968
SP-8022	Staging Loads, February 1969
SP-8029	Aerodynamic and Rocket-Exhaust Heating During Launch and Ascent, May 1969
SP-8030	Transient Loads From Thrust Excitation, February 1969
SP-8031	Slosh Suppression, May 1969
SP-8032	Buckling of Thin-Walled Doubly Curved Shells, August 1969
SP-8035	Wind Loads During Ascent, June 1970
SP-8040	Fracture Control of Metallic Pressure Vessels, May 1970
SP-8042	Meteoroid Damage Assessment, May 1970
SP-8043	Design-Development Testing, May 1970
SP-8044	Qualification Testing, May 1970
SP-8045	Acceptance Testing, April 1970
SP-8046	Landing Impact Attenuation For Non-Surface-Planing Landers, April 1970
SP-8050	Structural Vibration Prediction, June 1970
SP-8053	Nuclear and Space Radiation Effects on Materials, June 1970
SP-8054	Space Radiation Protection, June 1970
SP-8055	Prevention of Coupled Structure-Propulsion Instability (Pogo), October 1970
SP-8056	Flight Separation Mechanisms, October 1970
SP-8057	Structural Design Criteria Applicable to a Space Shuttle, January 1971
SP-8060	Compartment Venting, November 1970
SP-8061	Interaction With Umbilicals and Launch Stand, August 1970
SP-8062	Entry Gasdynamic Heating, January 1971

GUIDANCE AND CONTROL

SP-8015	Guidance and Navigation for Entry Vehicles, November 1968
SP-8016	Effects of Structural Flexibility on Spacecraft Control Systems, April 1969
SP-8018	Spacecraft Magnetic Torques, March 1969
SP-8024	Spacecraft Gravitational Torques, May 1969
SP-8026	Spacecraft Star Trackers, July 1970
SP-8027	Spacecraft Radiation Torques, October 1969
SP-8028	Entry Vehicle Control, November 1969
SP-8033	Spacecraft Earth Horizon Sensors, December 1969
SP-8034	Spacecraft Mass Expulsion Torques, December 1969
SP-8036	Effects of Structural Flexibility on Launch Vehicle Control Systems, February 1970
SP-8047	Spacecraft Sun Sensors, June 1970
SP-8058	Spacecraft Aerodynamic Torques, January 1971
SP-8059	Spacecraft Attitude Control During Thrusting Maneuvers, February 1971
SP-8065	Tubular Spacecraft Booms (Extendible, Reel Stored), February 1971
SP-8070	Spaceborne Digital Computer Systems, March 1971
SP-8071	Passive Gravity-Gradient Libration Dampers, February 1971
SP-8074	Spacecraft Solar Cell Arrays, May 1971

CHEMICAL PROPULSION

SP-8052	Liquid Rocket Engine Turbopump Inducers, May 1971
SP-8048	Liquid Rocket Engine Turbopump Bearings, March 1971
SP-8051	Solid Rocket Motor Igniters, March 1971
SP-8025	Solid Rocket Motor Metal Cases, April 1970
SP-8041	Captive-Fired Testing of Solid Rocket Motors, March 1971